Microfabrication and Modeling of a Tool for Thermodynamic Characterization of Micro-Samples

A Thesis presented to the Faculty of the Graduate School

University of Missouri

In Partial Fulfillment

of the Requirements for the Degree

Master of Science

by

Logan M. Compton

Dr. Gary L. Solbrekken, Thesis Supervisor

May 2012

The undersigned, appointed by the Dean of the Graduate School, have examined the thesis entitled:

Microfabrication and Modeling of a Tool for Thermodynamic Characterization of Micro-Samples

Presented by Logan M. Compton

A candidate for the degree Master of Science

And hereby certify that in their opinion it is worthy of acceptance

---

Dr. Gary L. Solbrekken

Dr. Frank Feng

Dr. Mahmoud Almasri

Acknowledgements

The process of accomplishing the feats I set out to do two years ago could not possibly have become a reality without the assistance and support I received from key co-workers and colleagues. I would like to thank my advisor Dr. Solbrekken for the vast amounts of invaluable support and advise that has led me to expand my horizons and critical thinking ability. I would like to thank Dr. Almasri, Dr. Feng, Joseph Mathai and Nuh Yuksek for their technical support in dealing with MEMS manufacturing problems and processes while allowing me to utilize their lab. I would like to thank the late Dr. John Critser and his colleague Xu Han for their advice and assistance within the biological sector of the supported research. Countless hours and support from my lab partner James Armes on developing software protocols and experimental testing has expedited research progress to unaccounted limits, and for that I am very grateful. Honorable mentions for their helpful assistance and advice go out to Mitch Tarka, John Kennedy, William Zhao, and Phillip Makarewicz.

Table of Contents

Acknowledgements ii

Table of Contents iii

List of Tables ix

List of Figures x

Nomenclature xiii

Abstract iv

Chapter 1. Introduction 1

Motivation 1

Measurement Techniques 2

IIF Measurement 3

Chapter 2. Calorimetry 6

Introduction 6

DSC vs DTA 6

.....

Heat Capacities 8

Heat Release or Absorption Measurement 9

Mass-Difference Base Line Method 9

Determining Area under Endothermic or Exothermic Curve 11

Micro-Scale 12

Micro-Calorimetry Device Design 13

Mass Measurements 15

Conclusion 16

Chapter 3. Proposed Micro-DTA 17

Micro-DTA Design 17

Volume Measurement 19

Single Micro-DTA 19

DTA Calibration Uncertainty Analysis 23
Physical Experimental Design 24
Housing Fixture 24
Thermocouple 27
Micropipette 28
Cold Trap 28
Humidity Sensor 30
Outer Enclosure Box 30
Microscope Camera 31
Control System Experimental Design 31
Numerical Model Development 32
Control Volume Theory 32
Discretization of Control Volume 33
Custom Model Case Check 35
Numeric Model 37
Source Terms 38
Boundary Conditions 39
Calibration 40
Initial Condition 42
Control System 42
Control System Results 43
Experimental Procedures 44
Thermocouple Placement 45
Micro-pipette placement 46
Chiller and Equipment Preparation 47
Liquid Sample deposition 47
Oocyte Sample 48
Oocyte preparation 48
Oocyte deposition 49
Volume Abstraction 49
Diameter Abstraction 50
Procedure Conclusion 50

Chapter 4. Micro-DTA of Micro-Sample Results 51

Repeatability of Dry run Trials 51

Micro-DTA Heat Capacity Calibration using water samples. 53

Micro-DTA Heat of Fusion Calibration using water samples. 55

Micro-DTA Results Conclusion 57

Chapter 5. Introduction of M.E.M.S. Manufacturing 58

Review 58

Micro-Bridge Fabrication Design 61

L.I.G.A. Introduction 64

General Overview 64

Substrate as the Platform 65

Surface Cleaning 65

Base Layer Deposition 68

Photoresist 70

Photoresist Coating 72

Soft bake 76

Lithography 77

Mask Design 77

Alignment 78

Exposure 80

Post Exposure Bake 81

Development 81

Electroplating 82

Electrolyte Solution 82

Current Density 83

Pulsed Plating 86

Etching 90

LIGA Conclusion 90

Chapter 6. Micro-D.T.A. Manufacturing Process 91

Equipment and Overview 91

Manufacturing Process 92
Sputtering Nickel 92
Applied Photoresist 94
NR21-20000P 94
Application of Photoresist 94
Resistance Probe Measurement Process 95
Spinning Process 98
Soft Baking Procedures 99
Mask Design 100
Overview 100
Mask Design Process 100
Exposure 103
Post Exposure Relaxation 106
Post Exposure Bake Procedures 107
Photo Resist Development 108
Post Development Resistance Testing 109
Electroplating 110
Electrolyte Solution 111
Current Density Overview and Equipment 112
Electroplating Procedures 113
Determining Duty Cycle and Frequency 115
Determining the Limiting Current Density 116
Electroplating Time 117
Striking 118
Smoothing 119
Resist Removal 119
Etching 120
Etching Procedure 121
Etching time study 122
Bridge Release Etching 123
Sample Characterization 124
Microscope camera 124
Image J 125

Optical profilometer **127**
Bowl Characterization **129**
Volume homogeneity program **129**
Process Integration **131**
Base structure 131
Cylinder 133
Crucible 134
Manufacturing Conclusion **135**
Chapter 7. DTA Manufacturing Results **136**
Introduction **136**
Successful Fabrication Results **137**
Resist application 137
Development 138
Electroplating 141
Electroplating Cylinders **142**
Electroplating Study **145**
Crucible Fabrication Results **146**
Etching Fixture 146
Mask Diameter Study 147
Etching Rate Study 148
Final Bridge with Crucible **149**
Micro-DTA Manufacturing Conclusion **151**
Works Cited **153**
Appendix: **158**
Numeric Model **158**
Control System **164**
DTA Area Calculator: **169**
DTA Heat Capacity Calculator: **171**
Height as a function of Diameter Calculator **175**
Volume as a function of Height Calculator **177**

Crucible Volume Homogeneity Program **179**

Chemical List **186**

List of Tables

Table 1 Steady State constant temperature boundary condition case check results 35
Table 2 Heat generation term case check 36
Table 3 Transient case check simulation results..... 36
Table 4. Numeric model layering thermodynamic values 37
Table 5. Source Term Properties..... 39
Table 6. Natural Convection Properties..... 40
Table 7. Micro-DTA Heat Capacity Calibration Results..... 55
Table 8. Freezing Temperatures and Heat of Fusions for water sample 57
Table 9. Pickling solution preparation procedure. 95
Table 10. Prescribed settings for desired thickness. 98
Table 11. Soft baking procedures as a function of photoresist thickness 100
Table 12. Post Exposure Bake Procedures (Futurrex)..... 108
Table 13. Electrolyte Bath Procedure 112
Table 14. Electrical current profile settings for pulsed electroplating 116
Table 15. Recommended values for desired growth height..... 118
Table 16. Procedures for Mixing Nickel Etching Solution 124
Table 17. Base Pulsed Electroplating Procedures..... 132
Table 18. 225 micron crucible pulsed electroplating procedures 134
Table 19. Resist Application Trouble Shooting Table 138
Table 20. Development Troubleshooting Table..... 141
Table 21. Electroplating Trouble Shooting Table..... 145
Table 22. Electroplating Thickness Vs. Time Study 146
Table 23. Fixture vs No Fixture Etching Experiment 147
Table 24. Mask Diameter Etching Study 148
Table 25. Etching Rate Study 149
Table 26. Geometry Characterization of Final Bridge..... 150

List of Figures

Figure 1. Typical DSC Operation 7

Figure 2. Typical DTA Operation 7

Figure 3. Phase transition curve (Pope and Judd n.d.) 11

Figure 4. Area under curve based upon the change in heat capacity of the sample after transition (Guttman and Flynn n.d.) 12

Figure 5. Trapezoidal integration performed on curve (Guttman and Flynn n.d.) 12

Figure 6. Membrane type calorimeter (Youssef, et al. 2009) 14

Figure 7. RTD Spiral Membrane Type Calorimeter (Yu, et al. n.d.) 14

Figure 8. RTD type Calorimeter Bridge Type Design. (Senesac, et al. n.d.) 15

Figure 9. Micro-DTA Setup 18

Figure 10. Baseline measurement run 21

Figure 11. Sample Measurement run 21

Figure 12. DTA test section setup 25

Figure 13. Side sectional view of DTA housing 26

Figure 14. Rear Sectional view of DTA housing 26

Figure 15. DTA Housing Front View 27

Figure 16. Cold Trap to deliver dry air to DTA housing. 29

Figure 17. Dry air system 29

Figure 18. Outer Enclosure Box 31

Figure 19. Conservation Framework 33

Figure 20. 2-D discretized control volume layout 33

Figure 21. 1-D discretized control volume setup 34

Figure 22 Numeric Model Layering Scheme 37

Figure 23 Boundary Conditions & Source Terms 40

Figure 24 1K/sec cooling profile produced from the current profile determined by the numeric control system 43

Figure 25. 1K/sec sinusoidal cooling profile produced from the current profile determined by the numeric control system 44

Figure 26. Thermocouple placement in Micro-DTA bowl shaped Crucible 46

Figure 27. Dry Run to Validate System Repeatability 52

Figure 28. Temperature Difference of Dry Run Trials 53
Figure 29. Water Sample Volume Abstraction 54
Figure 30. DTA Heat Capacity Calibration Constant Vs. Trial Number 55
Figure 31. Freezing Temperature vs Sample Number 57
Figure 32. Design of DTA/DSC bridge with location of crucible being below the bridge (left) or extruded above (right) 62
Figure 33. Difficulty in Concentric Alignment with Crucible Located Below Bridge 63
Figure 34. LIGA process flows (Kelly and Goods 2005). 65
Figure 35. Positive and Negative Resist Differences (Jones 2000) 72
Figure 36. Process of spin coating (Jones 2000) 74
Figure 37. Alignment of patterned and mask features using fiducial markings. 79
Figure 38. Primary Current Densities Between Anode and Cathode as a Function of Cathode Dimension (Kanani 2004) 84
Figure 39. Pulsed Plating Waveform (Kanani 2004) 88
Figure 40. trench profiles of four different etching procedures. (Maluf and Williams 2004) 90
Figure 41. (a) Hydrophilic surface (b) Hydropholic surface (Mechanisms behind the Lotus effect n.d.) 95
Figure 42. Resistance Probe Setup 97
Figure 43. Microscope view of resistance probe being positioned in cavity 97
Figure 44. Mask Design created by Fine Line Imaging with 20 µm resolution 101
Figure 45. Mask Printing Orientation, Read Correctly On Bottom 102
Figure 46. Gross Bridge Fabrication Process 103
Figure 47. Exposure Box with UV blocking cardboard insert 104
Figure 48. Modified microscope used as mask aligner 106
Figure 49. UV absorbing mask over laying existing topological features. 106
Figure 50. Plating Station with electronics 111
Figure 51. Electrical diagram for pulsed plating 113
Figure 52. Wafer position in electrolyte bath 114
Figure 53. Limiting Current Density 117
Figure 54. Photoresist mask design 121
Figure 55. Etching station 122

Figure 56. Abstracting known distance using Image J 126

Figure 57. Abstracting Structure Dimensions using Image J. 127

Figure 58. Wyko NT9100 optical profilometer (WYKO NT9100 Surface Profiler, setup and operation guide 2008) 128

Figure 59. 2-D plot for both X and Y crucible profile data 131

Figure 60. Bridge base construction 133

Figure 61. Cylinder fabrication process 134

Figure 62. Crucible creating process 135

Figure 63. Resist cracking after development 139

Figure 64. Undercutting of resist microcavities 140

Figure 65. Proper development 140

Figure 66. Poor deposition results during standard D.C. plating 143

Figure 67. Electrical resistance matrix of fully developed cavities 143

Figure 68. Electrodeposition voltage potential increased dramatically around 50 min indicating poor results 144

Figure 69. Improved deposition results as an outcome from pulsed D.C. electrodeposition. 144

Figure 70. Side view of final micro-DTA bridge with crucible 151

Figure 71. Top view of final micro-DTA bridge with crucible 151

Nomenclature

Variables

a	Fluid Dimensionless parameter
A	Conductive Area
A_{DTA}	Area of exothermic or endothermic curve
B_c	Calibration Constant
c	Specific Heat
C_p	Heat capacity
$C^B{}_{x=\infty}$	Bulk Electrolyte Concentration
$C_{x=0}$	Electrode Surface Concentration
$\frac{dc}{dx}$	Concentration Gradient
d	Mask Diameter
D_c	Diffusion Coefficient
D	Crucible Diameter
DT	Cooling Rate
DTA	Area under Curve for
$\frac{\partial E}{\partial t}$	Energy Rate
F	Faraday's Constant
F_{obj}	Objective Function
g	Acceleration Due to Gravity
g_f	Shape Factor
h	Enthalpy of fusion
h_{th}	Photo Resist Thickness
H	Enthalpy change per unit mass
$\frac{dH}{dT}$	Heat of Fusion Rate with respect to Temperature
$\frac{dH}{dt}$	Enthalpy Rate
I	Electrical Current
I_A	Average Current
I_P	Peak Current
J	Current Density
J_I	Limiting Current Density
k	Thermal Conductivity
K_1	Device Heat Transfer Coefficient
K_2	Apparatus parameter
L	Characteristic Length
m	Mass
m_s	Mass of sample
M_w	Atomic Weight
n	Refractive index
n_e	Number of electrons
N_i	Total number of Ice Crystals
$\overline{Nu}_L$	Average Nusselt Number
NA	Numerical Aperture
n_m	Moles of Electrons
P	Normalized distribution function
ΔP	Heat flow of the sample
q_{PC}	Peltier Cooling Term
q_{PH}	Peltier Heating Term
q_J	Joule Heating Term
r_i	Mean ice crystal radius
Ra_L	Rayleigh Number
R	Ideal Gas Constant
r_s	Scanning rate
S	Source Term
S_c	Temperature Independent Source Term
S_p	Temperature Dependent Source Term
t	Time
t_c	Charging Time
t_D	Discharging Time
t_{UV}	UV Exposure Time

T	Temperature
T_m	Melting Point Difference
T_o	Melting Temperature of Free Liquid
$\frac{\partial T}{\partial t}$	Temperature Rate
$\vec{u}$	Velocity component
U	Uncertainty
V	Volume
w	Rotational Speed
W	Minimum Line Width
y	Fluid Dimensionless parameter

Greek

α	Thermal Diffusivity
β_t	Thermal Expansion Coefficient
β	Half Angle of image
γ	Surface tension parameter
Γ	Diffusion Coefficient
δ	Boundary Layer Thickness
δx	Node Spacing
Δ	Change in
Δx	Control Volume Size
ε	Overall heat transfer coefficient
λ	Wave Length
η	Concentration Polarization
φ	Arbitrary Intensive Property
σ	Seebeck Coefficient
ρ	Density
ρ_e	Electrical Resistivity
ν	Kinematic Viscosity
ν_o	Photo Resist Viscosity

Subscripts

1,2,3..	Sample 1,2,3..
c	charging
cs	numeric model
b	Base
B	Bottom Term
d	desired
e	East Boundary
E	East Node
j	Iteration
LS	Large Sample
me	Ice Crystal Melting
P	Present Node
o	Initial
n	Total number of samples
N	North Node
SS	Small Sample
S	South Node
std	Standard Deviation
T	Top Term
test	Student t-test
W	West Node
w	West Boundary

Superscripts

n	Total number of samples
o	Previous time step

Abbreviations

AR	Aspect Ratio
CAD	Computer Aided Drafting
CPA	Cryopreservation Agent
CVD	Chemical Vapor Deposition

DI	Deionized
DSC	Differential Scanning Calorimetry
DMM	Digital Multi-Meter
DTA	Differential Thermal Analysis
EP	Extensive Property
FZK	Forschungzentrum Karlsruhe
HF	Hydrogen Fluoride
IIF	Intracellular Ice Formation
LIGA	Lithographie, Galvanoformung, Abformung
LHS	Left Hand Side
NEMS	Nano Electromechanical Systems
NIH	National Institute of Health
PCB	Printed Circuit Board
PEB	Post Exposure Bake
PED	Pulsed Electrodeposition
PEG	Polyethylene Glycol
RCA	Radio Cooperation of America
RTD	Resistance Thermal Device
RHS	Right Hand Side
SEM	Scanning Electron Microscopy
TMM	Tetramethylamonium
UV	Ultraviolet Light
VSI	Vertical Scanning Interferometry

Abstract

Successful cryopreservation protocols have been developed for a limited number of cell types through an extensive amount of experimentation. To optimize current protocols and to develop more effective protocols for a larger range of cells and tissues it is imperative that accurate transport models be developed for the cooling process. Such models are dependent on the thermodynamic properties of intracellular and extracellular solutions, including heat capacity, latent heat, and the physical phase change temperatures. Scanning techniques, such as differential-scanning calorimetry (DSC) and differential thermal analysis (DTA), are effective tools for measuring those thermodynamic properties.

Conventional thermal scanning tools require sample sizes that are multi-celled in nature. An issue with tools that require multiple cells is that the measurements effectively average the behavior of the cell sample, masking individual cell behavior. Further, extracellular solution further dismisses the desired measurement signal. It is hypothesized that evaluating thermodynamic properties of individual cells will allow more fundamental understanding of cell-level transport, and lead to more effective cryopreservation protocols.

To detect a phase change within a prototypical mouse oocyte cell (~100 µm diameter) sample holders for the scanning tools must be on the same order of size as the cell to reduce the relative thermal mass of the sample holder and to ultimately improve the measurement sensitivity. A proof-of-concept DTA sample holder with a 'bowl' to cradle the cell has been designed and fabricated using micro-electrical mechanical systems (MEMS) manufacturing techniques. Control software has been developed which

is capable of providing any desired heating or cooling profile within a humidity controlled environment. Repeatable scans using water samples have been demonstrated.

Chapter 1. Introduction

Motivation

Cryopreservation, or preserving biological materials at cryogenic temperature for an extended period of time, is a useful means to preserve biological material for indefinite periods of time. Cryopreservation is a method to preserve cells and tissues for a potentially indefinite amount of time by cooling to cryogenic temperatures where biological activity essentially ceases, such as the biochemical reactions that lead to the cell's degradation and eventually death. Unfortunately, a standard set of freezing procedures for a broad base of cell types does not exist. Cellular strengths and mechanics differ between cell type and species that prevent such cryopreservation protocols from existing (Woods, et al. 2004). The capability to preserve blood cells, reproductive cells, organs, tissues, or even bone marrow efficiently and effectively has been a goal for many researchers and new cryopreservation procedures are constantly under development for other cell types.

Biological materials undergo significant stress during the freezing process due to the liquid-to-solid phase change of intracellular water. There exists an optimal cooling rate at which the species undergoes that is related to the specie's maximum survival rate. A myriad of proteins and other substances exists within the intracellular solution that causes a freezing point depression relative to the extracellular solution (Zhao, et al. 2007) (Han and Crister 2009). During cooling the extracellular solution's chemical potential becomes lower than the intracellular solution creating an osmatic gradient, which causes the intracellular solution to flow out of the cell. If the cooling rate is too fast a critical amount of intracellular solution can be effectively trapped inside of the cell during freezing. If

enough intracellular solution exists inside of the cell during freezing the intracellular ice formation (IIF) of the trapped solution can injure the cell severely. However; if the cooling rate is too slow, too much intracellular solution can escape causing injury due to osmotic dehydration. (Gao and Crister n.d.) (Muldrew and McGann, Mechanisms of Intracellular Ice Formation 1990) (Muldrew and McGann, The Osmostic Rupture Hypothesis of Intracellular Freezing Injury 1994) (Woods, et al. 2004)

During thawing phases of a biological sample there also exists an equal amount of threat of being critically injured as during freezing even though the correct cooling rate was implemented. The warming rate is heavily dependent upon the cooling rate that was implemented. There could exist thermodynamically unstable ice crystals left from IIF that recrystallize upon thawing and destroy the cell if it was not already injured during freezing. The thawing rate is highly variable, especially if the cells survived from cellular dehydration during cooling, and is also dependent upon the species that is undergoing cryopreservation (Woods, et al. 2004).

Measurement Techniques

Intracellular ice formation coupled with water transport across the membrane during cooling is the root of unsuccessful cryopreservation procedures. The lack of a general procedure for cryopreservation exists because the liquid-to-ice phase change during cooling and ice-to-liquid phase change during thawing of the intracellular solution is not thoroughly understood. Two main methods for studying the phase transitions of biological samples exist such as cryomicroscopy and calorimetry techniques such as differential scanning calorimetry (DSC) and differential thermal analysis (DTA). Cryomicroscopy is an optical technique of observing the cell's volume during a cooling

profile providing cellular energy and mechanical information as well as freezing andthawing temperatures (Diller and Yuan 2005) (McGrath 1985). However, the cell's field of view becomes obscured when the extracellular solution freezes rendering optical methods unreliable. Also, analysis of the data obtained from optical methods requires extrapolation of 2-D to 3-D data to extract volumetric data. The assumptions required for such extrapolation data analysis can lead to misinterpretations of the cell's true behavior.

Calorimetric techniques observe specific heats, phase change temperatures, and latent heat releases or absorptions during phase change processes. This type of technique has the potential to detect multiple phase change events within a solution and is not dependent upon the order of the phase change events. If the calorimetric device is given the proper amount of sensitivity it will be able to detect both the extracellular and intracellular phase change events. Currently, the state of cryopreservation modeling assumes that the phase change for both the intracellular and extracellular solutions occur at the same temperature, which is improbable as stated earlier. It would be beneficial to determine the phase change transformations on the cell level then a fundamental understanding of cell-based behavior to develop new cryopreservation protocols can occur.

IIF Measurement

Determining the size, morphology, and amount of intracellular ice crystals is an important metric for determining protocols for successful cryopreservation. The ice formation information can help understand the tolerable amount of IIF that can occur within the cell and still be successful cryopreserved. A simplified model was created using Gibbs-Thomson relation and observing the melting-point depression to determine

the mean intracellular ice crystal size during different freezing protocols. Implementing a form of Gibbs-Thomson as shown in Eq. 1 will help determine the tolerable amount of ice formation within the cell without critically damaging the cell for cryopreservation. Using Eq. 1 below the mean intracellular ice crystal size r_i can be determined where ΔT_m is the melting point difference between the intracellular and extracellular ice crystals and T_{me} is the melting point of plane ice in the solutions. The 0.2 in Eq. 1 is derived from assuming the interface energy, fusion of ice, and density of the solution was to be constant. Present studies have only used cryomicroscopy for the determination of the melting temperatures of the intracellular and extracellular ice crystals in oocyte cells to determine the mean ice crystal radius. Using calorimetric techniques would prove to be very effective on accurately pin pointing the melting-point depression and also quantitatively determining the fusion of ice to improve the accuracy of the model (Han and Crister 2009).

$$r_i = 0.2\frac{T_{me}}{\Delta T_m} \tag{1}$$

Calorimetry also offers a method to investigate the statistical distribution of intracellular ice crystal size based on the endothermic data measurements captured by the analysis. The distribution curve can be achieved by using similar methods used to determine pore sizes of capillaries by combining the Gibbs-Thomson relation with differential calorimetry analysis. The endothermic data given by the absorption of energy during thawing that is captured by calorimetric techniques will produce a heat of fusion rate with respect to temperature $\frac{dH}{dT}$. The total number of crystals N_i, the radius of crystal size, r_i, the enthalpy of fusion, Δh, surface tension parameter, γ, and the melting

temperature of the free liquid T_o are used to solve for the normalized distribution function P using Eq. 2 below. (Cohen-Addad, et al. 2003). Using the Gibbs-Thomson derived equation an accurate model of the tolerable range of ice formation for successful cryopreservation procedures can be implemented.

$$\frac{dH}{dT} = \frac{2\pi}{3} N_i {r_i}^5 P \Delta h^2 / \gamma T_o \tag{2}$$

Unfortunately, current commercially available calorimetry devices are macroscopic relative to cell size requiring large sample sizes of cells; for 100 µm diameter cells, approximately a minimum of 100 cells would be required for the device for calorimetric analysis. Inaccuracies on determining individual cellular behavior from such large sample sizes are produced from using averaging schemes with the assumption that the cellular size, type, and state are all homogeneous throughout the solution. Also, as the individual cells undergo phase changes the latent heat released into the extracellular solution could affect the phase change of the neighboring cells.

The macroscopic nature of the current DSC and DTA devices have a large thermal mass compared to that of the cellular thermal mass which will result in a sensitivity loss due to a portion of the energy from phase changes will be used to raise the temperature of the device. This loss of sensitivity can effectively mask the intracellular phase change event within the extracellular phase change event. If the device was microscopic in nature, single cell observations are possible. With this capability the phase transitions within the cell can be readily observed and studied providing information to potentially develop an overall robust cooling procedure for different cellular types. This thesis will investigate the fabrication of a custom-built micro-differential calorimeter

device to thermodynamically characterize water samples for a proof-of-concept design to investigate oocyte cells.

Chapter 2. Calorimetry

Introduction

Often it is desirable to characterize the thermodynamic properties of an unknown substance through experimental methods. Calorimetry is the science of measuring heat of chemical reactions or physical changes that occur on a substance. Two major calorimetric techniques that will be discussed extensively are differential scanning calorimetry (DSC) and differential thermal analysis (DTA). Thermodynamic properties such as heat capacities before and after phase changes, energy changes, and phase change temperatures are obtained through DSC and DTA techniques.

DSC vs DTA

The underlying instrument setup of both the DSC and DTA techniques are very similar to one another based upon the differentiation portion of the systems. Both DSC and DTA methods requires two pans one to hold the known reference material and the other to contain the unknown sample. Both pans are not to be thermally connected to one another. Each pan also requires a method to independently measure the temperature. The difference between the DSC and DTA techniques is that the DSC technique measures the difference in energy of the two pans while the DTA measures the difference in temperature of the two pans. The DSC quantifies the amount of energy ΔP required to keep the temperature difference between the sample and reference pan at zero under a prescribed heating or cooling profile $\dot{Q}$ as illustrated in Fig 1. However, the DTA measures the difference in temperature ΔT between the sample and reference pan given

the same heating or cooling profile $\dot{Q}$ as shown in Fig 2. Both techniques are able to determine the heat capacities, the temperature at which phase change occurs in the samples and the change of energy of the sample due to either exothermic or endothermic heat exchange during the phase change of the sample.

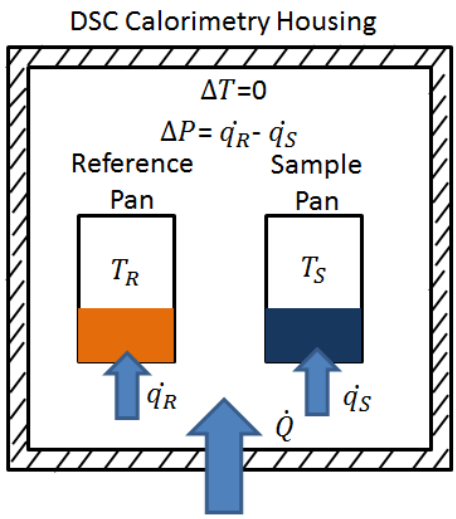

Figure 1. Typical DSC Operation

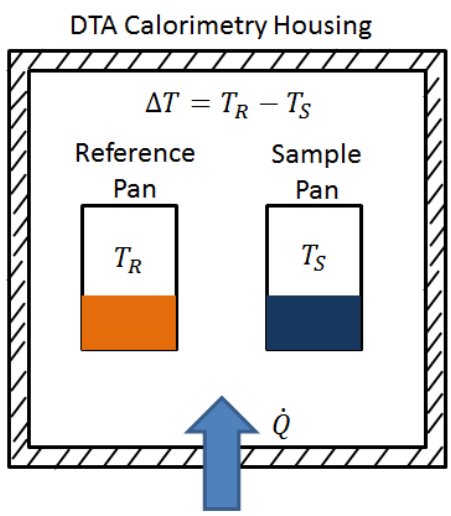

Figure 2. Typical DTA Operation

Heat Capacities

Thermodynamic quantities such as heat capacities can be calculated by evaluating either the energy differential as a function of time or the temperature differential as a function of time. Another useful metric obtained from both the DSC and DTA techniques is the temperature at which the phase change occurs. It has been found that this transition temperature depends upon the heating or cooling rates applied to the sample as described in Pope (Pope and Judd n.d.).

Once the data has been collected from the sample a few methods have been employed to determine the heat capacities of the sample with relative ease from both the DSC and DTA techniques. From the data obtained from the DSC technique the heat capacities can be calculated using Eq. 3. Where r_s is the scanning (cooling or heating) rate and ΔP is the heat flow of the sample (Simon and Cibulkova n.d.). Essentially, the heat capacity for the DTA technique can be calculated the same as for the DSC technique as shown in Eq. 4. Obviously when experimentally determining the heat capacities the calorimeters are calibrated against a substance with known heat capacities. Keep in mind that heat capacities of the unknown samples typically vary with temperature, so it is important to calibrate with a known heat capacity for the entire temperature range such as sapphire (Simon and Cibulkova n.d.).

$$C_p = \frac{\Delta P}{m r_s} \tag{3}$$

$$C_p = \frac{\Delta T}{m r_s} \tag{4}$$

Heat Release or Absorption Measurement

Quantifying the energy released or absorbed due to the phase change from the data produced from the DSC and DTA differ and will be discussed. The DSC method produces data that has change in energy in the ordinate and time or temperature as a function of time in the abscissa. To effectively determine the change in energy during a phase change of DSC is to integrate the area under the curve produced by the DSC. However, determining the change in energy using the DTA method requires previously determined knowledge of the thermal conductivity of the substance because the ordinate produced is in units of temperature and not energy. The relationship between the integrated temperature over time and change in energy during the phase change is expressed in Eq. 5 where A_{DTA} is the area of the temperature spike, m is the mass, H is the enthalpy change per unit mass, k is the thermal conductivity and g is the shape factor (Pope and Judd n.d.). To obtain the true experimental enthalpy change is by factoring in a calibration constant. This additional thermodynamic knowledge is inconvenient if the substance is completely unknown. It is more acceptable to utilize the DSC method because it does not require previous information to obtain the energy calculated.

$$H = \frac{A_{DTA}\, g_f k}{m} \tag{5}$$

Mass-Difference Base Line Method

A major difficulty in DTA measurement is that the conversion factors are rarely constant and difficult to determine as mentioned earlier. The DTA signal is not only influenced by enthalpy changes within the sample but also the heat transfer from the environment to the sample and reference materials. If the temperature range varies substantially, large errors due to asymmetric heat transfer may occur and many of the assumptions required to determine Eq. 5 becomes invalid. Equation 6. represents a

slightly simplified equation of the differential temperature between the sample measurement and baseline measurement. The first term of Eq. 6 on the right hand side is the change in enthalpy for the sample and the second term represents the difference in heat transfer coefficients between the sample and reference pan. The underlying assumption of Eq. 6 is that the difference in heat transfer coefficients between the sample and base are ignored which only is valid if the temperature range is narrow. An effective method to accurately eliminate the difference in heat transfer coefficients between the sample and base is to use the mass-difference base line method as described by Yang (Yang and Roy 1999).

$$\Delta T_1 - \Delta T_2 = \frac{m_{s,1} dH}{\varepsilon_{s,1} A\, dt} + \left(\frac{\varepsilon_{s,1} - \varepsilon_{t,1}}{\epsilon_{s,1}} - \frac{\varepsilon_{s,2} - \epsilon_{t,2}}{\epsilon_{s,2}}\right)(T_\infty - T_t) \tag{6}$$

$$\frac{dH}{dt} = K_1 K_2 \frac{(DTA_1 - DTA_2)}{(m_{s,1} - m_{s,2})} \tag{7}$$

To compensate for such heat transfer errors is by using a baseline measurement with similar heat transfer coefficients as the sample measurement to improve the linearity between the true DTA signal and the enthalpy change. The true base-line that will be used is a smaller mass sample of the substance being analyzed. Using the same substance for the baseline and sample measurement effectively eliminates the difference in heat transfer coefficients since both trials should be the same. With this assumption the second term on the RHS of Eq. 6 will be effectively diminished. A more useful relation between the change in enthalpy and change in temperature is represented in Eq. 7. Where K_1 is determined from the heat transfer from the cooling or heating device, K_2 is an apparatus related parameter as a function of temperature, $(DTA_1 - DTA_2)$ is the difference between the two curves and $(m_{s,1} - m_{s,2})$ is the differences between the two sample masses. The mass-difference base line method is a much more reliable way of measuring the change

in enthalpy than what is described as described by Pope by insuring the heat transfer coefficients are eliminated (Pope and Judd n.d.) (Yang and Roy 1999).

Determining Area under Endothermic or Exothermic Curve

In order to more accurately determine the change in energy during an exothermic or endothermic phase change is to properly determine the area underneath the curve. There exists an uncertainty as to how to draw the base line under the curve due to the fact that the heat capacity of the sample changes after the phase transition as shown in Fig. 3 where the height of point A is lower than point C. If the heat capacity changes considerably then it is critical as to how to draw the line. Pope describes that using the area points ABCA is sufficient; however it is believed that the area enclosed within ABCDEA is more accurate (Pope and Judd n.d.). Gutmann uses a different approach to obtain a more accurate calculation of the area underneath the curve. A base line is extrapolated from the steady state position after the phase transition to the beginning of the curve and the area is integrated as shown in Fig 4. Then a trapezoidal integration is performed on the curve where the phase change occurs shown in Fig. 6 (Guttman and Flynn n.d.).

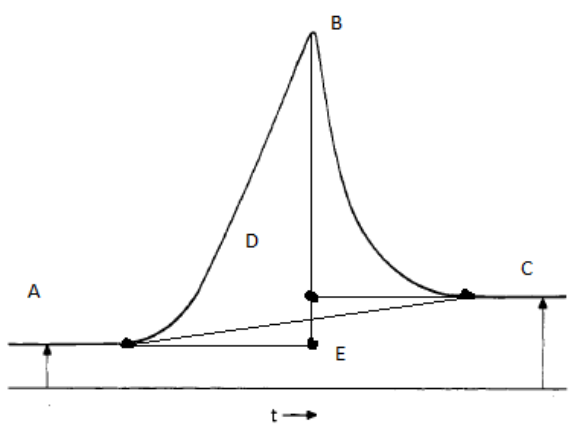

Figure 3. Phase transition curve (Pope and Judd n.d.)

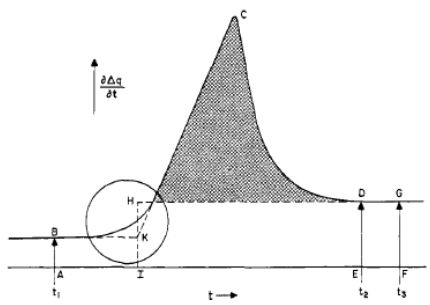

Figure 4. Area under curve based upon the change in heat capacity of the sample after transition (Guttman and Flynn n.d.)

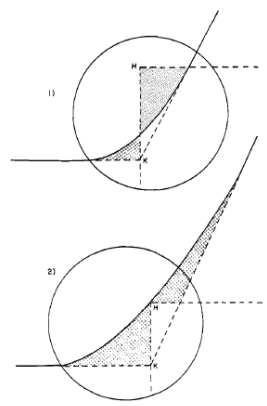

Figure 5. Trapezoidal integration performed on curve (Guttman and Flynn n.d.)

Micro-Scale

The results from DSC and DTA techniques depend greatly upon sample size and on the instrument sensitivity. The major focus of this thesis will be only on samples on the order of the micro-scale. The sensitivity is in very close relation to the design of the apparatus and in order for the instrument to be able to detect viable signals produced from the sample and reference cells, the device must be sized down to the same size order of magnitude as the sample being analyzed. Essentially, by decreasing the size of the device along with the temperature detecting devices an increase in sensitivity will occur. In recent years this has been accomplished using MicroElectricalMechanical Systems

(MEMS) manufacturing techniques. Youssef describes a serpentine-shaped device that measures 500 by 500 microns and a few nano-meters thick to measure samples on the order of nano liters (Youssef, et al. 2009). Another device can detect signals from samples on the order of micro grams (Mazieres n.d.). Decreasing the size of the devices the temperature rates can be as high as 200 K/ms, producing signals as fast as 50 ms, and having a sensitivity of 30 pico-Joules per Kelvin (Senesac, et al. n.d.) (Yu, et al. n.d.). Unfortunately, the aforementioned devices are all heater based and do not possess cooling capabilities.

Micro-Calorimetry Device Design

The design of the micro DTA and DSC is commonly a membrane or bridge design. The membrane type DSC or DTA devices are typically made of a SiN membrane with a resistive metal on top to serve as the heater element and or a resistive temperature device (RTD) as shown below in Fig. 6 (Youssef, et al. 2009) (Yu, et al. n.d.). However Olsen's device was designed as a spiral RTD along with the heater element 50 nm away, this design improved heating and temperature measuring uniformity as shown in Fig. 7 (Zhang, et al. 2003). The bridge type is designed as a thin bridge measuring around 200 microns by 500 microns with 50 nm thickness as shown in Fig 8. Like the membrane the bridge housed two separate tracks one for the heater element and the other RTD, the device was supported on relatively large silicon structures, which serves as a way to isolate the sample (Senesac, et al. n.d.) (Yu, et al. n.d.). The common design characteristic between both the bridge and membrane type is temperature uniformity through the device and sample and sample isolation.

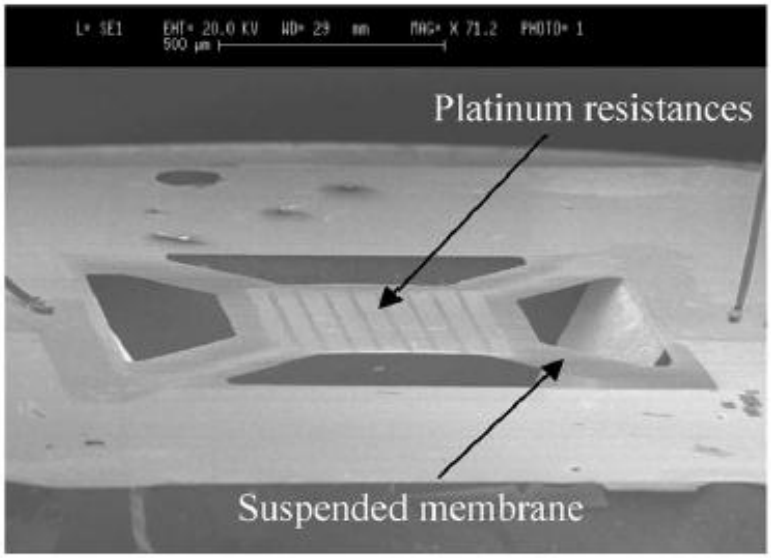

Figure 6. Membrane type calorimeter (Youssef, et al. 2009)

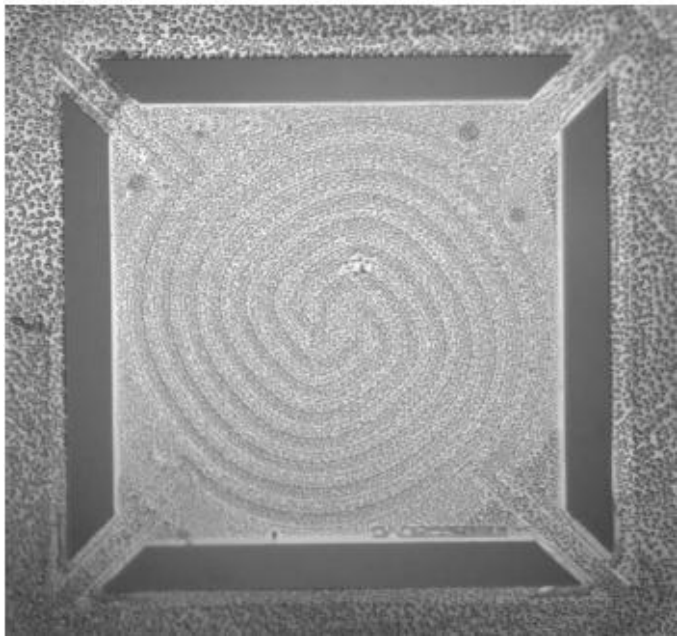

Figure 7. RTD Spiral Membrane Type Calorimeter (Yu, et al. n.d.)

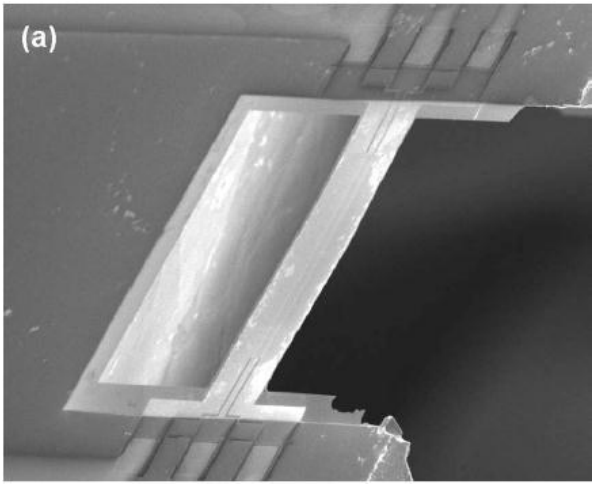

Figure 8. RTD type Calorimeter Bridge Type Design. (Senesac, et al. n.d.)

To detect signals produced from the samples during phase changes accurately it is important to ensure that the temperature sensor is in good thermal contact with sample and that there are no thermal gradients within the device or sample. As an example of error in the system caused by poor temperature measurement placement and ignored thermal gradients within the device, Bottner describes a device with micro cavities for the sample and reference that has a thermopile located away from the cavities. The results from experimentation were less than half from the expected value (Bottner, et al. 2003). Olsen and Youssef placed heavy emphasis on insuring that the thermal gradients within the sample and device were negligible by employing finite element and analytical model studies (Youssef, et al. 2009), (Yu, et al. n.d.). Without these considerations when taking measurements high levels of error can occur relative to the expected values.

Mass Measurements

One of the more important metrics involved in both DSC and DTA analysis, especially in the micro-scale level is mass, because it is involved in determining all of the thermodynamic characteristics. When scaling sample volumes down to the nano-scale the

area-to-volume ratio becomes large, meaning that boundary effects have a larger influence on the sample due to the large surface area with respect to its volume. With increased boundary effect sensitivity the atmosphere that surrounds the sample during calorimetric testing is important in quantifying. The ambient atmosphere around the sample can either be static, flowing, and may be either inert or reactive. Typically, the ambient atmosphere should be compatible with the process under investigation as described by Pope (Pope and Judd n.d.). As stated by Klancnik, when decomposition of different samples is studied such as clays or other organic materials, an oxidizing atmosphere is required. The type of sample and corresponding atmospheric composition should be carefully analyzed before any data collection to ensure that it will not alter the results.

Depositing micro-scale samples on the measuring device is usually delivered within an inert gas. The samples are allowed to condense upon the calorimetric device as described by Yu, Olsen, and Youssef. Many times during heating, the mass evaporates or desorbs into the measuring device and causes mass to be a function of time and temperature, Youssef and Olsen described using measurements of the resonance frequency of their membrane structures to determine the mass of the sample that is placed upon it (Youssef, et al. 2009) (Yu, et al. n.d.).

Conclusion

When studying samples at the micro-scale level it has been shown that the size of the measuring system is the most critical design factor followed by accurate mass data and then insuring minimal thermal gradients within for both DTA and DSC techniques. If the system is much larger than the sample being analyzed, the heat absorbed or

released by the sample during phase change will be affected by the thermal mass of the system causing thermal lagging and misleading results. That is why M.E.M.S. fabrication techniques have played a crucial role in micro-DSC and DTA analysis. Sample mass is an important metric in calorimetry since it is involved in determining the heat capacities and energy change during phase changes of the sample. Using the resonate frequency of the DTA/DSC system has proven to be a common method of determining the mass of micro-scale samples. Unfortunately, the micro-scale calorimetry devices mentioned above are all heater based and do not have the capability for cooling scans necessary for cryopreservation protocols.

Chapter 3. Proposed Micro-DTA

Micro-DTA Design

Currently, there does not exist of a micro-scanning calorimetric device that has demonstrated a cooling scan configuration to subzero temperatures and that has been effective at accurately collecting calorimetric data on biological samples. Also, conventional calorimetric pan designs are usually capped to minimize mass loss from evaporation; this blocks access for optical observations of the sample. The ideal setup would allow simultaneous observations both optically and through a temperature sensor of the biological sample. The present design of the micro-scanning calorimeter demonstrated within the scope of this paper will be a bridge with built in open-faced crucible type single-differential thermal analysis (DTA) device. A type E 25 micron diameter thermocouple is used as the temperature sensor and a commercially available thermoelectric module coupled with an industrial chilled cold block is the cooling temperature control device as shown below in Fig 9. The bridge is constructed of pure

copper and is approximately 1000 X 300 X 30µm in size with a 270 µm X 65 µm copper bowl shaped crucible attached on top. The crucible encapsulates the biological sample and the associated fluids to more effectively deliver a uniform cooling regime to the sample. An open face crucible was chosen so that the biological sample can be readily observed via microscope camera during cooling procedures and phase changes. However, the open-faced design does allow for evaporation of extracellular solutions, which causes changes in volume. Evaporation is especially apparent with small volumes due to the large surface to volume ratio of the sample. Although, a protocol has been developed to determine volume changes in real time using image abstraction. The differential thermal analysis was chosen as it allows simultaneous measurements of changes in sample mass while DSC demands constant sample mass. Manufacturing of the device is explained in detail in later sections of this thesis.

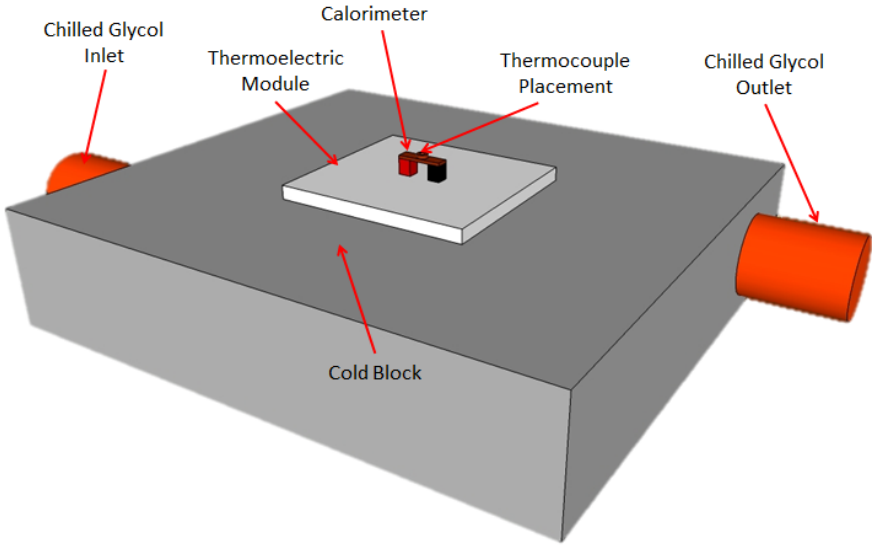

Figure 9. Micro-DTA Setup

Volume Measurement

Sample volume estimates can be taken through extrapolating 2-D diameter measurements from aerial images produced from a microscope implemented camera while also having knowledge of the contour of the bowl shaped crucible. Using measurements from an optical profilometer the bowl shaped crucible's height is a function of the diameter while the volume is a function of the height. If the extracellular solution perfectly fills and conforms to the crucible then the volume of the sample is a function of the diameter. When studying liquids such as cryoprotectant agents (CPA), a small amount of evaporation will occur causing the volume to change as a function of time. An active volume measurement scheme is ideal for liquid studies due to the fact that it will provide real time volume estimations from live video capture. The volume estimates will also allow a mass difference base-line method to be employed to maintain a repeatable measurement scheme as stated earlier. During the base line run a small amount of sample liquid V_{ss} is deposited within the crucible to ensure that the same thermal resistance is between the thermocouple and crucible wall as in the sample run. The temperature measurement repeatability would otherwise be compromised due to the differences in dry and wet thermal contact resistances between the thermocouple and crucible during the baseline and sample runs if the small sample was not deposited.

Single Micro-DTA

Instead of performing a true differential thermal analysis a single differential thermal analysis was chosen as a first order approach to micro-scale calorimetry. The single thermal analysis allows for ease in experimental setup along with a more simple data collection and temperature control system setup. The procedures for single differential thermal analysis contain two separate measurement scans, the first being the

base-line scan as shown in Fig 10 then followed by a separate sample scan as illustrated in Fig 11. An energy balance of the system was performed to determine the heat capacity of the bridge as a calibration constant to later determine thermodynamic properties of unknown substances. The energy rate $\frac{\partial E}{\partial t}$ of the system is shown in Eq.8 and is equal to the temperature gradient of the system $\nabla(\mathrm{k}\nabla\mathrm{T})$ plus the source term S. Energy E for this system is the product of the temperature T and heat capacity or the product of the specific heat c, volume V, and density ρ as shown in Eq. 9. Assuming that the volume, density, and specific heat of the system does not vary significantly within a 50 K temperature range the change of energy is equal to the change in temperature multiplied by the heat capacity terms as shown in Eq. 10. The spatial temperature gradient within the bridge is assumed to be minimal and was ignored. The energy balance of the bridge with a smaller sample ss (typically DI water) is shown in Eq. 11 where the cooling energy q replaced the source term and $\frac{\partial T}{\partial t_1}$ is the cooling profile for the base-line run.

$$\frac{\partial E}{\partial t} = \nabla(\mathrm{k}\nabla\mathrm{T}) + \mathrm{S} \tag{8}$$

$$E = TV\rho c \tag{9}$$

$$\partial E = \partial(TV\rho c) \rightarrow \partial(T)V\rho c \tag{10}$$

$$V_b\rho_b c_b \frac{\partial T}{\partial t_1} + V_{ss}\rho_{ss}c_{ss}\frac{\partial T}{\partial t_1} = \mathrm{q} \tag{11}$$

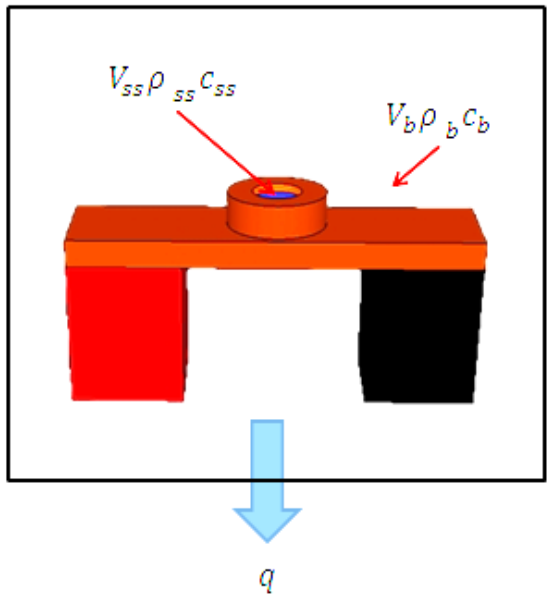

Figure 10. Baseline measurement run

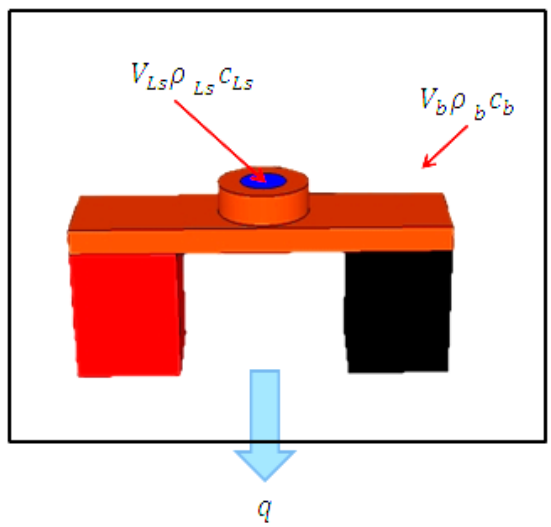

Figure 11. Sample Measurement run

By conducting a scan on a second larger sample *LS* into the crucible a second energy balance of the system is described in Eq. 12 where $\frac{\partial T}{\partial t}_2$ is the cooling profile for the

larger sample run. If the cooling term is equal in both the sample and base line runs then Eq. 11 and Eq. 12 can be set equal to one another as shown in Eq. 13. If using a known sample then the thermodynamic properties of the bridge can then be determined and calibrated by using Eq. 14. The difference between the base and sample cooling profiles $\left(\frac{\partial T}{\partial t_1} - \frac{\partial T}{\partial t_2}\right)$ will be non-zero due to the differences in thermal mass between the runs. Once calibrated Eq. 15 can be used to determine the properties of an unknown substance by assuming the thermal conductivities of the known smaller sample are similar to the larger unknown substance. The underlying assumption for the single differential thermal analysis is that the heat flow for both base-line run and sample run is identical or the differential portion would be unreliable. This is accomplished through a carefully designed experimental test section and control system, which will be discussed in detail in the following sections.

$$V_b \rho_b c_b \frac{\partial T}{\partial t_2} + V_{Ls} \rho_{Ls} c_{Ls} \frac{\partial T}{\partial t_2} = \mathrm{q} \tag{12}$$

$$V_b \rho_b c_b \frac{\partial T}{\partial t_2} + V_{Ls} \rho_{Ls} c_{Ls} \frac{\partial T}{\partial t_2} = V_b \rho_b c_b \frac{\partial T}{\partial t_1} + V_{ss} \rho_{ss} c_{ss} \frac{\partial T}{\partial t_1} \tag{13}$$

$$V_b \rho_b c_b = \frac{V_{Ls} \rho_{Ls} c_{Ls} \frac{\partial T}{\partial t_2} - V_{ss} \rho_{ss} c_{ss} \frac{\partial T}{\partial t_1}}{\frac{\partial T}{\partial t_1} - \frac{\partial T}{\partial t_2}} \tag{14}$$

$$\rho_s c_s = \frac{V_b \rho_b c_b \left(\frac{\partial T}{\partial t_1} - \frac{\partial T}{\partial t_2}\right)}{\frac{\partial T}{\partial t_2} V_{Ls} - \frac{\partial T}{\partial t_1} V_{ss}} \tag{15}$$

DTA Calibration Uncertainty Analysis

To understand the variability of the calibration data obtained an uncertainty analysis must be performed by determining the sensitivity or partial derivative of Eq. 14 with respect to each of its variables. Each sensitivity term is then multiplied by its associated student t-test uncertainty denoted by the U term then normalized to determine the total uncertainty as shown in Eq. 16. The sensitivity equations for each independent variable are shown below in Eqs (17-20). The calibration constant $V_b \rho_b c_b$ and cooling terms $\frac{\partial T}{\partial t_1}$ and $\frac{\partial T}{\partial t_2}$ was shorted to B_c, DT_1, and DT_2 for sake of simplicity. The variability of the sample's density and specific heat were assumed to be negligible within the 50 K temperature range and thus ignored for the analysis.

$$U_{B_c} = \sqrt{\left(\frac{\partial B_c}{\partial DT_2} U_{DT_2}\right)^2 + \left(\frac{\partial B_c}{\partial DT_1} U_{DT_1}\right)^2 + \left(\frac{\partial B_c}{\partial V_{ss}} U_{V_{ss}}\right)^2 + \left(\frac{\partial B_c}{\partial V_{Ls}} U_{V_{Ls}}\right)^2} \tag{16}$$

$$\frac{\partial B_c}{\partial DT_2} = \frac{\frac{\partial T}{\partial t_1} \rho_s c_s (V_{Ls} - V_{ss})}{\left(\frac{\partial T}{\partial t_2} - \frac{\partial T}{\partial t_1}\right)^2} \tag{17}$$

$$\frac{\partial B_c}{\partial DT_1} = \frac{\frac{\partial T}{\partial t_2} \rho_s c_s (V_{ss} - V_{Ls})}{\left(\frac{\partial T}{\partial t_1} - \frac{\partial T}{\partial t_2}\right)^2} \tag{18}$$

$$\frac{\partial B_c}{\partial V_{ss}} = \frac{\frac{\partial T}{\partial t_1} \rho_s c_s}{\frac{\partial T}{\partial t_2} - \frac{\partial T}{\partial t_1}} \tag{19}$$

$$\frac{\partial B_c}{\partial V_{Ls}} = \frac{\frac{\partial T}{\partial t_2} \rho_s c_s}{\frac{\partial T}{\partial t_1} - \frac{\partial T}{\partial t_2}} \tag{20}$$

Physical Experimental Design

Housing Fixture

The micro DTA experimental design allows for direct thermocouple placement upon the biological sample, quick and easy deposition of the sample into the crucible, and a controlled environment for repeatable measurements. The test section is built around a microscope stand for observation of thermocouple placement, sample deposition, and sample observations during cooling procedures as shown in Fig. 12. The DTA bridge housing is designed to improve repeatable cooling conditions to the micro-DTA bridge by sufficiently insulating the DTA from the environment and providing a controlled humidity environment. The housing encloses and insulates the cold block along with the thermoelectric element and bridge while providing access ports for the microscope, thermocouple, micropipette, humidity sensor, dry air inlet, and dry air outlet as shown in Figs. (13-15). The housing fixture was designed in SolidWorks and fabricated using selective laser sintering (SLS), a rapid prototyping process to reduce costs from the complicated geometries involved. Most of the complicated geometries arose from the hallow cavities within the housing; these cavities were later filled with expanding insulating foam for a sufficient insulating scheme.

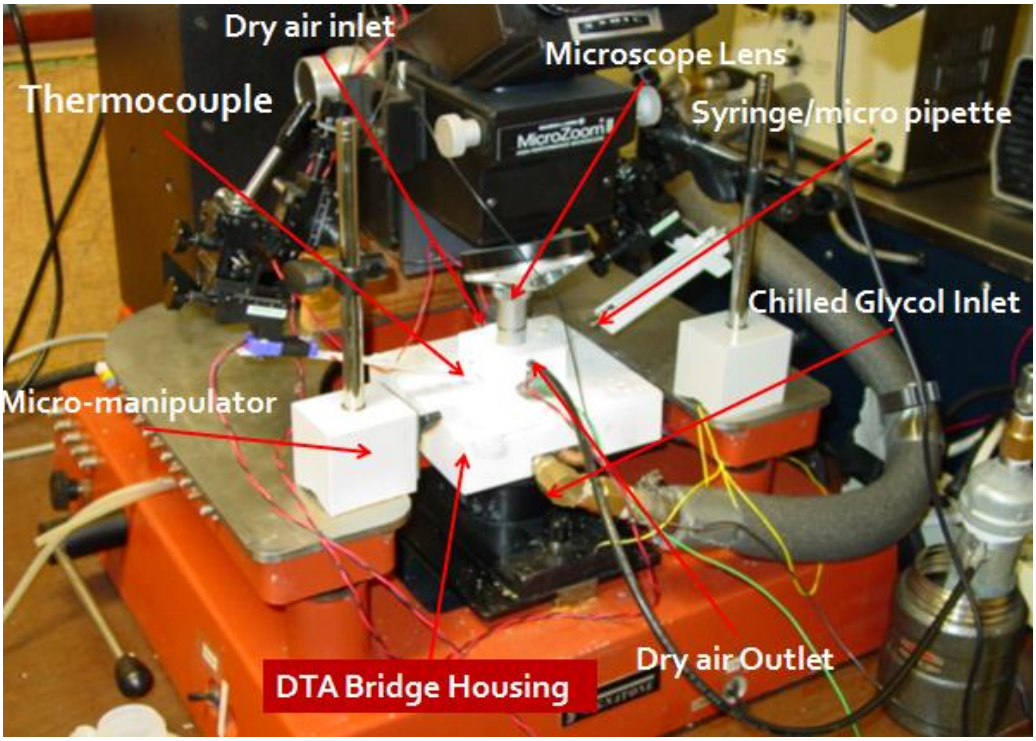

Figure 12. DTA test section setup

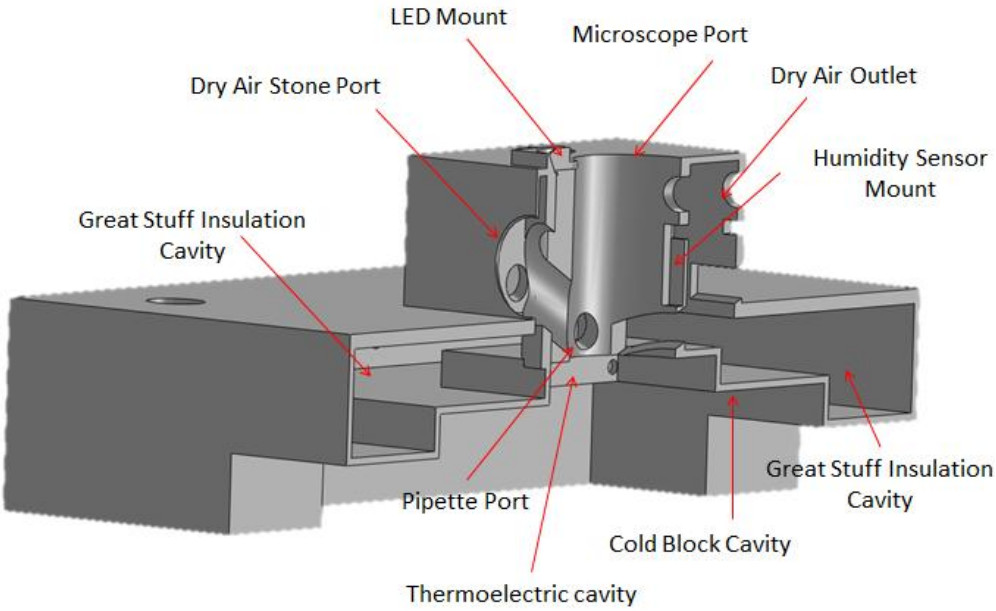

Figure 13. Side sectional view of DTA housing

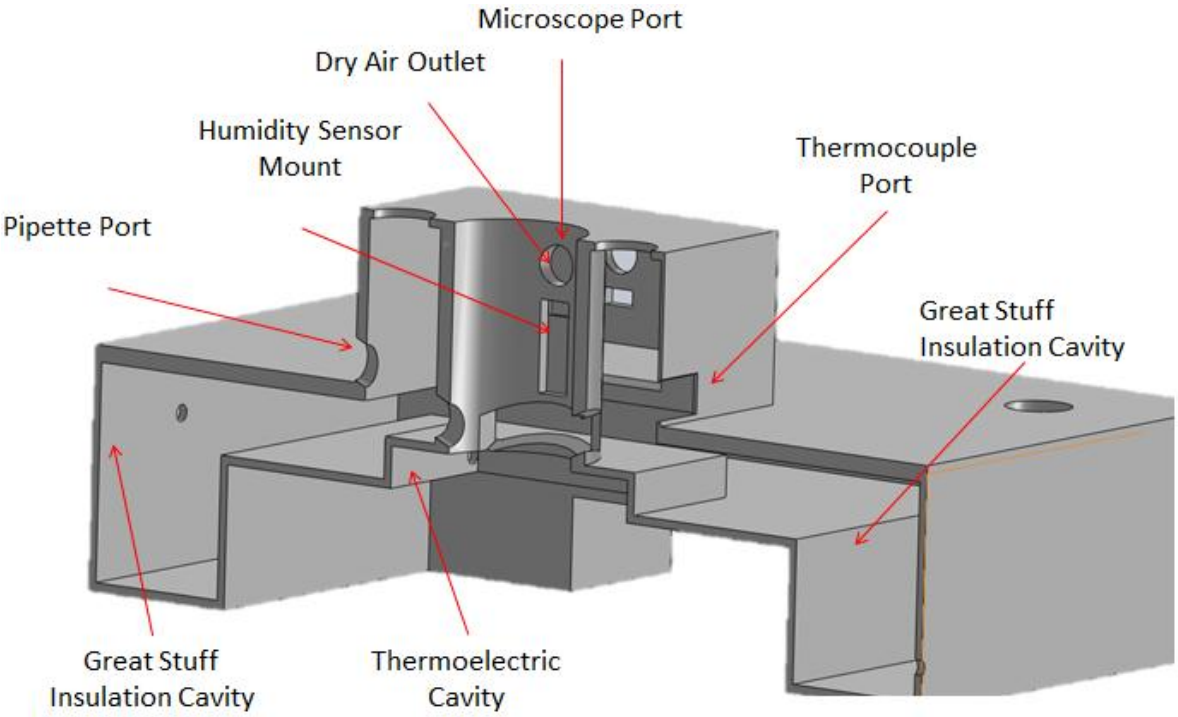

Figure 14. Rear Sectional view of DTA housing

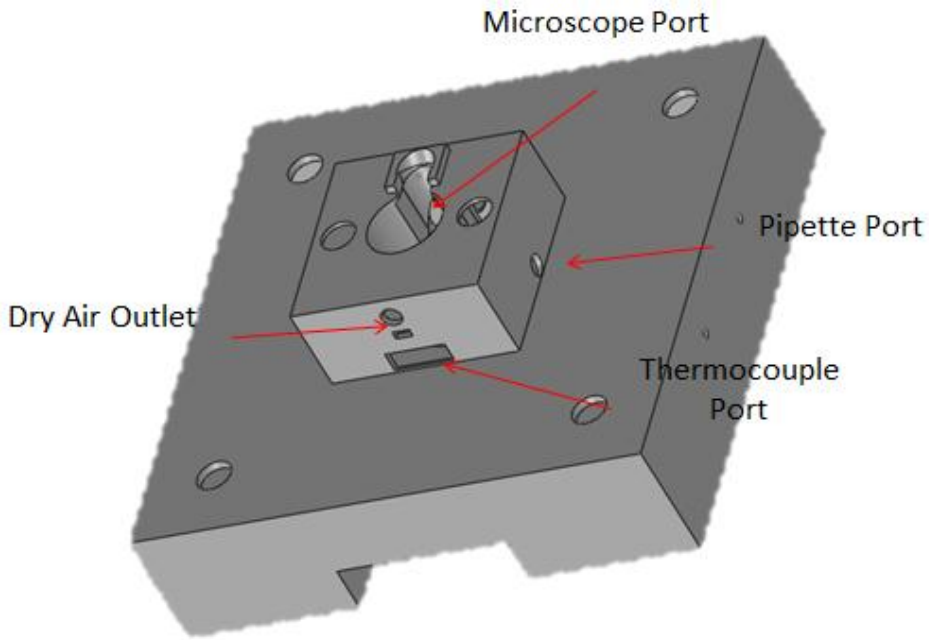

Figure 15. DTA Housing Front View

Thermocouple

The measuring system chosen was an Omega 25 micron diameter type E (chromel–constantan) thermocouple due to its high sensitivity output and also poor thermal conductivity to minimize interference within the system. The small size of the thermocouple is able to achieve response times as low as 5 milliseconds which is crucial for measuring the endothermic or exothermic graphs of the micron sized oocyte cells. To minimize the chances of damaging or destroying the micron sized thermocouple beads the handling procedures involved minimal movement of the thermocouple. The thermocouple was permanently secured to the packaging using tape that the thermocouple was originally adhered to. A type E thermocouple connector was then secured to the packaging while installing the thermocouple leads to the appropriate connectors. Then the end of the packaging was carefully removed with an x-acto knife to expose the thermocouple bead. The end design of the thermocouple packaging fixture

was to use it as a probe to insert into the housing fixture thermocouple port using micromanipulators.

Micropipette

To deliver liquid samples and oocyte cells to the crucible custom made micropipettes were constructed using a method of heating and expanding. 1mm diameter micropipettes were heated using a propane-torch until the glass glowed orange. Then the pipettes were removed from the flame and pulled while glowing until the desired thickness was achieved. Typically, the pipettes used for oocyte handling ranged between 150-200 µm in diameter while the pipettes used to deliver water samples were 25-50 µm diameter. The smaller diameter sized pipette was needed to more precisely deliver a smaller liquid sample volume size for the deposition of the lesser volume. To achieve the smaller diameter sizes two different heating stretching procedures were used. The micropipettes proved to be an effect tool to deliver the controlled volume of sample to the crucible.

Cold Trap

To effectively control the calorimeter's atmosphere, dry air was purged into the DTA housing until the relative humidity within the housing reached 15-17%. The controlled humidity environment decreased the amount of frost that collected upon the bridge during the final cooling phases. The minimization of frost allowed for a more controlled cooling environment, which improved repeatability within the system. Dry air was achieved by utilizing a cold trap that effectively traps the moister within the humid air by allowing the water within the air to condense within the trap as shown in Fig. 16. A pump was used to vacuum dry air from the 253 K chilled cold trap and then deliver the dry air to the DTA housing cavity through an air stone. The air stone was used to

distribute the dry air within the cavity and to minimize the air stream from damaging the thermocouple and bridge, the location of the air stone is shown in Fig 13 above. An airline was then routed from the DTA housing to the cold trap to attempt a closed circuit air stream to improve the cold trap's efficiency. Figure 15 illustrates a diagram of the dry air circuit below.

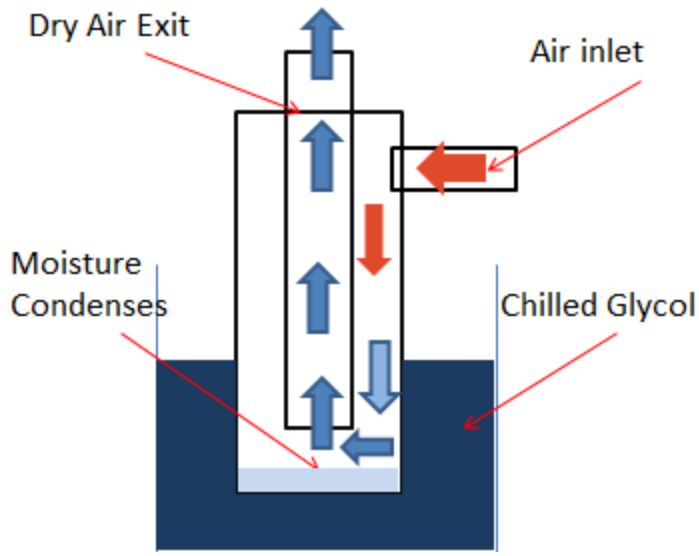

Figure 16. Cold Trap to deliver dry air to DTA housing.

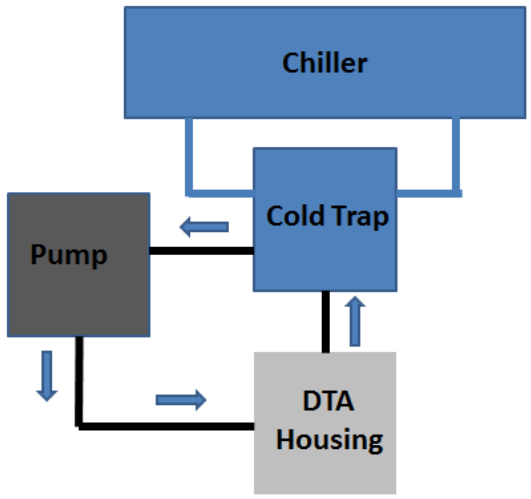

Figure 17. Dry air system

Humidity Sensor

The relative humidity is then measured through a HIH-4000 humidity sensor that is mounted within the cavity of the DTA housing as shown in Fig. 13. An Arduino Uno microcontroller provides a 5V input while also reading the sensor's analog output signal. The Arduino then converts the output signal into readable relative humidity values using a calibration equation supplied by the manufacturer. The calibration equation is also dependent upon temperature for which a constant temperature is used only during the initial warming and purging phase before the experiment is ran. The humidity sensor is used to determine when steady state relative humidity is reached to begin the experiment.

Outer Enclosure Box

Air motions within the laboratory induce errors in the temperature measurement process due to the very sensitive thermocouple used. To shield the experimental setup an outer enclosure box was designed and built as shown below in Fig. 18. The enclosure box provides a viewing window to observe the position of the instruments and equipment to ensure proper experimental setup is performed. A small access door is also provided to manipulate the micropipette for sample placement before an experimental run. After implementing the outer enclosure box experimental results showed excellent repeatability.

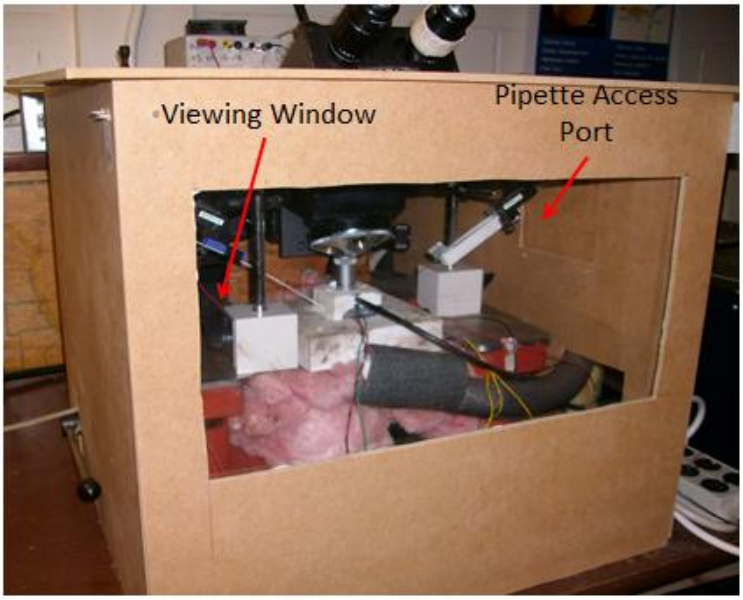

Figure 18. Outer Enclosure Box

Microscope Camera

To visually record the sample during the entire experimental run an 8MP 1080P Microscoft web cam was custom fit to the microscope viewing lens. The camera can either take high-resolution photos of the sample within the crucible for volume extraction purposes or capture the freezing process of the cell with 1080P high definition video. The microscope camera has proved to be an invaluable tool to utilize during experimental procedures and also during the initial phases of procedure development.

Control System Experimental Design

The cooling profile was controlled using an off –the- shelf thermoelectric module coupled with an industrial chilled cold block. The thermoelectric module was used as the main temperature control device by inputting an electrical current profile from an Agilent power supply to achieve the desired temperature output. The cold block was used as the gross cooling source with the coolant temperature kept constant throughout the experiment at 251K. Determining the correct electrical current profile to achieve the desired cooling rate required the development of a numeric model of the DTA

experimental setup. The model was based off of Patankar's control volume theory for computational fluid dynamics (CFD) (Patankar 1980). The model was then coupled with an optimization algorithm to minimize the difference between the numerical model output temperature and the desired temperature profile (objective function) by altering the electrical current input (design variable).

Numerical Model Development

Control Volume Theory

A 1-D conduction type transient control volume theory based numeric model was developed in Matlab for the purposes of modeling the DTA experimental system. The theory used was borrowed from Pantaker, which warrants a brief description of the methods used to discretize the system. The theory is based on conservation of energy applied to a finite control volume as shown in Fig. 19. The control volume theory states that the rate of accumulation of extensive property EP inside of the system at time t equals the rate of transport of EP into the system minus the rate of transport of EP out of the system. The accumulation of EP inside the system also accounts for the rate of generation of EP inside the system minus the rate of consumption of EP inside the system. The control volume theory just explained can be simplified and described in Eq. 21 below. The first term of Eq. 21 on the RHS is the rate of accumulation of extensive property where ρ is the density (extensive property) and φ is the arbitrary intensive property. The second term on the RHS is the advection term where $\vec{u}$ is the velocity component. The first term on the LHS of Eq. 21 is the diffusion term where Γ is the constitutive property of the substance, such as thermal conductivity k for thermal energy transport. Lastly, the last term of Eq. 21 is the total volumetric source term S

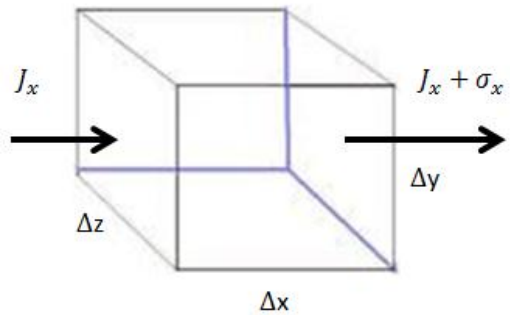

Figure 19. Conservation Framework

$$\frac{\partial \rho \varphi}{\partial t} + \nabla \cdot (\rho \vec{u} \varphi) = \nabla \cdot (\Gamma \nabla \varphi) + S \tag{21}$$

Discretization of Control Volume

The objective of Pataker's method is to discretize Eq. 21 into algebraic equations and then apply one equation for each control volume. Each control volume solution φ_P is influenced from its immediate neighbors $\varphi_N, \varphi_S, \varphi_E, \varphi_W, \varphi_T, \varphi_B$ solutions along with its and constants as depicted in Eq. 22 and Fig. 20 below.

$$\varphi_P = f(\varphi_N, \varphi_S, \varphi_E, \varphi_W, \varphi_T, \varphi_B) + Const \tag{22}$$

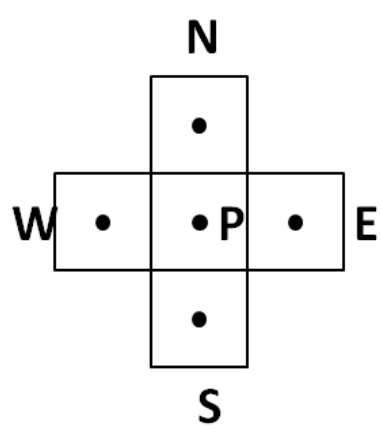

Figure 20. 2-D discretized control volume layout

Discretizing Eq. 21 involves assuming linear trends between values of φ so that when the control volume is small enough the discretized solution will approximate the exact solution of the discretized equation. The developed numeric model used in this paper approximates a 1-D geometry scheme therefore for brevity purposes a 1-D algebraic discretization description will be necessary. The stagnant 1-D transient simplified version of Eq. 21 is described below in Eq. 23. Using the 1-D control volume setup as shown in Fig. 21 and assuming linear functions between the nodal values of φ, Eq 23 can be integrated to obtain Eq. 24. As described earlier the temperature T_P is a function of the neighboring temperaturesT_E, T_W the temperature of the previous time step $T_p{}^o$, the source term S and the constants $\frac{\rho c \Delta x}{\Delta t} + \frac{k_e}{\delta x_e} + \frac{k_w}{\delta x_w}$ as shown in Eq 24. The source term is split into a temperature dependent source term S_p and temperature independent source term S_c as shown in Eq 25.

$$\int_w^e \rho c \frac{\partial T}{\partial t} dx = \int_w^e \left[\frac{\partial}{\partial x}\left(k \frac{\partial T}{\partial x}\right) + S\right] dx \tag{23}$$

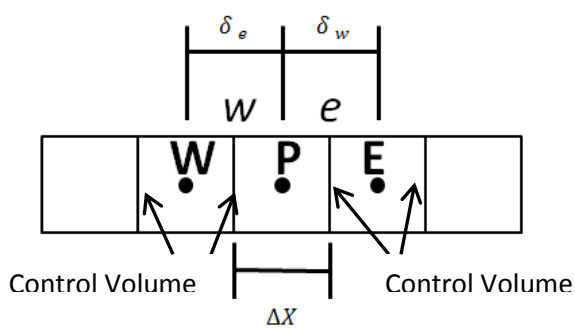

Figure 21. 1-D discretized control volume setup

$$\left(\frac{\rho c \Delta x}{\Delta t} + \frac{k_e}{\delta x_e} + \frac{k_w}{\delta x_w}\right) T_P = \frac{k_e}{\delta x_e} T_E + \frac{k_w}{\delta x_w} T_W + \frac{\rho c \Delta x}{\Delta t} T_p{}^o + S \Delta x \tag{24}$$

$$S = S_c + S_p T \tag{25}$$

Custom Model Case Check

To ensure the accuracy of the created numeric model a few cases were compared with three simple analytical solutions that encompass similar scenarios that the numeric model will encounter. The three case checks were constant temperature boundary conditions with varying material layers, constant temperature boundary conditions with heat generation terms, and transient with constant temperature boundary conditions.

The steady state constant temperature boundary condition with varying material layers check consisted of one side of the simulated block being held at 300K while the other was 500K. The model was 9 meters long and split into 5 different layers with all the same conductivities of 1.5 W/m except the middle layer which was 6 W/m for layer communication insurance. The numeric model was run with different mesh sizes until mesh independence had occurred. The results of the constant temperature boundary conditions are presented below in Table 1 where the solutions to the numeric simulation matched the analytical solutions almost exactly with a maximum percent error of 0.01%.

Table 1 Steady State constant temperature boundary condition case check results

Position (m)	**0**	**1**	**2**	**7**	**8**	**9**
Numeric (K)	499.3	461.9	424.7	377.7	340.2	302.8
Analytical (K)	499.30	461.87	424.44	377.66	340.23	302.81
Percent Error	0.00035%	0.00620%	0.06021%	0.01037%	0.00997%	0.00232%

The second case check was a steady state constant temperature boundary condition with a heat generation term within the middle of the model. The constant temperature boundary conditions were 500 K and 300 K along with a constant heat generation term of 99999 W. The total length of the simulated block was 0.04 m and split into 4 different layers with a constant thermal conductivity of 1.5 W/m at each layer.

The numeric model was run until mesh independence was achieved. The results of the heat generation term case check are presented below in Table 2 where the numeric simulation results match the analytical solution very closely with a low percent error of 0.008%.

Table 2 Heat generation term case check

Position (m)	0.01	0.02	0.03
Numeric (K)	460	413.3	360
Analytical (K)	459.99	413.33	359.99
Percent Error	0.00217%	0.00774%	0.00278%

The last case check involved a constant temperature boundary condition transient problem. Each side of the simulated block was held at 0 K with an initial condition of 50 K. The thermodynamic properties were held constant throughout the 3.142 meter span of the simulated block with the thermal conductivity, density, and specific heat each held at 1 W/m, 1 kg/m^3, and 1 J/kg. Two different temperature span checks were made at 100 seconds and 200 seconds for both numeric and analytic models. The transient case check simulation results are presented below in Table 3, both the numeric and analytical results agree with each other within a 0.53% error span.

Table 3 Transient case check simulation results

Position (m)	0.5	1	1.5	2	2.5
Numeric K @ 100s	22.57	39.62	46.95	42.79	28.17
Numeric K @ 200s	8.343	14.65	17.36	15.82	10.41
Analytical (K) @ 100s	22.69	39.81	47.19	43.02	28.32
Analytical (K) @ 200s	8.344	14.65	17.36	15.83	10.42
Percent Error @100s	0.53%	0.48%	0.51%	0.53%	0.53%
Percent Error @ 200s	0.01%	0.00%	0.00%	0.06%	0.10%

Numeric Model

The 1-D numeric model of the controlling thermoelectric module required that layers of different materials along with cooling and heating source terms to simulate both the thermoelectric module along with the micro-bridge and thermocouple as shown in Fig. 9 above. The layered model created is shown in Fig. 22 below, the associated thermodynamic properties used in the simulation are shown in Table 4.

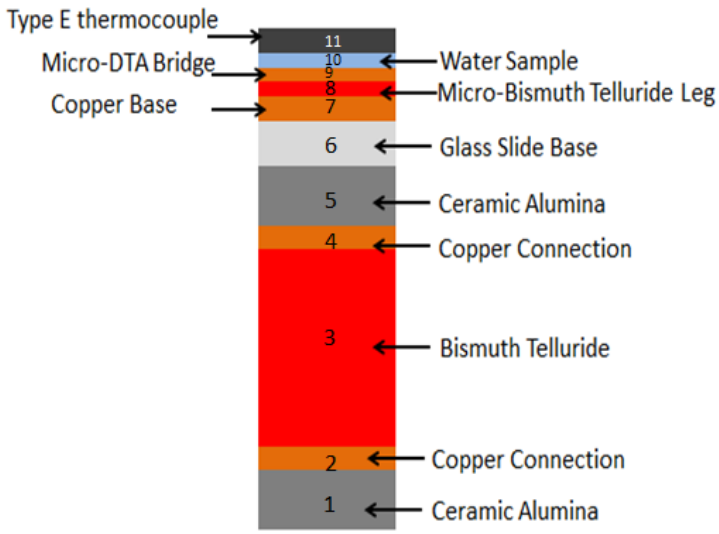

Figure 22 Numeric Model Layering Scheme

Table 4. Numeric model layering thermodynamic values

layer	1	2	3	4	5	6	7	8	9	10	11
k (W/m^2)	35	401	1.48	401	35	14	401	12	401	0.569	38.6
rho (kg/m^3)	3750	8960	7700	8960	3750	2225	8960	7700	8960	1000	8730
cp (J/Kg*K)	775	390	122	390	775	835	390	122	390	4217	0.8054
length (mm)	0.68	0.432	1.27	0.432	0.686	0.152	0.152	0.5	0.3	0.01	0.025
nodes	500	600	1200	600	500	500	500	800	600	600	600

The main temperature control of the DTA system employed a thermoelectric module, a solid state cooler/heater which utilizes Peltier technology. A single thermoelectric is comprised of two electrically dissimilar materials connected electrically in series with a metal electrode (Karimanal, Ellsworth, Jr. and Refai-Ahmed 2003). Electric current passing through the junctions where the two materials meet either absorbs or liberates

heat at the junction and is due to the Peltier effect. The absorption q_{PC} or liberation of heat q_{PH} is dependent upon the direction of the electrical current I passing through the junction, the temperature at the junction T and the Seebeck coefficient σ of the two materials as shown in Eqs. (26-27). There also exists a joule heating term q_J throughout the dissimilar materials that is dependent upon the current density applied and the electrical resistivity of the material ρ_e shown in Eq. 28 below.

Source Terms

The Peltier cooling and heating terms described in Eqs (26-27) are used in the temperature dependent source terms of the nodal equations in the numerical model. The peltier cooling and heating terms will be applied at the two control volumes surrounding the junction of the bismuth telluride piece and copper connection to simulate liberation and absorption of heat. The peltier cooling term was applied at the upper junction whereas the peltier heating term will be applied to the lower junction as shown in Fig. 23 below. The joule temperature independent heating source term in Eq. 28 will be used throughout all of the nodal equations throughout the bismuth telluride piece and both copper connections as shown in Fig 23. The source term properties used for the numeric model are presented in Table 5 below.

$$q_{PC} = S_p = -2\sigma IT \tag{26}$$

$$q_{PH} = S_p = 2\sigma IT \tag{27}$$

$$q_J = S_C = J^2\rho_e \tag{28}$$

Table 5. Source Term Properties

	Bismuth Telluride	Copper
Electrical Resistivity (ohm-m)	8.82E-06	1.68E-08
Seebeck Coefficient (V/K)	1.92E-04	NA

Boundary Conditions

Two different boundary conditions will be used on the outer nodes for the numeric model. The first boundary condition will be a constant temperature boundary condition of 251 K on the lowest node to simulate the cold block while the second will be a convection boundary condition on the upper node. The convection boundary condition term was assumed to be purely natural convection since the system was well insulated from the environment. The natural convection is due to buoyancy forces caused from temperature differences between the warm ambient air relative to the cold air near the surface of the thermoelectric. The average Nusselt number empirical correlation for an upper surface of a cold plate is described below in Eq. 29 where Ra_L is the Rayleigh number. The Rayleigh number is a correlation between the thermal expansion coefficient β_t, characteristic length L, acceleration due to gravity g, thermal diffusivity α, kinematic viscosity ν, and the difference between the surface and ambient temperature as stated in Eq. 30. The average heat transfer coefficient due to natural convection is shown in Eq. 31 where k is the thermal conductivity of the air and will be used as the temperature dependent source term at the boundary as shown in Fig 23 below. The natural convection properties used for the numeric model are cataloged in Table 6. below.

$$\overline{Nu}_L = 0.27 Ra_L^{0.25} \tag{29}$$

$$Ra_L = \frac{g\beta_t(T_s - T_\infty)L^3}{\alpha\nu} \tag{30}$$

$$\overline{h} = S_p = \frac{\overline{Nu}_L k}{L} \tag{31}$$

Table 6. Natural Convection Properties

Characteristic Length (m)	3.48E-04
Thermal Expansion Coefficient (m) (1/K)	3.47E-03
Thermal diffusivity (Air) (m^2/s)	1.45E-05
Kinematic Viscosity (Air) (Kg/s*m)	2.06E-05
Thermal Conductivity (Air) (W/m*K)	2.40E-02

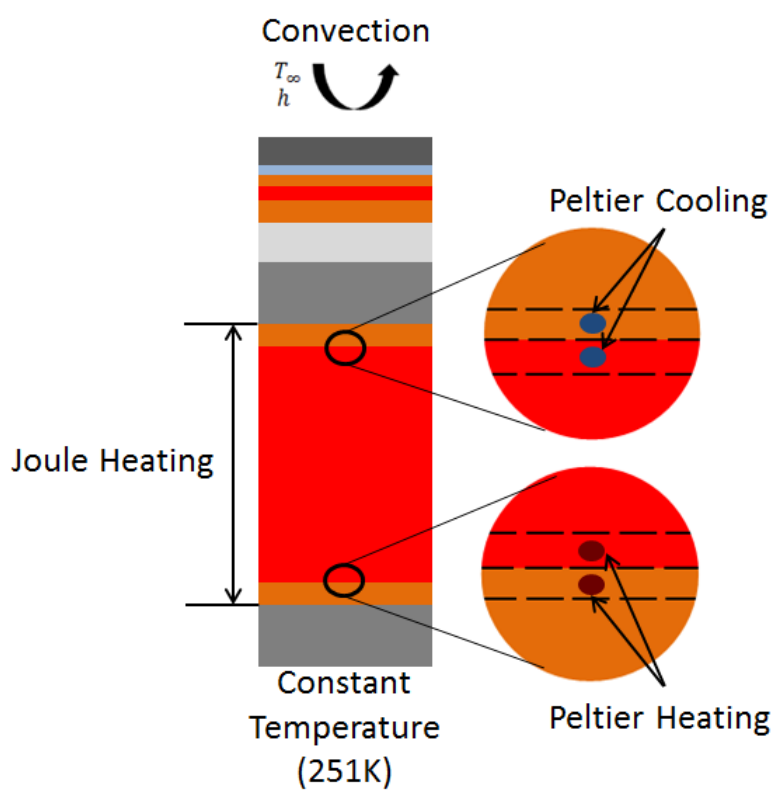

Figure 23 Boundary Conditions & Source Terms

Calibration

Within the experimental DTA setup unknown convection terms exist that affect the temperature at the thermocouple that is not accounted for within the natural convection terms. The numerical model is an idealized case of the DTA experimental

setup therefore a correction term must be implemented in order to match the model with the DTA experimental setup. A calibration convection term is implemented into the model at the boundary as shown in Fig 23. An optimization algorithm is utilized to match the numerical model temperature output to an experimental calibration run by changing the convection term within the constraints. The experimental calibration run consisted of inputting a constant current of 2 amps in heating mode into the thermoelectric module and recording the transient temperature of the bridge from a cold steady state temperature to the next warmer steady state temperature.

The calibration program utilized an optimization program (Matlab's fmincon) to minimize the difference between the calibration run and numerical model by changing the calibration design variable under bound constraints. The design variable used in the optimization algorithm is the convection term. The design variable upper constraint is based off of typical values of condensing water vapor (5000 W/m^2K) and lower bound constraint of no convection (0 W/m^2K). The calibration program was also under a nonlinear constraint to ensure the numerical model achieved steady state by calculating the standard deviation of the last 50 time steps based off of the experimental calibration run. If the standard deviation was ≤ 0.01 then the numerical model temperature output was assumed to have achieved steady state. The calibration program specifically looked at the steady state temperature of both the numerical model and experimental calibration run's output and minimized the difference of the two. The calibration program was run every time the system changed either by switching out the micro-bridge, thermoelectric module, or after a week without running.

Initial Condition

Initially, the thermoelectric module was switched to heating mode (reversing the current) to raise the temperature of the DTA bridge to 288K from 251K (cold block temperature) using approximately 2 amps of current before each experiment. To determine the initial temperature distribution within the nodal array a numeric simulation was run with 2 amps of current running in heating mode for 15 seconds with a time step of 0.05 seconds. The nodal temperature distribution was then imported into an excel document to be imported into the model prior to each simulation.

Control System

A numeric control system was developed based off of the DTA 1-D transient numeric model to determine the correct electrical current profile to be imported into the thermoelectric module to produce the desired temperature profile. A built in Matlab optimization algorithm (fmincon) was utilized to search for the optimal current input to minimize the objective function subject to design variable constraints. In this case the objective function F_{obj} is the absolute value of the difference between the numeric model temperature output T_{cs} and the desired temperature T_d as shown in Eq. 31. The only design variable for the DTA control system is the electrical current input I and subject to constraints $0 \leq I \leq 5.5$. For most cases a linear cooling temperature profile was developed as the desired cooling profile. The control system encompasses both the heating and cooling mode of the thermoelectric module to produce the desired linear cooling temperature profile throughout the entire range of 288 K to 225 K. Initially, the simulation starts at 288 K with the control system being in heating mode to compensate for the 251 K from the cold block and incrementally steps the current down until the current becomes zero. When the current reaches a null value the control system switches

the direction of the current and then incrementally increases the current until 5.5 amps has been reached (current constraint).

$$F_{obj} = (T_{cs} - T_d)_{abs} \tag{31}$$

Control System Results

The numeric control system produced an electric current profile along with warming and cooling mode flags to be imported into the power supply being used to drive current into the thermoelectric module. A 1 K/sec cooling profile was imported into the numeric control system to produce the desired current profile. The 1K/sec current profile was then implemented into the power supply and ran which produced a 0.7841 K/sec linear cooling profile with an R squared value of 0.9999 as illustrated in Fig. 24 below. To demonstrate the true capabilities of what the numeric control system is able to achieve a 1 K/sec sinusoidal cooling profile was produced and illustrated in Fig 25 below.

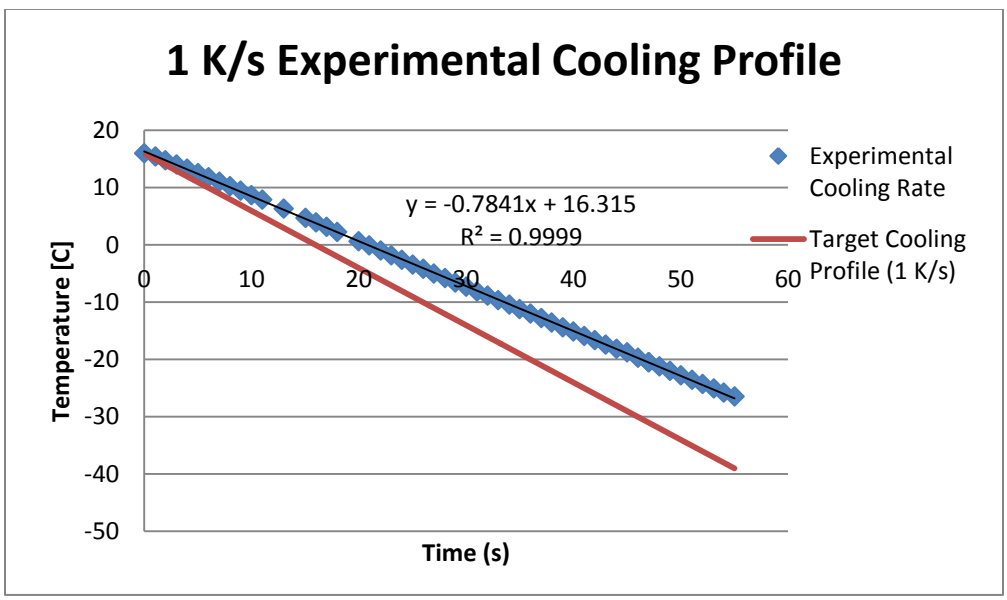

Figure 24 1K/sec cooling profile produced from the current profile determined by the numeric control system

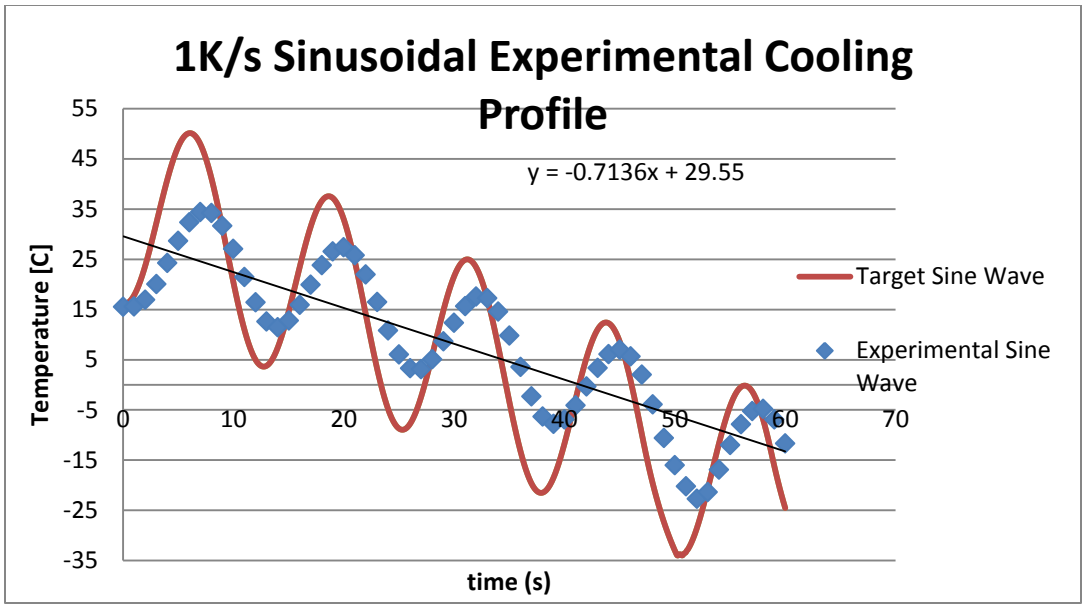

Figure 25. 1K/sec sinusoidal cooling profile produced from the current profile determined by the numeric control system

Experimental Procedures

The experimental procedures for collecting calorimetric data from the micro-DTA system were developed through extensive training on manipulating microscale systems. First, the newly built bridge was placed carefully on the thermoelectric module with the application of silver thermal paste to minimize thermal resistances between the bridge and module. The housing fixture along with the thermoelectric module was then placed upon the cold block while insuring that the thermoelectric module is in good thermal contact with the cold block with the application of thermal grease. The microscope light was then turned on and the microscope optic was then lowered down into the microscope port in the housing fixture until the bridge came into focus. If the bridge was not in clear view then the housing fixture was then removed and the bridge was repositioned until it was visible using the microscope.

Thermocouple Placement

After bridge placement the next step was to position the thermocouple within the crucible to take temperature measurements of the sample. The thermocouple was chosen to not be permanently secured to the crucible to allow freedom to position the thermocouple as close to the oocyte cell as possible to maximize sensitivity. The 25 micron diameter type E thermocouple was clamped and secured within the Narishige micro-manipulator and placed near the entrance of the housing fixture thermocouple port. The thermocouple was then slowly positioned within the housing fixture by adjusting the control knobs on the micro-manipulator until the thermocouple bead came in view through the microscope. The thermocouple bead was then slowly lowered into the cavity of the crucible until contact has occurred. The manipulator was then slightly moved side-to-side to ensure that the thermocouple bead was in good contact within the bowl by observing that the bead was static during the movements as shown in Fig 26. Positioning of the thermocouple in the desired location within the crucible proved to be difficult to not damage or destroy the thermocouple or bridge during the process.

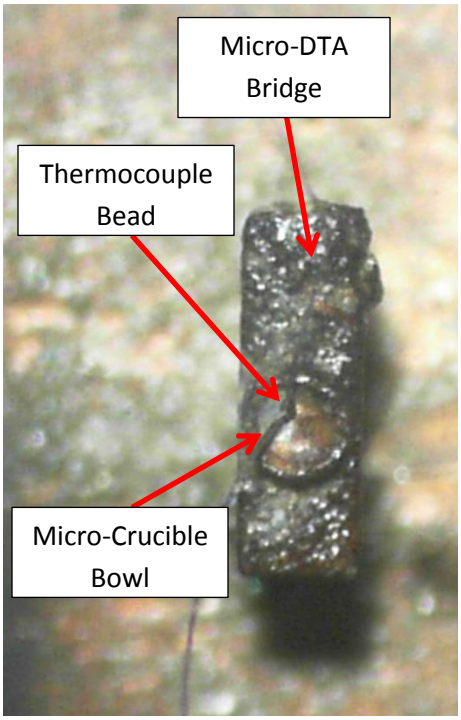

Figure 26. Thermocouple placement in Micro-DTA bowl shaped Crucible

Micro-pipette placement

The next step was to position the micro-pipette to either deposit a calibration liquid or biological sample within the crucible. The custom made micro-pipette was secured within an oil eppendorf cell tram pipette holder. Then the pipette holder was then secured within a custom built pipette holder fixture to more effectively secure the pipette holder to another micro-manipulator. The micro-manipulator was then placed on the other size of the housing fixture while insuring that the pipette was in line with the pipette port. The pipette was then slowly positioned within the housing fixture using the control knobs on the micro-manipulator until the pipette came in view. The pipette was then slowly positioned until the tip was within the crucible. It was essential for the tip to be in contact with either the thermocouple or the contour of the crucible to assist in the deposition of the calibration liquid or oocyte. In order to successfully deposit the sample there seemed to be a need for a seed point for the deposited liquid to adhere to or the

droplet will attach to the pipette causing difficulty for deposition. After the pipette height adjustment has been determined, the pipette was then backed away from the crucible to prevent damages from occurring during the cooling and de-humidification process.

Chiller and Equipment Preparation

Once the thermocouple and pipette have been positioned in the desired locations the industrial chiller was turned on and temperature set at -27 °C which was the minimum temperature that chiller could operate with the provided glycol solution. The thermoelectric module was then set to heating mode and powered with 1 A to prevent ice crystals from forming on the bridge and thermocouple. The crystals could damage the bridge by dislodging the bridge base from the legs due to ice crystal expansion. The industrial chiller will cool for about 2 hours until it has reached a steady state temperature of -27 °C. During the chiller down time the digital multi-meter (DMM), and both power supplies were turned on to ensure that the systems will be properly warmed for accurate data collection. The outer enclosure box was usually installed before the chiller hoses froze to ensure proper alignment after the hoses were immovable. Once the chiller has reached steady state the dry air pump was turned on to purge the DTA housing cavity with dry air. The pump was run until the relative humidity has reached a steady state humidity of 15-17% then switched off to position the pipette into place through the outer enclosure pipette access port as illustrated in Fig 18. After the cooler and relative humidity has reached steady state the experimental system was ready for sample deposition followed by cooling and data collection.

Liquid Sample deposition

The sample liquid volume being deposited depended upon which experimental run that was being performed. During the baseline run procedure a volume amount that

was significantly below the top edge of the crucible was deposited while insuring that the liquid sufficiently wetted the thermocouple within the crucible. During the sample run procedure the crucible was filled to the top edge of the crucible while insuring the liquid was not overflowing above the lip of the container. Once the sample was successfully deposited within the crucible the microscope camera was set to video record the sample within the crucible for volume extraction purposes. Then the chiller was turned off while keeping the glycol circulating and then the control system and data collection process began. In both cases the pipette was left in the liquid until the experiment has initially ran to approximately -5 °C to prevent excessive evaporation. Once the pipette was removed from the liquid the outer enclosure box's pipette port was covered with the door to prevent ambient disturbances from affecting the data collection series. Once the experimental series was complete, the chiller and dry air pump was turned on for preparation of the next experimental series.

Oocyte Sample

Oocyte preparation

Bovine oocyte cells were used as the standard model for the cryopreservation characterization procedures. The cells were transported from the animal science center to the characterization lab within a thermous filled with 37 °C (body temperature) water. The cells were then individually picked up within the cellular solution using a 100 µm pipette and placed in an enzyme solution to help remove the granular cells that are attached to the oocyte. The cells were "washed" within the enzyme solution by catching and releasing the cells using the pipette to physically remove the granular cells. Once the oocytes were cleaned they were then placed back into the original solution container and placed in 37 °C water for storage purposes.

Oocyte deposition

Procedures for the deposition of the oocyte cells were very similar to the deposition of the liquid samples. The difference between the cells and liquid samples is the size of the micro-pipettes used for the experimental procedures. DI water was used as the smaller sample for the base-line run for an oocyte cell series because cell solution is composed mainly of water thus also having similar thermal conductivities to achieve the same thermal resistances. However, if a cryoprotectant agent was used as the base-line smaller sample since common CPAs have been characterized (Han, Devireddy and Bischof 2002). After the experimental run was complete the cells were deemed useless due to IIF damage and removed by the micropipette method.

Volume Abstraction

Determination of the sample volume is a critical factor in characterization and calibration of the calorimetric system. As stated before the volume was abstracted through an imagery program by using a correlation between the diameter and volume of the crucible. An optical profilometer was used to characterize the volume and shape of the crucible. Using built in analysis tools four different contour profiles of the crucible profile (depth vs length) and a volume profile (volume vs height) was exported to CSV files for further analysis.

The contour profile data was then manipulated in an m-file created in Matlab to produce a correlation between diameter and height and saved in an XLS file to import in a custom volume calculator written in Matlab. The volume calculator imported the XLS data files and required a user input that consisted of a diameter and its associated t-test uncertainty to find the associated volume. The volume finder linearly interpolates between the height as a function of diameter profile using the user inputted diameter and then interpolates

again to find the associated volume as a function of height from the volume profile. The program then outputs the associated volume along with its associated total t-test uncertainty. The code for these programs can be found in the appendix.

Diameter Abstraction

Determining the volume for the proposed setup requires the input of the measured diameter of the water sample within the crucible. ImageJ was used to abstract the diameter measurements of the sample. Measurements of the crucible were obtained using a stage micrometer to later use as a calibration standard for diameter measurements before the bridge and crucible were mounted into the DTA housing. Once the sample was deposited within the crucible cavity a still photo or a snap shot of a video recording was obtained to import into Image J. The cylinder diameter was used as the known calibration constant to abstract the sample diameter within the crucible. Twenty-five independent measurements were obtained to calculate the associated sample diameter average and t-test uncertainty as inputs for determining the volume.

Procedure Conclusion

The experimental procedures that were described required an extensive amount of practice and experience on handling and manipulating micro-scale sized structures and objects. The majority of the time spent was developing new procedures, tools, and techniques to achieve a repeatable process without the result of damaged equipment. The majority of the equipment used was custom designed and altered to help alleviate the steep learning curve requirement for successful micro-scale experimental preparation. The current procedures have proved to be successful on delivering reliable, accurate, and repeatable experimental results while minimizing the probability of equipment destruction.

Chapter 4. Micro-DTA of Micro-Sample Results

Nano-liter samples of DI water were chosen to display the micro-DTA's capability of achieving accurate and repeatable exothermic and heat capacitance results for future characterization of oocyte cells. The main objective of the proof-of-concept micro-DTA was to prove that trials could be repeatable meaning that the temperature profiles of similar sample masses share similar slopes, freeze relatively at the same temperature, and share comparable exothermic peaks. The first results section will display repeatability in trials, the second section will present the specific heats based upon the differential mass method in Eq. 14 above while the third results section will concentrate on freezing temperatures and exothermic releases.

Repeatability of Dry run Trials

In order to proceed towards sample based experiments the validity of repeatability needs to be proven to satisfy Eqs (11-14) above. Five different dry run trials were performed with 15 minute relaxation times in between experimental runs were ran to test that the system was repeatable and also at steady state. Each test involved heating the bridge momentarily to 60 °C and then cooled down to 15.5 °C to ensure all moisture has evaporated while running the dry air pump until the relative humidity reached a steady state of 21% humidity. The current profile produced from the numeric control system for 1 K/s was imported into the experimental control system to run each experiment at a 60 Hz sampling rate.

The cooling profiles for each dry experimental run were plotted against one another to illustrate the repeatability of the system as shown in Fig. 27 below. Each cooling profile resulted in a -1.13 K/s temperature rate with an R value of 0.9965. The

trials were then compared against the first trial to determine the temperature difference from the initial profile and displayed in Fig. 28 below. Trials 3, 4, &5 seemed to have deviated away from the first trial but have reached a steady state of around 0.35 K difference from the first trial. Every trial has managed to stay below a 1K temperature difference which is within the thermocouple's uncertainty specified by the manufacture (Omega). The dry run results have concluded that the validity of the systems repeatability has been proven to be effective. Therefore further assumptions of repeatability for further experimentation can be valid.

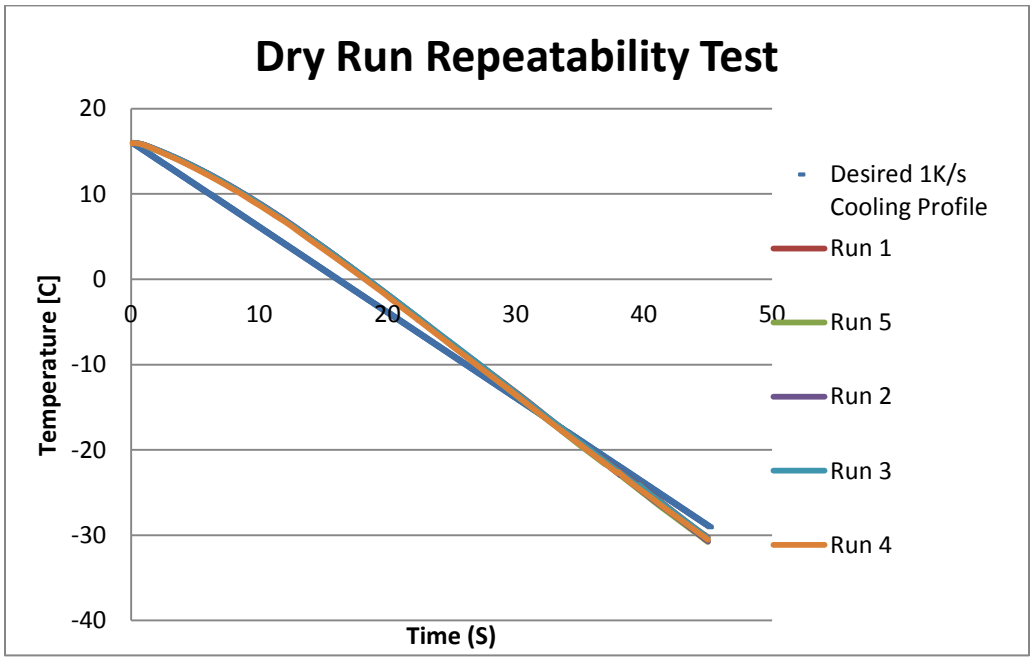

Figure 27. Dry Run to Validate System Repeatability

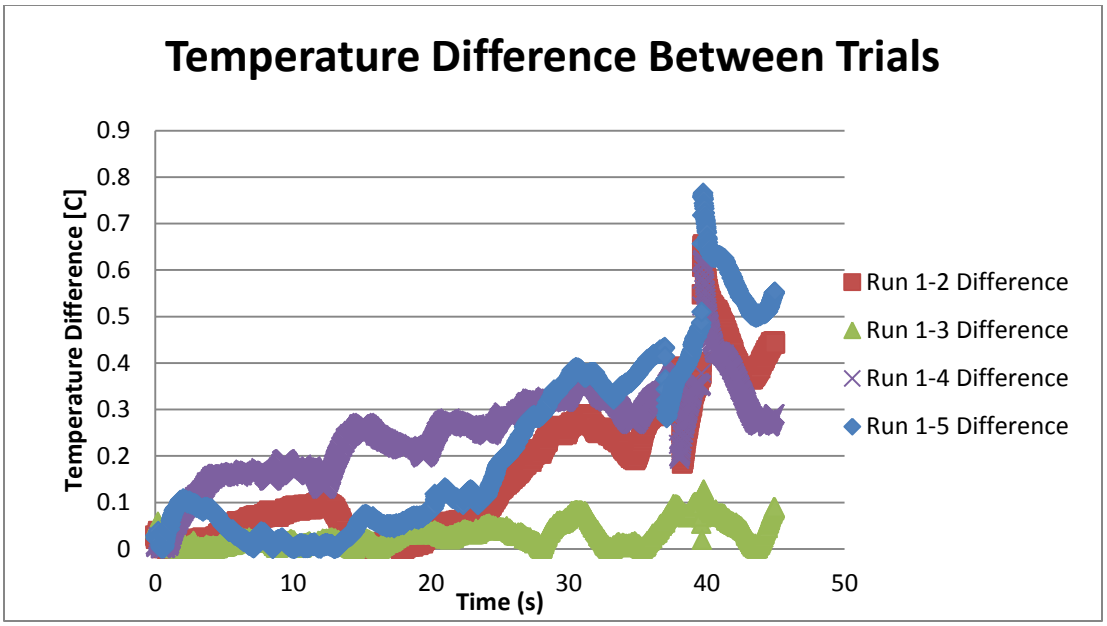

Figure 28. Temperature Difference of Dry Run Trials

Micro-DTA Heat Capacity Calibration using water samples.

Calibration of the Micro-DTA was performed using Eq. 14 above using DI water samples deposited via micro-pipettes. Ten different water samples were deposited into the Micro-DTA and then cooled at a 1 K/s cooling profile with a 60 Hz sampling rate. Each sample's volume was measured at approximately -20 °C (denoted by the relay switching the thermoelectric module into cooling mode in the video) as shown in Fig. 29. At -20 °C it was theorized that minimal evaporation will occur thereafter. The cooling curves obtained from each sample were then analyzed using a 5th order Taylor series expansion to determine the cooling rates needed for determining the micro-DTA's calibration constant. The largest water volume sample of the ten trials was used as the standard large volume sample to determine the calibration constant.

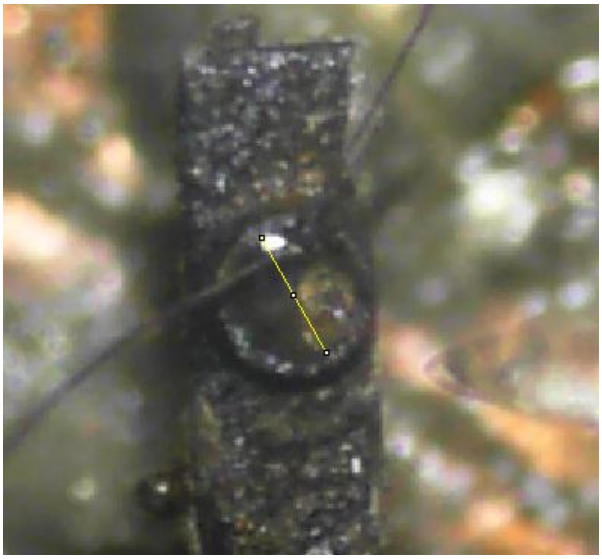

Figure 29. Water Sample Volume Abstraction

The average micro-DTA's heat capacity calibration constant was determined to be 0.0416 J/K with an associated +/- 0.00662 J/K uncertainty at 95% confidence interval. One trial was erroneous and discarded while the other trials are displayed in Table 7 and Fig 30 displaying the trials' cooling rates, sample volumes, and associated calibration constants. Trials 2 and 5 have resulted in elevated deviated results; this could be a consequence of mineral oil from the cell tram mixing with the DI water. A binary mixture of mineral oil and DI water was sometimes deposited into the micro-DTA's sample pan resulting in erroneous results. The specific heat and density of oil is 60% and 20% lower than that of water thus having an impact on results. To prevent the mixture of solutions an air based cell tram mechanism needs to be implemented into the deposition system.

Table 7. Micro-DTA Heat Capacity Calibration Results

Sample	1	2	3	4	5	6	7	8
Small Sample Cooling Rate (K/s)	0.943	0.925	0.942	0.934	0.920	0.942	0.938	0.937
Large Sample Cooling Rate (K/s)	0.898	0.898	0.897	0.900	0.888	0.899	0.899	0.899
Small Sample Volume (mm^3)	0.000823	0.000805	0.000940	0.001026	0.000824	0.000805	0.000834	0.001026
Large Sample Volume (mm^3)	0.001710	0.001710	0.001710	0.001710	0.001710	0.001710	0.001710	0.001710
Calibration Constant (J/K)	0.0341	0.0568	0.0341	0.0452	0.0479	0.0358	0.0393	0.0400
Calibration Constant Uncertainity +/- (J/K)	4.10E-05	1.15E-04	3.54E-05	5.51E-05	8.09E-05	4.59E-05	5.35E-05	4.33E-05

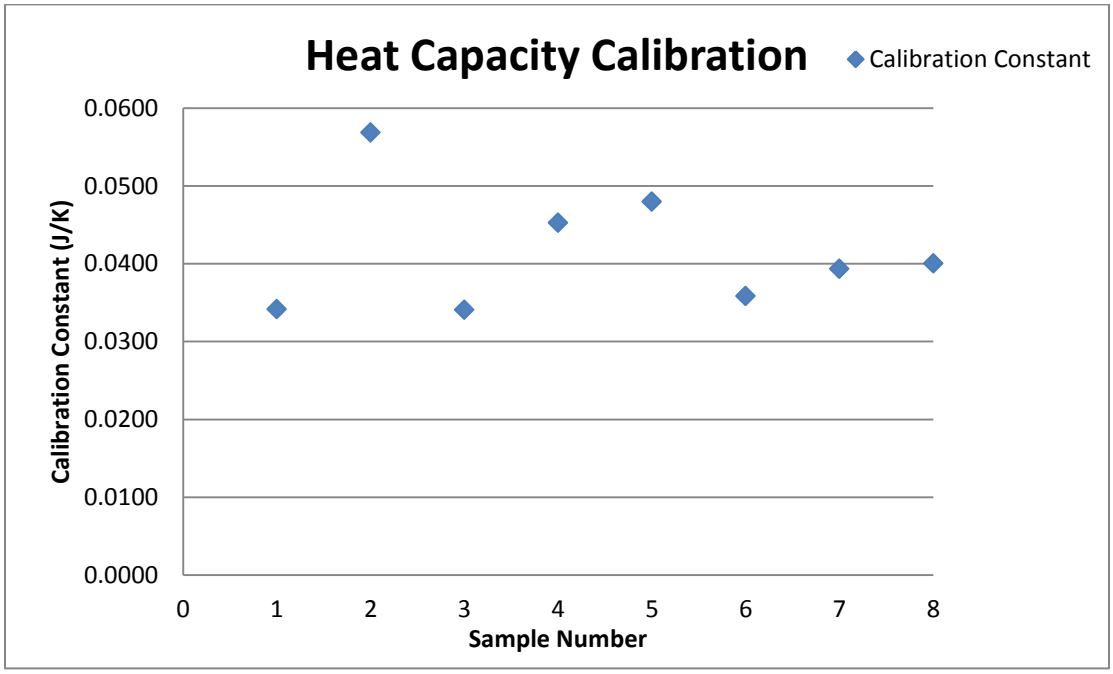

Figure 30. DTA Heat Capacity Calibration Constant Vs. Trial Number

Micro-DTA Heat of Fusion Calibration using water samples.

The last portion of displaying the proof-of-concept micro-DTA's capabilities is determining the freezing temperatures and exothermic heat releases from the water samples used from the previous heat capacity calibration series. The exothermic heat release was calculated using Eq. 5 above where the area was determined using an

adaptive Simpson's quadrature a numeric integration method. The freezing temperatures froze on average at 249 K with a deviation of +/- 0.4 K which is within the uncertainty range of the thermocouple used as shown in Table 8 and Fig 31. The heat releases of the different samples however, are highly variable from one another. The average heat of fusion for the samples is 618.8 J/Kg with an uncertainty of +/-227.8 J/Kg. The calculated heat of fusion is also off by a factor of 5 from literature values of 334 KJ/Kg.

The exothermic area under the curve and mass are the only two variables on determining the heat of fusion values that are not constant. The mass has an uncertainty percentage of 28 % relative to its mean whereas the area's relative uncertainty percentage is 87%. Therefore, the exothermic area's variability has a greater impact on the variability of the calculated heat of fusion. It his hypothesized that by having a binary mixture of mineral oil and DI water being deposited into the sample pan that the true amount of water is not known and is highly variable. Since oil is hydrophobic, the oil did not dissolve into the water altering the water's freezing point hence observing a constant freezing temperature. The exothermic peaks observed were of the water only and not of the mixture since mineral oil's freezing temperature is 20 K lower than water. The exothermic curves observed are much smaller and variable than predicted due to the unknown water volume within the crucible. The water volume uncertainty hypothesis correlates well with the known results.

Table 8. Freezing Temperatures and Heat of Fusions for water sample

Sample	1	2	3	4	5	6	7	8
Temperature Freeze (K)	248.58	249.22	250.02	248.55	248.8	249.07	249.01	248.71
Mass (Kg)	8.22E-10	8.04E-10	9.39E-10	1.28E-09	9.39E-10	8.24E-10	8.33E-10	9.39E-10
A (K-s)	0.89725	1.3396	1.5312	2.02	0.9289	0.5749	0.191	1.3528
k (W/m-K)	0.563	0.563	0.563	0.563	0.563	0.563	0.563	0.563
q (J/Kg)	579.6025	884.8294	865.7582	837.563	525.2108	370.8088	121.8252	764.8888

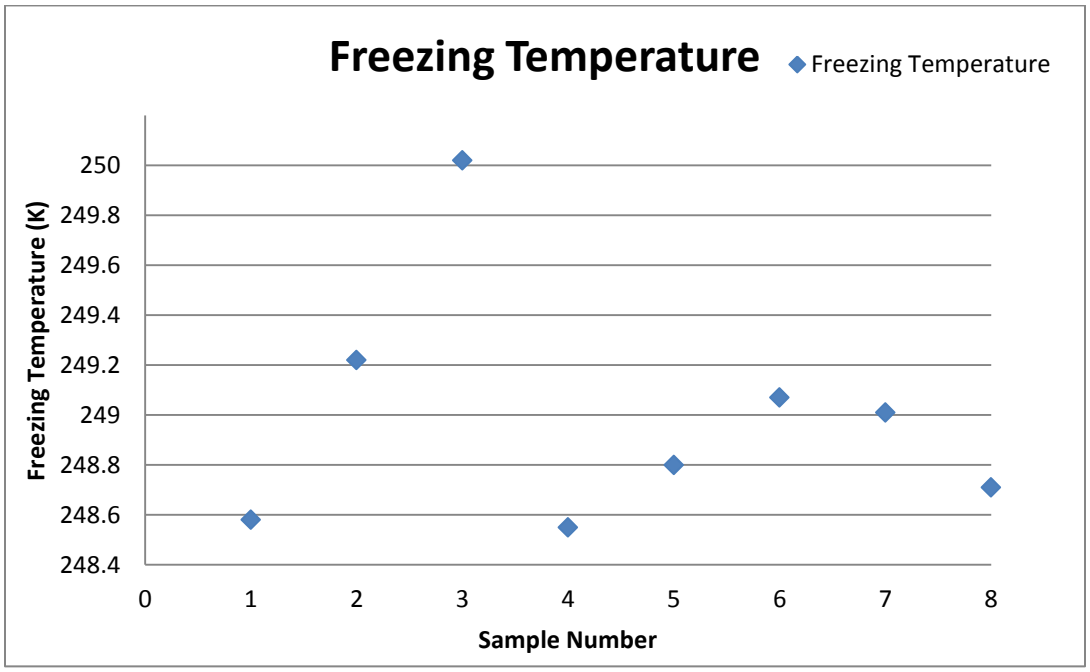

Figure 31. Freezing Temperature vs Sample Number

Micro-DTA Results Conclusion

The micro-DTA has proved to be effective in obtaining duplicate dry cooling curves, determining repeatable freezing temperatures, and calculating a relatively repeatable calibration constant despite the unknown binary mixture of oil and water. Obtaining the latent heat release values of water is hypothesized to be repeatable and accurate once a method to deposit a known volume amount of samples has been established. Utilizing an air cell tram to transport and deposit samples into the micro-crucible is a viable yet expensive approach. An alternate approach on deposition of water

samples into the crucible is to allow water condensation to selectively collect and fill inside the crucible. The theory is to coat the bridge except the crucible with Rain-X to give a hydrophobic surface, and then cool the bridge to a prescribed temperature to allow condensation of water within the micro-crucible only. This method would guarantee the delivery of pure water within the crucible, given condensation will not occur elsewhere on the micro-bridge.

Future work for micro-scanning calorimetry will include implementing a micro-DSC approach, improving the bowl shaped crucibles, and determining an alternative method of obtaining mass measurements. The micro-DTA was a stepping stone into calorimetry, the true objective is to use a DSC approach using bismuth telluride pieces as the micro-bridge's legs to control the temperature for a more accurate heat release measurement system. The bowl shaped crucibles can be optimized and redesigned for more accurate volume abstraction via imagery and to include a resistance temperature device. However, often it was difficult to determine the true diameter of the sample within the crucible. An alternate method to measure mass could lead to more accurate results such as observing the bridges natural frequency as mentioned earlier in the mass measurement section. Overall, the current device manufactured and tested has proven that the micro-DTA proof-of-concept idea is a viable sensor for measuring accurate and repeatable thermodynamic responses from nano-liter sized samples.

Chapter 5. Introduction of M.E.M.S. Manufacturing

Review

In the past 20-30 years technology has allowed scientists and engineers to effectively fabricate structures on the micro-scale level. Traditionally, micro-fabrication

has been primarily used in the electronics and computer industry; now the field has expanded further into areas such as optics, fluids, and biology. Many fields like the medical field have been significantly impacted by micro-fabrication technologies by allowing micro devices to be non-invasively implanted in patients. The micro devices are used to monitor blood pressure, deliver drugs, and even perform retinal restoration (Microelectronmechanical Systems: Advanced Materials and Fabrication Methods 1997).

The advantage of scaling down mechanical or electrical devices to the micro-scale level is to increase the device's sensitivity to allow devices to observe processes on the micro-scale level. Micro-devices or more commonly known as MicroElectroMechanical systems (MEMS) has permitted scientists to study individual biological samples than just averaging the population, allowing researchers to better understand the fundamental elements and functions of biological systems. The overall objective of this thesis is to explore the feasibility of observing thermodynamic responses from individual biological samples using MEMS fabrication techniques to develop a micro-bridge structure to perform differential thermal analysis (DTA).

M.E.M.S. manufacturing has essentially borrowed manufacturing technologies from the silicon industry to scale down macroscopic devices to the microscale level. There are three different M.E.M.S. fabrication processes that are extensively used; bulk micromachining, surface micromachining, and molding processes. Bulk micromachining is the process of selectively removing material either by use of chemical or physical means, typically a chemical treatment is used to isotropically, or anisotropically remove material of a bulk material. Surface micromachining also uses etching process like bulk micromachining; however the main theme of surface micromachining is to remove

“sacrificial” material after the deposition of the permanent material upon it to create voids within the final structure. Molding processes or more commonly known as LIGA is the process of using a photo-sensitive chemical to create sacrificial micro molds that are to be filled with a defined material [(What is MEMS n.d.)] (Judy 2001) . The three processes previously discussed are the essential fabrication processes used to fabricate the DTA bridge and will be discussed in further detail within this paper.

MicroElectricalMechanical systems (M.E.M.S.)

Although micromachining plays a role in the manufacturing process of the MEMS DTA device, LIGA processing is the primary fabrication technique used in the development of the current device. LIGA is a German acronym for the series of processing steps: lithography, electroplating, and replication. (Kelly and Goods 2005). Lithography was developed in the 1980’s by Ehrfeld and coworkers to produce structures using electroplated metallic materials with small dimensions and high aspect ratios (Faulkner 2005), (Lobontiu and Garcia 2005). Ehrfeld was the first to combine the molding process with electroplating through electro-deposition. One of the first structures produced by LIGA processes was a non-electronic device; the researchers at the Forschungzentrum Karlsruhe (FZK) developed a nozzle type device for isotopic separation of uranium which required very narrow and tall channels (Kelly and Goods 2005). Once the researchers at FZK realized LIGAs potential more effort was directed towards creating metal molds on the micron scale for plastic injection molding for mass production of micro-parts. Since then researchers around the world saw the usefulness of LIGA and developed technologies to further optimize the process.

Most structures that are developed through LIGA processing are typically mechanical in nature as a consequence of LIGA's ability to create very unique geometries. The mechanical structures can be produced in high quantity with high fidelity features due to the lithographic process and as the patterns of the structures are easily repeatable. Complicated geometries such as electrical motors and rotors can be manufactured on the micro-scale are a consequence of using LIGA (Judy 2001). One of the key advantages of LIGA is that it is an additive process that allows different varieties of metals to be grown within one structure if desired as opposed to micromachining where it is a subtractive process of usually one material (Kelly and Goods 2005). This is advantageous as with varying materials can result in different electrical and magnetic properties such as the Seeback effect seen from exposing a temperature gradient to the junction of two dissimilar conducting metals.

Micro-Bridge Fabrication Design

The design of the calorimeter device is a bridge like structure to allow optimal heat transfer from the bridge to the biological sample while isolating the sample from the ambient and allowing ease in micro-fabrication. The top portion of the bridge structure will be composed of pure copper with a small crucible container to encapsulate the cell that will be located at the center of the bridge structure. Originally, the design for the location of the crucible was to be extruded below the bridge as shown in Fig 32 (left); now the crucible is to be extruded above or be built upon the bridge as shown in Fig 32 (right). The reason for the change in design is for both fabrication simplification and heat exchanger efficiency purposes.

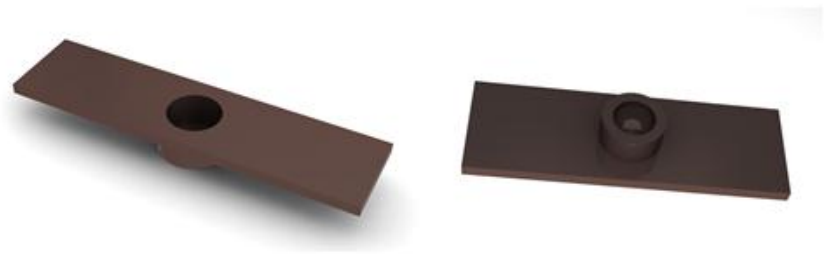

Figure 32. Design of DTA/DSC bridge with location of crucible being below the bridge (left) or extruded above (right)

Growing the crucible structure above the bridge allows flexibility in alignment or position on the bridge as opposed to having the crucible below the bridge. The alignment of the latter structure had to be very precise in order to be concentrically aligned with the preceding opening of the crucible and the hole in the bridge as shown in Fig 33. Normally, alignment should not be an issue with precision alignment mechanisms available but the lower budget equipment that is being utilized is aligned by hand. Also, with the crucible being below the bridge one extra fabrication step will need to be implemented in order to create the bottom of the crucible container as opposed to the crucible being located on top where the bridge platform serves as the bottom. Another advantage of having the crucible being located on top of the bridge is harnessing a more efficient heat transfer process because the surface area between the bridge and crucible is larger. The thermal conductive surface area from the bridge to the crucible positioned on top is of a full cylinder as opposed to just a partial cylinder from the crucible located below the bridge. The position of the crucible being extruded above the bridge is the most ideal in terms of fabrication and heat transfer.

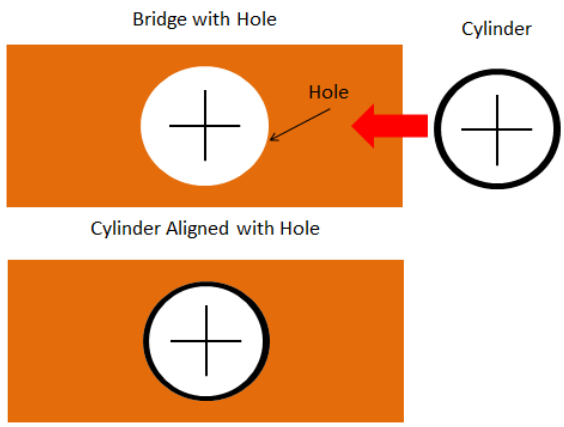

Figure 33. Difficulty in Concentric Alignment with Crucible Located Below Bridge

The legs of the bridge structure are 500X250X250 µm bismuth telluride pieces which isolate the bridge structure and sample while also allowing for better cooling control of the sample. The bismuth telluride pieces raise the bridge and sample from the bulk cooling surface allowing access for fiberglass strands to be placed in the voids to help isolate the bridge from the cooling surface. This isolation effectively decreases the overall heat capacity of the measurement system or smaller thermal lag times. The main reason bismuth telluride was chosen to be the bridge legs' material because they are an efficient thermoelectric material for refrigeration. The thermoelectric circuit is comprised of two electrically dissimilar materials and when a current is passed from one material to the other i.e. copper bridge to the bismuth telluride heat is either absorbed or liberated depending on the direction of the electrical current. This allows for a more precise temperature control system for cooling of the biological sample for differential scanning calorimetry purposes.

L.I.G.A. Introduction

General Overview

LIGA requires a general flow of steps in order to fabricate micro-parts. The process consists of applying a photo-active chemical or photoresist upon a sacrificial electrically conductive surface. A UV light along with a UV absorbing mask is used to imprint patterns from the mask onto the photo-active resist. The exposed (positive image) or unexposed (negative image) is then removed creating mold cavities and exposing the conductive surface. The mold cavities are then filled with a desired material through electro-deposition where cations or positively charged ions flow from the depositing material and adhere to the exposed electrically conductive anode.

After electro-deposition the mold cavities are removed through chemical means exposing the grown material. The final product is completed usually through multiple steps of the sequence just described by adding different layers of materials or geometries to the base layer and then separated from the sacrificial conductive material through a chemical etching process (Microelectromechanical Systems 1997), (Allen 2005), (Maluf and Williams 2004), (Lobontiu and Garcia 2005), (Kelly and Goods 2005). The entire LIGA process that was described above is shown below in Fig. 34.

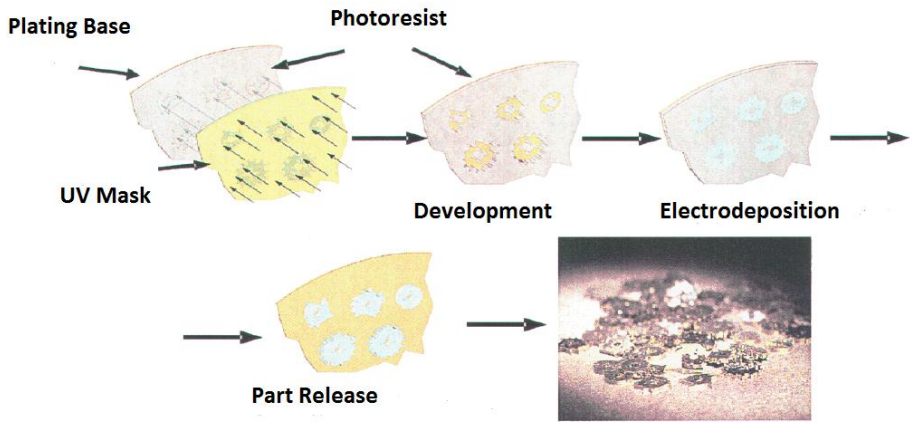

Figure 34. LIGA process flows (Kelly and Goods 2005).

Substrate as the Platform

As mentioned before LIGA is based on growing structures upon previously established mechanical platforms, a substrate must be chosen in order to support the entire process of LIGA. The base platform or substrate can be any substance with a virtually flawless surface and careful consideration must be taken when selecting the material. Since most of MEMS manufacturing has adopted techniques used in the electronics industry, the use of silicon based products as the substrate is no exception. The silicon wafers are grown in cylinders ranging from 6 to 12 inches in diameter and cut in thin slices ranging from 625 and 725 µm then completed by polishing to a fine surface finish. Silicon wafers are widely accepted and are the standard substrates in MEMS manufacturing because of the well-established manufacturing process making them available at high quality and quantity at lost cost. (Allen 2005).

Surface Cleaning

As the fabrication environment scales down to the microscale level, effects from surface contamination becomes an important consideration during the MEMS

manufacturing processes. Surface contaminates are a potential threat to the integrity of a microscale product because the size of the potential contaminates are now large enough relative to the device being produced to change the overall composition of the part being created. Also, contamination affects adhesion to surfaces, which is detrimental to successful photoresist application and electroplating processes.

Contaminates that are often encountered in MEMS processing are typically soils or molecular compounds and oxides. Soils are mostly particles or films of lubricants, greases, solvent residues, metal oxides or hydroxides. Extreme caution needs to be implemented when handling the substrates as to not containment the wafers. The usage of gloves, petri dishes, and vacuum bags are common items used in a clean room to keep the wafer surfaces as clean as possible. Oxides are typically grown native on the surface of the wafers after a certain period of time and accelerated by increased temperature. The most common oxide encountered is silicon dioxide (SiO_2) which inhibits adhesion of most deposition processes. (Kern 1990), (Franssila 2004)

Cleaning processes have been developed since the 1960s and implemented as standard operating procedures in the wafer cleaning processing laboratories such as the RCA cleaning practices. RCA (Radio Cooperation of America) has created a standard for cleaning silicon wafers for the electronics industries, which include removal of the organic containments, removal of oxide layers, and removal of ionic contamination. It is important for RCA processes to be implemented in the order as described earlier or proper surface cleaning will not be achieved. The organic containments can serve as a mask to prevent the oxide etching solutions from ever reaching the oxide layer for proper removal of the oxide layer and then subsequently ionic contamination removal. Chemical

removal is favored over mechanical means due to simplicity and less probability of surface re-contamination. (Kern 1990)

The cleaning procedures vary from each laboratory and are dependent upon the preceding and following process MEMS processing steps but the chemicals used for each step are standard throughout all. Peroxide solutions such as ammonia peroxide (NH_4OH:H_2O_2:H_2O,1:1:5), hydrogen chloride-peroxide (HCl:H2O2:H2O, (1:1:6), and sulphuric peroxide mixture (H_2SO_4:H_2O_2, 4:1) are heavily used to remove the organic or soil layers from the surfaces. The peroxide chemicals are very efficient in the removal of most types of soils without damaging the silicon wafer itself. Hydrogen fluoride (HF) is commonly used to remove the native oxide layer without attacking the silicon surface itself. HF is typically diluted with DI water in order to slow down the etch rate of SiO_2, thereby ensuring better etch uniformity. Typical dilution ratios range from 1:1 H_2O:HF to 100:1 H_2O:HF. Acidic pickling solutions are also used to remove oxide layers, but typically oxide layers upon metal surfaces before electroplating. The pickling also slightly attacks the surface to be plated leaving the surface slightly rough for improved electroplating adhesion. (Standard Practice for Preparation of Copper and Copper-Base Alloys for electroplating and conversion coatings 2008), (Franssila 2004), (Kern 1990)

Wafer rinsing and drying procedures are just as important as the cleaning procedures because surfaces become recontaminated easily if not processed correctly. The chemically cleaned wafers are usually rinsed with highly filter deionized water to effectively remove all chemicals from the surface. Often, the wafers are placed in ultrasonic agitated DI water baths for improved results. Drying of the wafers must be done by physical means and not by evaporation. Spin drying and the use of nitrogen gas

are commonly used to effectively remove the water from the surface while preventing particles or debris from collecting. Often the wafers are rinsed in 80 °C DI water to allow capillary action to remove the water from the surface once the wafer was removed. Isopropyl alcohol is also used to achieve a clean particle free drying process by displacing the water. (Kern 1990), (Franssila 2004).

Base Layer Deposition

LIGA requires an electrically conducting cathode layer for the depositing metal to be plated to during electrodeposition; a couple different techniques are employed that deposit conducting metal layers upon the surface of a silicon wafer such as sputtering and evaporation. The processes use either physical means of excitation energies to break the bonds of the bulk depositing material to release the material's atoms in the controlled environment; the atoms will adhere with the surrounding surfaces to build atom by atom layers. Both Evaporation and sputtering are physical processes that do not require chemical reactions for deposition of thin films upon a substrate unlike chemical vapor deposition (CVD). The deposition processes described above are able to repeatedly and precisely deposit ultrathin layers (nm) of the desired material upon the selected mechanical platform (Allen 2005), (Maluf and Williams 2004).

Sputtering is a deposition process that uses high energy ions created from low-voltage induced plasma within a low pressure inert atmosphere to strip off the target (cathode) or depositing material's atoms; the atoms will then collide into the desired mechanical platform (wafer) to deposit thin films. Sputtering is an ideal deposition process within the MEMS community because the process is usually performed in a relatively low temperature environment (<150 C°) to deposit thin films of materials such

as aluminum, titanium, chromium, platinum, tungsten, and palladium. The ions that collide with the target should ideally have a high atomic weight to ensure successful ejection of the surface atoms. Using Argon as the inert gas is often used in the sputtering processes because of its high atomic weight (Allen 2005), (Maluf and Williams 2004).

Sputtering processes create an environment of highly energized particles compared to evaporation methods; this is advantageous because the collided particles have great surface mobility, which leads to greater thin film uniformity over a step or step coverage. The directionality of the ejected target's atoms is random which can lead to poor step coverage if the target is smaller than the wafer. The films are usually under variable amounts of tensile or compressive stresses and are usually reduced by heating of the substrate, although heating is not necessary for adhesion purposes. Typically, inert materials such as gold, silver, and nickel are very difficult to sputter upon silicon based wafers because of the natural oxide layer that grows upon the surface of the substrate causing the inert material to peel off during handling. A solution is to sputter a thin adhesion layer (5-20nm) that reacts well with the oxide layers such as titanium as it also grows a natural oxide layer. After the adhesion layer is established the desired electrically conductive material can then be sputtered upon the adhesion layer to complete the sputtering process. An important consideration when sputtering the desired layer upon the adhesion layer is that the adhesion layer must not be exposed to oxygen or the process will fail (Allen 2005), (Maluf and Williams 2004).

Evaporation deposition involves heating the desired material to be deposited upon the desired mechanical platform to the point of evaporation where the material will then condense upon the substrate in thin layers. The processes should always be performed in

a vacuum chamber to decrease the vapor temperature and to prevent atmospheric contamination of the deposited material. The target material is typically heated using electrically resistive heaters. However, for target materials with evaporation temperatures that approaches the melting temperature of the heaters the material selection of the electrical heaters must be carefully considered to prevent contamination. Other heating methods are often used for improved quality of deposition such electron beam heating but careful a more complex chamber must be designed to accompany radiation shielding and water cooling. Unlike sputtering evaporation, deposition is very directionally dependent meaning in order to achieve a good step coverage the wafer must be rotated around the depositing material.

Photoresist

Photoresist is the major component into developing the mold for electro-deposition and the thickness of the resist and type of resist should always be considered before developing a fabrication procedure. Many resists that have been developed for the silicon industry hardly ever exceed 10 microns, a special type of resist called thick photoresist has been developed specifically for LIGA fabrication processes which can range from 10 microns to a few millimeters. Many new thick resists have been developed for such purposes such as SU-8, a thick resist that is used frequently in research that can easily exceed one hundred microns and have excellent aspect ratios (up to 1:50) which is ideal for LIGA (Yang and Wang 2004). Typically, with thick resists special attention to exposure recipes and mask design have to be implemented in order to obtain desired results (W. W. Flack, H.-A. Nguyen, et al. 2005). As a rule of thumb the thickness of the resist should be around 25% taller than the desired geometry to prevent the material from outgrowing the mold, which would cause undesirable outcomes (Kelly and Goods 2005).

Photoresist chemicals are organic compounds that consist of three different compounds that lead to the unique characteristic abilities as a photosensitive sacrificial mold. The first compound called the resin affects the overall toughness and resolution of the material during handling and electrodeposition. The second substance is the photoactive compound that determines the amount of UV exposure or sensitivity $\frac{mJ}{cm^2}$ of the photoresist to alter the chemical composition of the photoresist. The last component of the photoresist is the solvent, which affects the overall viscosity of the photoresist that affects the uniformity and thickness of the resist. The resist is applied to the wafer usually by means of centrifugal force to spread the photoresist evenly over the substrate. For ultra-thick photoresists such as SU-8 the solvent is typically very viscous to produce thick layers. The solvent is evaporated away by using prescribed baking procedures to make the structure strong and rigid; these procedures will be covered thoroughly in later chapters.

Two different types of photo resists that are available are negative and positive photoresists meaning either positive or negative images will be imprinted from the UV absorbing mask onto the resist after development. When developing positive type photoresists the photoresist that has been exposed by the UV light alters its chemical composition and becomes more soluble when exposed to a developer solution, the image remaining is the exact image as projected from the mask. However, the negative resist reacts completely different when exposed to the UV light. The exposed resist polymerizes and becomes more difficult to remove by a developer solution than the unexposed resist leaving a negative image behind. Figure 35 effectively describes the differences between the positive and negative resists. Traditionally, the negative

photoresist is much harder to remove than the positive photoresist but it can also withstand higher temperatures (Flack, Nguyen and Capsuto, Characterization of an Ultra-Thick Positive Photoresist for Electroplating Applications 2003). When choosing the photoresist type it is important to always guarantee that the photoresist will not react with the main chemical in the electrolyte solution during electrodeposition or catastrophic results may occur during plating.

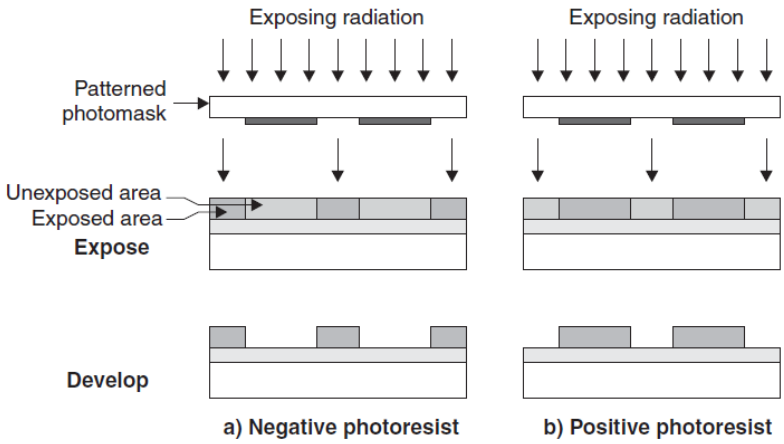

Figure 35. Positive and Negative Resist Differences (Jones 2000)

Photoresist Coating

A few methods are used to uniformly apply photoresist to the surface of the substrate but spin on methods have been proven as a fast, effective, and repeatable technique to coat the surface of a wafer. The spin on method essentially spins the wafer with a specific amount of photoresist deposited to speeds up to 3000 rpm; the centripetal acceleration causes the photoresist to spread around and eventually off of the wafer creating an even coating. The equipment is simple, a spin table with variable speed settings, a dispense nozzle, and a protective shield to protect the surroundings from excessive photoresist being thrown from the spinning wafer. The spin on method is an

established process in the MEMS fabrication community to coat substrates with organic resists (Maluf and Williams 2004) (Columbia University Clean Room 2009).

The spin on process can be broken down to four categories: deposition, spin up, spin off, and evaporation. As mentioned before a precise amount of photoresist is deposited upon the wafer before the wafer is spun up to final speed, the deposition can either be static or dynamic. During static deposition a puddle is formed in the center of the wafer ranging in volume from 1 to 10cc. While during dynamic deposition the wafer is spinning at a lower rpm typically at 500 rpm to help spreading the photoresist evenly across the wafer resulting in less waste. When utilizing either method it is important to apply an excessive amount of resist to ensure no discontinues exist during the final spin sequence due to fluid front drying before reaching the edge (Columbia University Clean Room 2009), (Bornside, Macosko and Scriven 1987).

During the spin up sequence the fluid is moved to the outer edge of the substrate by centrifugal forces, a fluid wave front forms and moves to the edge leaving a uniform surface behind. Once the wave front reaches the edge, surface tension prevents the photoresist from leaving the wafer until the centrifugal forces exceed the surface tension causing the resist to be spun off causing thinning of the photoresist. Throughout the spinning process the viscosity of the resist increases due to evaporation of the solvent. The final thickness of the photoresist is an equilibrium balance between the shear forces in the resist due to viscosity and the centrifugal forces due to spinning. The thickness is inversely proportional to the rotational speed w of the wafer and the viscosity v_o of the resist as shown in Eq. 31 where a and y are dimensionless parameters. The process of steps involved in the spin-on method is described below in Fig. 36 (Jones 2000).

$$h = \frac{y\sqrt{a}{v_o}^{1/4}}{\sqrt{w}} \tag{31}$$

Thinning of the resist is also caused by evaporation of the solvent throughout both the spin up and spin off series. The resin within the photoresist is absorbed into the atmosphere and can have significant effects on the uniformity of the deposited resist. If excessive resin evaporates early on in the spin process a solid layer of resist forms on the surface impeding normal evaporation of the resist that is trapped beneath causing deformities within the coating (Columbia University Clean Room 2009), (Bornside, Macosko and Scriven 1987).

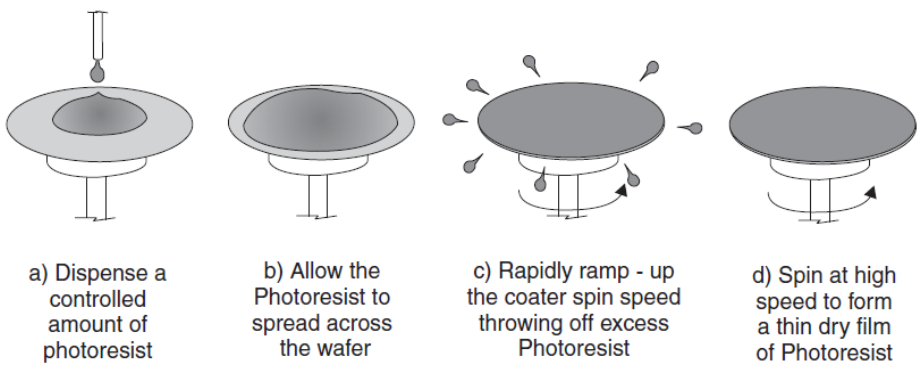

Figure 36. Process of spin coating (Jones 2000)

Acceleration from startup to the final setup can also serve as another parameter of the final overall thickness and uniformity of the photoresist. The first few seconds of the spinning process is crucial since 50% of the solvent will have been evaporated; hence controlling how fast the wafer reaches the prescribed limit or acceleration of the wafer should be accurately controlled. Acceleration also manipulates the resin in a twisting action allowing the resin to fully encompass topographic features that may already be on the substrate such as previously grown mechanical structures which is a common occurrence during LIGA steps. Depending on the size and complexity of the geometries

of the already established topographic features on the substrate different acceleration prescriptions should be chosen to allow for a more uniform coating (Columbia University Clean Room 2009).

A few disadvantages from using the spin on method are common occurrences and can be easily compensated for such as resist waste and edge beading. As stated before an excessive amount of resist must be initially applied in order to ensure continuous photoresist throughout the wafer, this can lead to 90-95% resist loss (Snodgrass and Newquist 1994). Photoresist waste cannot be prevented but can be reduced by using a dynamic dispense and optimize the volume of resist applied upon unit of area through trial and error studies. Overall, the waste of the spin-on method can be costly if mass production LIGA is implemented.

Edge beading is the buildup of resist on the edges that usually always exceeds the overall thickness of the photoresist throughout the wafer. Edge beading occurs due to surface tension at the edge preventing the photoresist from fully flowing off of the wafer causing a slight bump or bead at the edge. The effect is additive such that the resist then hardens and allows more resist to flow over the original bump adding to the thickness. Edge beading affects non circular wafers more dramatically as the resist tends to build up around the corners (Carcano, Ceriani and Soglio 1993). Edge beading can be detrimental during the exposure process due to the elevated edge impeding the photo absorbing mask to make perfect contact with the majority of the deposited resist causing distorted images. Techniques such as beveling the edges, spraying developing solution, and even physically removing the edges have been used to compensate for the increase in thickness around the edge (Columbia University Clean Room 2009).

There are many factors that influence the quality of the photoresist coating upon the wafer such as humidity, acceleration, speed, and surface contamination. Many times appearances of discontinuities within the coatings occur due to improper cleaning of the surface wafer inhibiting the photoresist to adhere properly to the wafer. Air bubbles often appear within the resist causing undesirable imperfections to the structure patterns after development. Air bubbles typically occur due to imperfections in the dispense nozzle or improper application of the resist during dynamic dispense.

Soft bake

Once the wafer has been successfully coated with the desired thickness of photoresist a soft baking procedure is implemented to evaporate the remaining amount of solvent causing the coating to become rigid. The time and temperature of the soft baking procedure is dependent on the resist, the solvent and thickness of the photoresist. Soft bake temperature and time recipes must be carefully controlled due to the possibility of deviations in the chemical compound of the photoresist that will cause undesired results.

If the soft bake temperature or time is too low or short, then an excessive amount of solvent will remain causing the photoactive chemical to not be fully sensitive. The result from an insufficient soft bake procedure can cause dark erosion meaning the portion of the resist that is not selected to be removed is eroded away. If the soft bake is too long or the temperature is too high then a portion of the photoactive chemical can be altered and or destroyed, decreasing development rates of the resists. Other side effects from over soft baking can lead to severe dehydrating of the photoresist which can cause cracking and chipping away.

Lithography

The next step in LIGA is lithography which as described before is the process of transferring a desired pattern from a mask throughout the thickness of the photoresist. Lithography is the most critical portion of the LIGA process as it is the most influential on the precision of the desired geometrical outcome. The equipment involved for successful results is also the most expensive because most LIGA steps involves multiple steps which require highly repeatable processes in order to fabricate the desired MEMS device. The lithography involves sequential steps to deposit the desired pattern within the resist such as the mask design, mask alignment, and exposure doses.

During lithography, images from the photo absorbing mask are projected onto the layer of photoresist; the mask layout must first be designed before the mask can be fabricated. The overall objective of the mask layout is to achieve a good mixing between the exposed and unexposed areas. Large uninterrupted areas in resist are undesirable because the thermal expansion and swelling cause distortion in the geometry of parts (Kelly and Goods 2005). To achieve high fidelity within the mold array, ancillary structures are typically placed to prevent large distortions. Also by placing ancillary structures in uninterrupted areas in the resist also improves homogeneity of the current density during electroplating that ultimately improves plating uniformity (Dukovic, Gerisher and Tobias 1994), (Yang, et al. 2006).

Mask Design

When designing the photo-absorbing mask for the lithography purposes the minimum line width resolution must be taken in consideration in order to achieve high fidelity. The resolution of the mask is closely coupled with the wavelength of the illumination source. Derived from the Raleigh criteria for optical resolution Eq. 32

represents the minimum line width W given the wave length of the light λ used and the numerical aperture NA which is usually dependent upon the device. Where the numerical aperture is a function of the refractive index n between the object and the wafer, and the half angle of the image β as shown in Eq. 33. Minimizing the wavelength of light increases the resolution of the pattern that can be transferred on the photoresist, hence the reason UV light and even in some cases extreme ultraviolet light is used (Allen 2005).

$$W = \frac{\lambda}{NA^2} \tag{32}$$

$$NA = n \sin \beta \tag{33}$$

The mask layout is typically designed in a CAD package and a few MEMS specific commercial packages are available to help in constructing the layout. If one desires, thermal-mechanical computational analysis of the resist can be evaluated to determine where there may be areas of concern for distortion. Also, an electrical field analysis can also be used to evaluate the current densities within the design of the photoresist mask layout to optimize deposition uniformity. Mask design can heavily influence the outcome of the final product during LIGA and is imperative to involve the previously stated design considerations during the mask layout process.

Alignment

LIGA often involves multiple steps in order to implement complex geometries in micro-devices therefore it is crucial to have proper alignment of the photo mask with the preceding topographical structures established on the wafer. The most common method is implementing fiducial markers in the exact location throughout the series of photo masks that will be used to create the micro-device. The fiducial markers will serve as a

point of reference as they will be transferred and grown onto the wafer like the micro-device. The subsequent features can then be precisely aligned with the preceding features by correctly matching the fiducial markers of the photo mask with the fabricated fiducals as shown below in Fig 37. There are no set design criteria for fiducial markings but the fiducials will allow for proper alignment of both the X and Y axis along with rotation of both the mask and proceeding features, generally crosses are used for such purposes.

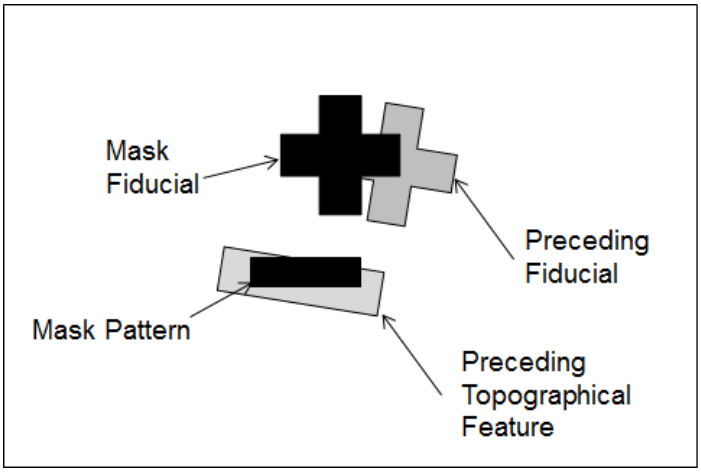

Figure 37. Alignment of patterned and mask features using fiducial markings.

In low production facilities such as laboratories contact aligners are often used due to the simplicity in the optical infrastructure. Contact aligners physically press the UV absorbing mask in perfect contact against the post-soft baked photoresist. With perfect contact between the mask and resist considerations such as UV light leaking underneath the photo absorbing mask causing undesirable results can be ignored. Imperfections such as edge beading and or bumps formed in the surface of the resist will obstruct the mask from coming in perfect contact with the photoresist and proper techniques to alleviate these inadequacies must be implemented.

In order for the mask and the photoresist to be in precise contact with one another, perfect parallelism between the two needs to be established. Typically most contact aligners are equipped with a wafer platform floating on a stream of air, when the wafer and mask are in contact the platform will adjust to be in perfect parallel with the mask. The wafer platform will then be locked in position while the mask will be raised slightly in order to perform alignment between the mask and the preceding fiducials.

Exposure

Exposing the photoresist to UV light chemically alters the photoresist to either become resilient or vulnerable to chemical etching; to effectively achieve this process the proper exposure dose needs to be implemented. The exposure dose is dependent upon the photoresist thickness and the type of photoactive compound within the photoresist. Determining the exposure dosage is typically determining the amount of exposure time the photoresist is subject to. Typically, most exposure devices have a constant power density output $\frac{mW}{cm^2}$ and photoresists have a constant sensitivity or energy density input $\frac{mJ}{cm^2}$, therefore the amount of time in seconds the photoresist is exposed can be determined.

If the photoresist is improperly exposed deviations in the geometry will occur leading to poor results. The direction in deviations in the features depend upon if the photoresist is either negative or positive type. If the photoresist is over exposed the miniscule amount of UV light that leaks under the photo absorbing mask affects the "covered" resist enough to alter its chemical composition. Negative type resists that are over exposed will experience a decrease in feature size while positive type photoresists under the same exposure will show an increase in geometry size. If the photoresist is

under exposed then the photoactive chemical within the resist is not fully activated. Positive resists under exposed will then obviously exhibit smaller geometries while negative resists will show larger features.

Post Exposure Bake

Many times it is desirable to raise the temperature of the photoresist just above the resist's softening point after exposure called post exposure bake to crosslink the monomers in negative resists, smoothing the feature walls and mechanical relaxation. During exposure of many but not all negative type resists, photons react with the photoactive chemical to create monomer links and a post exposure bake is required to crosslink the monomers into developer resistive polymers. If reflective wafer surfaces are used during exposure then a rippling effect along the geometry caused by standing waves can result in a lower resolution of the feature. A solution to the rippling effect is applying a post exposure bake to effectively agitate the photoresist molecules and cause a smoothing out effect. After soft baking and exposure of the photoresist mechanical stress can occur due to expanding nitrogen within the compound especially within thick photoresists. An effective post exposure bake can relax these mechanical stresses while improving adhesion and reducing under etching (Jones 2000), (Baking Steps in Photoresists Processing 2010).

Development

The last step to create micro-mold cavities within the resist is termed as development, where a chemical etchant attacks the unexposed (negative type) or exposed (positive type) portion of the photoresist. The etchant carves out the weak portions of the photoresist leaving the desired topographical mold structures intact for electrodeposition. The time of full development of the cavities is dependent upon the type and thickness of

the photoresist used, while continuously and properly agitated. If the photoresist is over developed dark erosion is likely to occur, which causes feature distortion. Dark erosion distortion caused from over development is especially noticed in thick resists where the feature's walls exhibit a slant like topography due to linear dark erosion throughout the thickness from the more eroded surface to the less eroded bottom. Proper development is a balance between maximizing the removal of the unwanted resist while minimizing the erosion of the wanted resist, thus procedures and results should be accurately documented.

Electroplating

Growing of microstructures within the micro-mold cavities is typically performed by electroplating which is the process of transferring metal ions through an electric field from a desired metal to the surface of the target. The process is capable of growing thin metal layers ranging from 1 µm to greater than 100 µm. The process delivers direct current through the anode or the wanted metal to oxidize the material into cations (positive charge) by losing electrons within a solution. The cations associate to the anions in the solution or electrolyte bath and then reduce back to the original desired material at the surface at the cathode to effectively transfer material to the target. Many factors affect the quality of plating the material such as the electrolyte solution, temperature, agitation, and current density (Kanani 2004), (Madou 2002).

Electrolyte Solution

The electrolyte solution is composed of metal salts, which dissociate to allow the transfer of ions from within the solution. The electrolyte solutions can be broken down into three different categories depending upon the pH levels such as acidic, neutral, and alkaline solutions. Acidic electrolyte baths are typically used in producing MEMs

because finer grain deposition can be achieved which improves fidelity and the quality of the microstructure being created. Acidic baths are based on salts such as sulfates or chlorides to dissociate into their associative cations and anions, and the acid is used to optimize the electrical conductivity. Additives called brighteners such as chloride and polyethylene glycol (PEG) can enhance the surface quality of the deposition by aiding in a smooth deposition with minimal surface roughness (Li, Ye and Li 2001), (Kanani 2004).

Current Density

Current density plays a large role in not only the deposition rate of material being plated but also the quality such as porosity, surface roughness, and strength. Higher current densities may expedite plating thickness but also will lead to poor uniformity and high surface roughness. Macro-throwing power is a metric used to determine how well the electrolyte solution is able to lay down a uniform layer of metallic crystals across the cathode target. Throwing power is dependent upon the primary and secondary current densities of the system (Madou 2002).

As previously stated, careful consideration during mask design must be taken to promote evenly distributed primary current densities. Primary Current densities are higher at sharp corners or where the dimensional area is smaller with respect to other geometries within the micro- mold layout. As shown in Fig 38. electric field lines are more concentrated at edges (Section A) whereas the current densities are more uniform in flat interrupted regions (Section B); perfectly distributed electric field lines (Section C) are never seen in practice. Unbalanced current densities due to uneven geometry sizes cause irregular plating throughout the micro-mold cavities. Experimentally, throwing

power can be determined by the use of Hull or a Haring-Blum Cell (Madou 2002) (Kanani 2004).

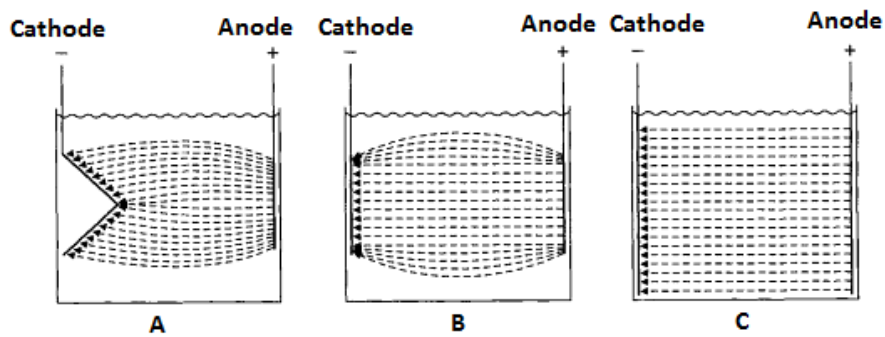

Figure 38. Primary Current Densities Between Anode and Cathode as a Function of Cathode Dimension (Kanani 2004)

The Secondary current densities are attributed to the electrochemical interactions at the cathode, which are dependent upon the solution, agitation and temperature. In order for reactions to occur from the cathode to the anode surfaces, species must be transported efficiently. Through electrochemical reactions at the surfaces of the anode and cathode, the concentration of the species will vary though out the boundary layer thickness at the surfaces of the electrodes. This gradient in concentration $\frac{dc}{dx}$ can be described by Eq. 34 where ${C^0}_{x=\infty}$ is the concentration in the bulk electrolyte and $C_{x=0}$ is the concentration of the species at the electrode surface, and δ represents the boundary layer thickness.

$$\frac{dc}{dx} = \frac{{C^0}_{x=\infty} - C_{x=0}}{\delta} \tag{34}$$

Equation 34. can be rewritten in terms of current density J based on Faraday's law in Eq. 35. where n is the number of electrons transferred, F is Faraday's constant and D is the

diffusion coefficient. At a certain potential all of the species are consumed and the concentration at the surface i.e. $C_{x=0}$ go to zero thus leading to the limiting current density J_I as shown in Eq. 36. which illustrates that the limiting current is a function of the bulk concentration of the reacting species (Lee, Strathmann and Moon, Determination of the limiting current density in electrodialysis desalination as a emperical function of linear velocity 2005).

The ratio of the species concentration at the surface with respect to the species concentration of the bulk can be related to the ratio of the limiting current density and current density. Equation 35 can be re-written so that the current density will be expressed in measurable quantities, this relation is shown below in Eq. 37 where η is concentration polarization, and R and T are the ideal gas constant and absolute temperature (Kanani 2004). It has shown that by increasing the stir speed or agitation of the electrolyte bath increases the limiting current because the promotion of convective transport results in a smaller boundary layer (Kanani 2004), (Lee, Strathmann and Moon, Determination of the limiting current density in electrodialysis desalination as a emperical function of linear velocity 2005).

$$J = nFD\,\frac{{C^0}_{x=\infty} - C_{x=0}}{\delta} \tag{35}$$

$$J_I = nFD\,\frac{{C^0}_{x=\infty}}{\delta} \tag{36}$$

$$J = J_I\left(1 - e^{\frac{nF\eta}{RT}}\right) \tag{37}$$

Pulsed Plating

Pulsed plating or more commonly called pulsed electrodeposition (PED) is an alternate technique used to improve the quality of plating. Pulsed plating is a swift alternation of two different values of current applied between the anode and cathode. Pulse plating can either be in direct current (D.C.) where the pulses are of equal amplitude, duration, and polarity followed by zero current; or the pulses can be alternating current where the polarity alternates at each pulse. Typically in D.C. pulse plating, the pulses are in square form but other forms of pulses such as saw tooth can be achieved. Pulse plating favors initiation of grain nuclei, which promotes finer grain deposition with improved quality compared to traditional plating methods. PED is an advantageous alternative compared to adding leveling and brightening agents that can affect the electrical and mechanical properties of the deposited metal. The brightening agents contain different atomic configurations than most materials that are plated leading to high sources of mechanical stresses. (Osero 1986) (Devaraj 1990) (Zhang, et al. 2008) (Chandrasekar and Pushpavanam 2008) (Gad-el-Hak 2006).

PED improves throwing powering power by effectively improving the distribution of both the primary and secondary current densities. In traditional direct current electroplating electrical current gradients exist within the electrolyte solution, which affects the current density across the cathode. In high current gradient areas the ion concentration is lower than the low current gradient regions. During pulse off high current gradients with low ion concentrations will be replenished with ions from low current regions to effectively smooth out the ion concentration within the solution. When pulse on occurs the ion concentration will be more evenly distributed across the cathode target (Chandrasekar and Pushpavanam 2008) (Puippe 1980).

As stated earlier, in traditional direct current plating a boundary layer is formed around the cathode as the process continues. This negatively charged boundary layer grows to a defined thickness within a specified amount of time and impedes the species from reaching the surface of the cathode target. In PED the electrical current momentary ceases causing the charged boundary layer to discharge allowing ions to reach the surface more easily. The pulses in electroplating promote improved porosity within the metal being deposited. (Puippe 1980) (Chandrasekar and Pushpavanam 2008).

Traditional electrodepositon is dependent upon the current density only, whereas PED has three independent parameters, which are current, time of pulse on, and time of pulse off. An important pulsed current parameter is the corresponding duty cycle, which is a percentage of the pulse time that is on, T_{on} compared to the pulse time that is off, T_{off} and can be expressed in Eq. 38 below. The duty cycle is used to calculate the average current I_A from the peak current I_P used in the pulses as represented in Eq. 39 below. Figure 39 illustrates the pulse parameters just discussed in a graphical representation (Madou 2002) (Kanani 2004) (Zhang, et al. 2008).

$$Duty\ Cycle = \frac{T_{on}}{T_{on}+T_{off}} \tag{38}$$

$$I_A = I_P \times\ Duty\ Cycle \tag{39}$$

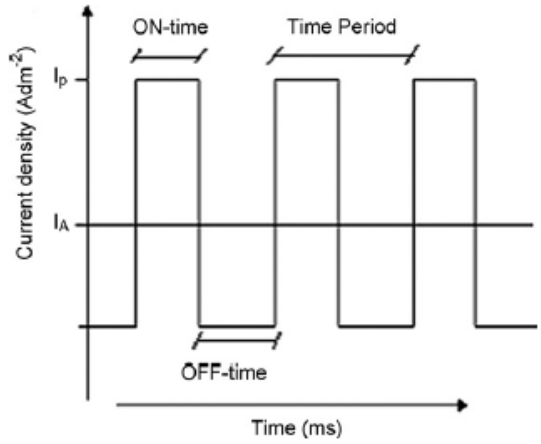

Figure 39. Pulsed Plating Waveform (Kanani 2004)

The current provided in pulsed electrodeposition must overcome the over potential in order for deposition to occur at the rate of the average current density being supplied. The peak current applied to the cathode target can be split into two different quantities; the capacitive current which is responsible for charging of the double layer and faradic current which is responsible for the rate of deposition. The faradic current is a function of the changed percentage of the double layer; if the pulse on time is shorter than the charging time then the faradic current never reaches the peak current. If the pulse off time is shorter than the discharge time then the faradic current never reaches zero. Unsatisfactory charge and discharge times of the double layer can lead to inaccuracies in deposition rates because the peak current and null current are never reached changing the average current applied to the cathode target. A rapid method to determine the charging t_c and discharging $t_D$times were investigated and presented in Eqs. (40-41) below as a function of peak current, where the time is in µs. (Puippe 1980), (Kanani 2004)

$$t_c = \frac{17}{I_p} \tag{40}$$

$$t_D = \frac{120}{I_p} \tag{41}$$

As mentioned before the limiting current density is a factor in promoting mass transport to the cathode target, however the longer the pulse time the smaller the limiting current as described in Cottrell equation in Eq. 42 below. The time must be sufficient enough to charge the double layer but small enough to stay below the limiting current. A good criterion is that the ratio of the average current density over the limiting current density must stay be less than one meaning that the double layer is sufficiently charged while maximizing the limiting current to promote mass transport to the target surface (Madou 2002).

$$J_I = nFDC^0{}_\infty\sqrt{\frac{D}{\pi t}} \tag{42}$$

Electrodeposition or electroplating is an effective way to rapidly grow metal structures to great thicknesses in a relatively short time period. Many parameters can be altered to achieve the desired outcome such as the electrolyte bath composition, agitation, temperature, current and in the event of pulse plating the duty cycle of the pulse. The success of the processes of electroplating is not only dependent upon science but also skill and experience. With inexpensive equipment and a few metric experiments such as deposition rate and adhesion tests an effective electrodeposition process can be achieved. Electroplating was the primary method for growing the bridge and crucible structures used to characterize the thermodynamic properties of the biological samples.

Etching

Etching is a micromachining method that uses either a chemical (wet etching) or plasma (dry etching) process to selectively remove material by using photoresist as a masking template. The classification of etching can be either isotropic or anisotropic depending upon the material being etched and the process being used. With isotropic etching the material is etched uniformly in all directions as opposed to anisotropic etching where etching is directional depended as shown below in Fig. 40. However, wet etching profiles are seldom perfectly isotropic where both deep slopes and gently sloping sidewall profiles are possible. An undercutting bias occurs with a wet etching process; the undercutting profile should be similar to the desired depth of etching giving a larger etch profile than mask size. Typically, photoresist patterning is used as the mask for MEMS etching processes. The masks protect the undesired areas of the material from being etched while allowing the etching solution to etch away the desired areas. (Maluf and Williams 2004). (Franssila 2004).

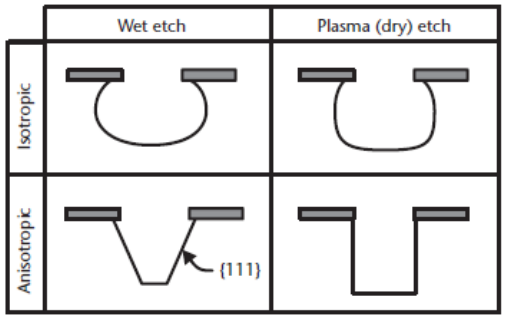

Figure 40. trench profiles of four different etching procedures. (Maluf and Williams 2004)

LIGA Conclusion

The LIGA process is complicated with many variables and factors that need to be considered when designing the procedures to create the desired structure. A plethora of

information concerning the optimal procedures and steps need to be thoroughly studied when going through the design processes in order to maximize time and cost efficiencies. It is at the upmost importance to document every step and prescribed settings that are used throughout the process as one change can have devastating results further down the process road map. There are many different paths that can be taken to achieve the same result but each process has to be studied to determine the feasibility and how practicable the process is for the individual user or lab. LIGA is a very effective process to create high quality and quantity micro-structures or devices used for studying biological samples and hence why it is used to create the DTA structures used in this study.

Chapter 6. Micro-D.T.A. Manufacturing Process

Equipment and Overview

The LIGA processes were done primarily in a low budget lab setting to speed up the process times by being independent upon the schedules of the MEMS and NEMS laboratories available. However, to achieve a high quality conductive layer the sputtering process was outsourced to another lab to create a few samples for use. The majority of the time spent during the LIGA process was learning the correct procedures to achieve the desired micro-mold structures using photoresist while the remaining time was dedicated to fine tuning the electroplating procedures. All characterizing of the molds and structures were also outsourced since the equipment needed is very expensive for small scale production.

The laboratory setting where the LIGA processing took place was not a standard MEMS processing lab as far as being a clean room but proper illumination equipment was implemented to prevent processing discrepancies. A laboratory clean room was not

necessary due to the large size of the structures being built (100~1000 µm) which would not be adversely affected by dust particles within the room. The laboratory was not equipped with any windows for any exterior light sources to enter the work environment, which could have devastating effects on the photoresist being used. Room illumination was supplied by standard fluorescent lights shielded with clear filter sleeves that are capable of blocking 390nm light and below which is above the sensitivity of the photoresist (<365nm).

Processing equipment used for the fabrication of the bridges was basic and comprised of a spin coater, exposure box, and microscopes for 1st order processing. A Spin 150-NPP single substrate spin processor was used to apply the resist which was capable of manual chemical dispenses and is completely enclosed for a repeatable spin environment. The main exposure box used was a Kinsten KVB-30D box designed for printed circuit board processing which included mercury lamps outputting 350~400nm light at 2~4 mW/cm^2 and a vacuum table for contact mask alignment. For first order processing 20x optical laboratory microscopes were used to visually check the outcome of each process and an 8MP web cam that was retrofitted to the microscopes were used to document the results. Most equipment used had custom alterations to achieve desirable results.

Manufacturing Process

Sputtering Nickel

As described in the proceeding LIGA processing steps, the first step is depositing a thin conductive seed layer to a silicon wafer by means of sputtering or evaporation to electroplate the main structure upon. Ideally, sputtering is the method of choice in MEMs

processing due to the ability to operate at low temperatures and achieve a more controlled environment thus sputtering was the method of choice. The conductive seed layer must be dissimilar to the material being used to grow the structure so that the seed layer can be selectively etched away while leaving the bridge unaltered. Based upon past research conducted by Ben Pepin the conductive seed layer was chosen to be Nickel due to less sputtering and etching difficulties (Pepin 2010). However, the Nickel layer will not adhere to the silicon wafer directly due to the natural oxide layer growing upon the silicon wafers. Titanium is deposited as an adhesion layer before the Nickel layer is to be deposited because Titanium reacts well with the natural oxide layer.

The sputtering process was outsourced to another lab due their ability to precisely control the thickness of the Titanium and Nickel film (Gangopadyay Laboratory University of Missouri). The Nickel film was deposited using a RF magnetron system (Orion, AJA international Inc). The silicon substrates were ultrasonically cleaned in acetone, methanol and DI water for 5 min in each solvent. These substrates were then dipped in 1:10 HF:Di water for one minute to remove the native oxide layer before loading into the deposition system. The base pressure and working pressure of the deposition system was 2.3x10^-7 Torr and 4mT respectively. A 5nm titanium layer is first deposited which acts an adhesion layer, then a 20nm nickel layer was deposited at 200 W DC, 4mT, 20sscm flow of Argon at room temperature. The deposition rate for 200 W DC was 6.66 nm/min and resulted in a uniformity of +/- 5nm.

Applied Photoresist

NR21-20000P

The photoresist used to create the micro-mold was chosen to be NR21-20000P which is a relatively new negative type thick photoresist produced by Futurrex. The resist is capable of achieving thicknesses of up to 125 microns and has specifications of superb adhesion during plating and easy removal during development. There are only a few photoresists available on the market that have the capability of achieving thicknesses of up to 100 microns and are compatible with UV exposure tools. SU-8 was also considered but it is mainly used for permanent structures causing it to be difficult to remove and not used as a sacrificial mold structure that is desirable for the purpose of this paper. NR21-20000P was used primarily because it was a less expensive thick photoresist that was offered in low quantities that was can be easily developed and removed. Unfortunately, because of NR21-20000P being relatively new there was very little documentation concerning development and problem shooting procedures.

Application of Photoresist

The NR21-20000P photoresist was applied to the Ni coated silicon wafers through the centrifugal spinning method after a thorough cleaning procedure was implemented to Ni coated silicon wafer. The nickel plated silicon substrates were processed as 2”x3” fragments and were packaged in 4” petri dishes and sealed in vacuum bags to prevent contamination from the non-filtered laboratory environment. The fragments were then carefully cut to 0.75” x 0.5” segments using a glass cutter to score and wafer pliers to selectively break the scored wafer. The cut wafer segments were then handled with tweezers and rinsed thoroughly in acetone, alcohol, and DI water until the surface was hydrophilic as shown in Fig 41. The wafers were then submersed in a

pickling solution for 60 seconds to remove any oxide layer that may have grown upon the surface; the procedures for preparing the pickling solution are displayed below in Table 9. The wafer samples were then removed from the pickling solution with tweezers and rinsed with acetone and DI water. To dry the samples and improve adhesion the wafers were placed on the wafer spinner and spun for 45 seconds at 5000 rpm and then placed on a hotplate at 90 °C for 10 minutes to ensure thorough removal of water on surface. The wafers were then placed on the wafer spinner again for 45 seconds at 5000 rpm to assist in cooling to room temperature.

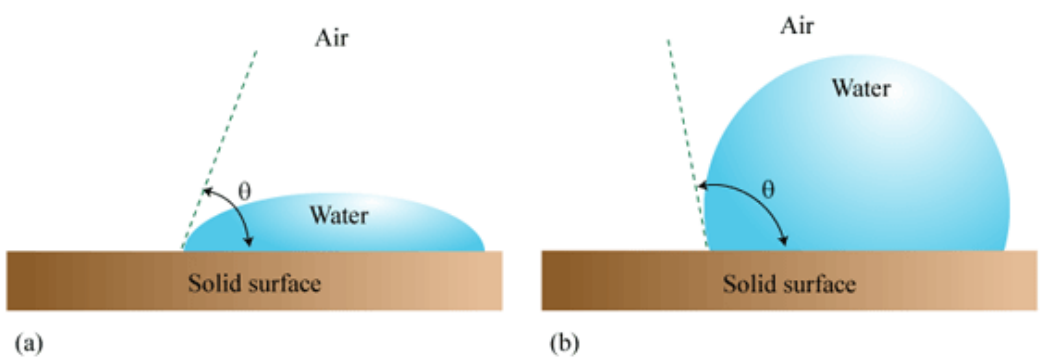

Figure 41. (a) Hydrophilic surface (b) Hydropholic surface (Mechanisms behind the Lotus effect n.d.)

Table 9. Pickling solution preparation procedure.

1. Fill a 500mL beaker cleaned with soap and rinsed with DI with 100mL of lukewarm DI water.
2. Slowly add 42.5grams of Sparex No.2 granular dry acid compound to the lukewarm water.
3. Use stir bar to stir solution until all of the pickling particles are dissolved.

Resistance Probe Measurement Process

Before resist is applied to the cleaned substrate electrical resistance was checked and recorded to ensure proper development later in the process and that the wafer was properly cleaned before any further processing would occur. A custom made electrical

resistance probe was constructed using a single electrical wire strand secured to a tongue depressor as the probe (approximately 200 µm in diameter). An alligator clip was used to secure the wafer and to also ground the resistance circuit as shown below in Fig. 42. A micro-manipulator and microscope was used to accurately position the wire probe at a desired location along the wafer, these instruments were critical for probing inside the microcavities later in the LIGA process as shown in Fig. 43. The probe was placed in multiple locations to ensure that the resistance was uniform throughout the entire surface of the wafer. The measurement was performed using a 2 wire resistance measurement to establish a reference resistance which was approximately between 11-15 ohms. If the resistance was elevated from the reference resistance after cleaning then the cleaning process was performed again to remove any oxides or organic materials that may be contributing to the increase in electrical resistance. This resistance measurement check was crucial to assure that electroplating would be successful later in the LIGA process.

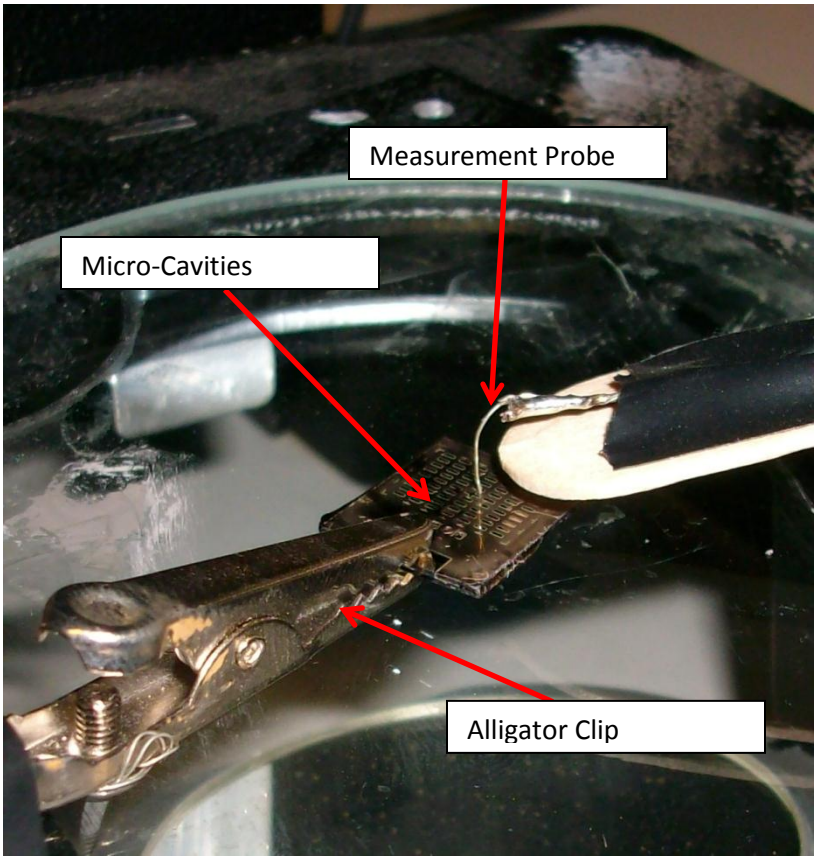

Figure 42. Resistance Probe Setup

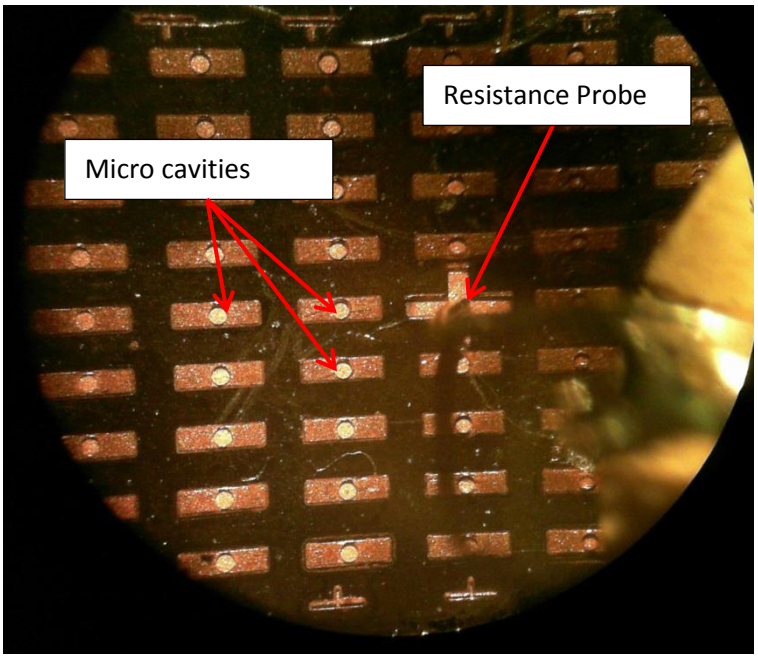

Figure 43. Microscope view of resistance probe being positioned in cavity

Spinning Process

The photoresist was applied to the wafer surface by manual operation and spun to the designated speed for desired resist thickness. The photoresist used was stored in a 10 mL syringe that was continuously covered with aluminum foil and capped off and stored upright in a refrigerator at 5 C°. Every 2 weeks the syringe was replenished with fresh photoresist from the main supply to ensure active photoresist. The main supply of photoresist was stored in an amber bottle in a refrigerator at 5 °C to guarantee shelf life storage for 1 year. Recommended application of resist is 7mL per 6 inch diameter wafer which equates to 0.1 mL of resist dispensing for the 0.5" x 0.75" silicon wafer used. To alleviate any air bubbles that may have been trapped in the needle, a small amount of resist was dispensed into a Kim wipe before each use. A silicon wafer was then placed in the center of the chuck and a vacuum seal was applied to secure the wafer in place during the spin series. The photoresist was then slowly dispensed on the static wafer in a rectangular swirl pattern going from the center out to improve uniformity during the spin. Spin settings for desired thickness are displayed below in Table 10.

Table 10. Prescribed settings for desired thickness.

Thickness (µm)	1st spin speed (rpm)	1st spin time (s)	1st spin acceleration (rpm/s)	2nd spin speed (rpm)	2nd spin time (s)	2nd spin acceleration (rpm/s)
20	3000	40	3100	0	0	0
40	3150	10	3300	0	0	0
50	1500	10	1600	0	0	0
70	1975	6	2000	100	120	100
100	1200	10	1300	100	120	100
120	1050	10	1200	100	120	100

After each photoresist coating process the coated wafer was allowed to sit for a predetermined amount of time to achieve better results. After experience was gained on working with photoresist, it was learned to place the freshly coated substrate on a perfectly level surface while placing a small petri dish over the coated wafer to prevent solvent evaporation. Often after a spin coating process small air bubbles are suspended in the resist which if left to sit for a predetermined amount of time (~20 min/10 µm) would allow the bubbles to dissipate in the atmosphere. Edge beading often was a result after spinning at prescribed settings for thick photo resist layers (>30µm) and if allowed to sit the photoresist would re-flow into a more uniform layer which is desired for exposure. It was until after many trials of the LIGA process this step was learned and was a key step for the success of the final product.

Soft Baking Procedures

The next step after the application of resist is to evaporate the solvent within the resist by means of a heated source to create a rigid surface for mask alignment and UV exposure. A HP-30 Echotherm digital hotplate was used as the heated source to accurately heat the coated wafer to the prescribed temperature as indicated in Table 11 below. First a two-way bubble level was used to assure the hotplate surface was perfectly level so a more uniform photoresist layer would occur as a result. An external type E thermocouple probe was used to cross check the surface temperature at a designated location of the hotplate for quality assurance. Once the levelness and temperature have been calibrated; using tweezers a coated wafer was placed close to an outer edge for 10 seconds and then moved to the designated location to have a temperature ramp affect. Implementing the temperature ramp during the soft bake results in a more uniform surface and pitting caused from rapidly expanded suspended gases is drastically reduced.

After the coated substrate has been successfully soft baked the wafer was removed from the hot plate and placed in cooling rack made from expanding foam to reduce thermal stresses due to cooling too rapidly.

Table 11. Soft baking procedures as a function of photoresist thickness

Thickness (µm)	1st Soft bake Temperature (°C)	1st Soft Bake Time (s)	2nd Soft bake Temperature (°C)	2nd Soft Bake Time (s)
20	150	120	NA	NA
40	150	180	NA	NA
50	150	150	NA	NA
70	150	300	NA	NA
100	80	600	150	300
120	80	600	150	300

Mask Design

Overview

Due to the NR21-20000P resist being a negative type resist the images transferred onto the resist will be negative to the images on the mask after development. The UV absorbing images will block the UV light from chemically strengthening the composition of the resist so that the un-exposed portions can be chemically etched away creating micro-molds. Alternatively, the UV blocking images will subsequently be positively transferred into micro-molds in the resist after chemical development. The negative image transfer was considered when subsequently designing the overall UV absorbing mask design.

Mask Design Process

The UV absorbing mask design is dependent upon the manufacturing process of the bridge while keeping mechanical integrity of the micro-mold, uniformity of current density, and user integration as a design constraint. The general mask design consisted of

a 7x9 array of structures to improve current uniformity while increasing the electroplatable surface area as shown in Fig 44. Increasing the electroplating surface area elevates the electrical current required for desired material growth within the electrical current ranges achieved by the available power supplies. The array also was used to reduce photoresist stresses during development and electroplating and increase the probability of a successful bridge outcome. The mask design included fiducial marks for subsequent mask alignments and a mask label to help identify the type of mask used and mask orientation. Printing on the mask was orientated to read correctly on the bottom side of the transparency material as shown in Fig. 45, this was done to ensure that the UV mask was directly in contact with the photoresist if the label read correctly. Lastly, the mask design allows for an alligator terminal clip for electrical ground and controllable submersion of the resist layered wafer into the electroplating bath.

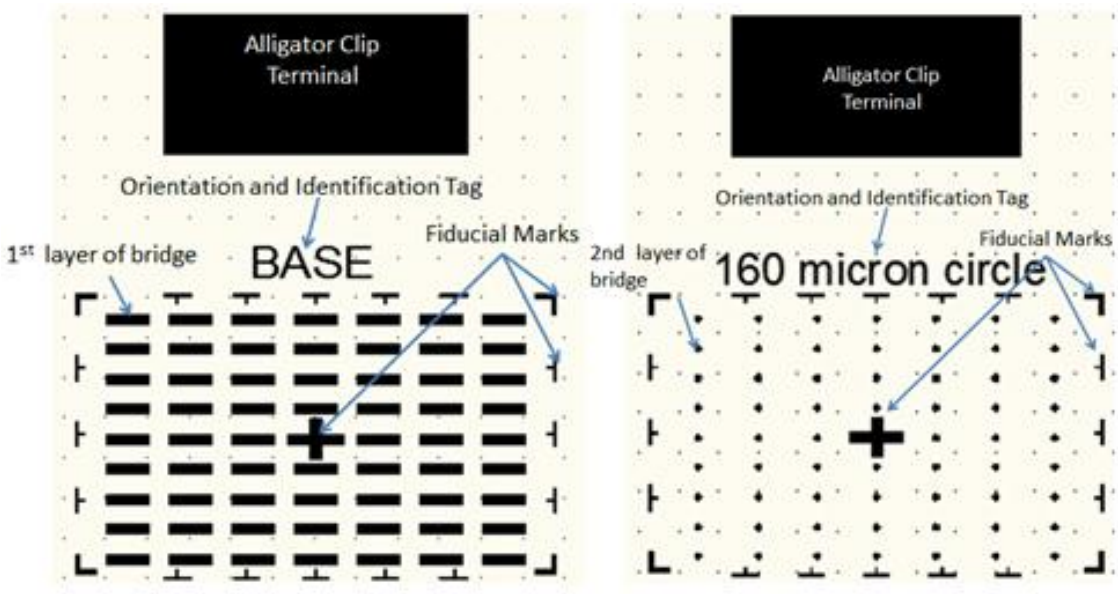

Figure 44. Mask Design created by Fine Line Imaging with 20 µm resolution

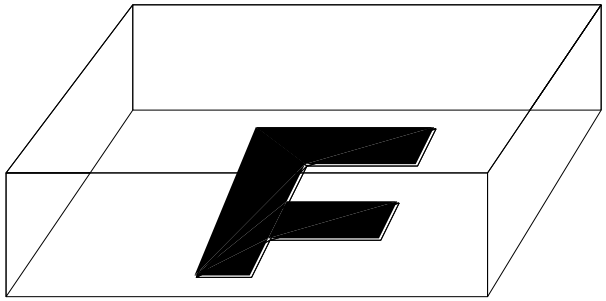

Figure 45. Mask Printing Orientation, Read Correctly On Bottom

The fabrication process consists of three steps which include the base, the cylinder, and isotropic etching of the cylinder as illustrated in Fig. 46 below. The bridge base was designed to be 250 or 300µm wide, 1000 µm long and 30 µm thick to minimize thermal mass while keeping mechanical integrity when handled for succeeding manufacturing steps. The left mask design displayed in the Fig. 44 was used to create the micro-molds for growing the bridge bases. After the bases were grown the crucibles were then created in a two-step process which included growing a solid cylinder and then isotropically etching a bowl shaped crucible into the cylinder. The cylinder's diameter ranges from 300 µm to 200 µm depending upon the size of the biological sample being tested. A similar mask to the right mask design displayed in Fig. 44 assisted in the formation of the molds to grow the cylinders. Once the cylinders were grown, isotropic etching was initiated to create the desired bowl shaped crucible. The diameter of the bowl ranges from ~290 µm to 160 µm again depending upon the size of the sample.

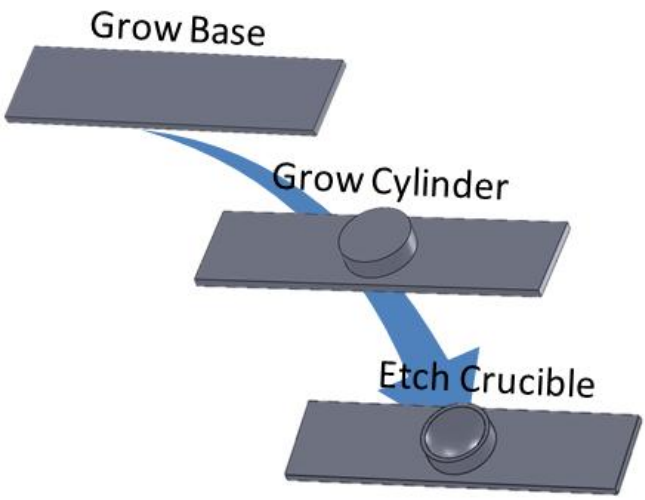

Figure 46. Gross Bridge Fabrication Process

Exposure

Exposure of the photoresist layered nickel plated wafers was performed using a modified printed circuit board exposure box made by Kinsten. After experiencing undesirable exposure results some modifications and corrections were implemented because the exposure box was not designed to expose thick film resists nor small dimension features. It was found that indirect UV rays were leaking under the mask creating smaller than desired features. A ¼ inch thick poster board with a 1”x1” square cut in the middle was used to block the indirect UV light from reaching the wafer. The simple implication of the modified cardboard resulted in high fidelity results and the ability to achieve smaller dimensions.

The mask alignment and photoresist exposure procedures were mostly manually involved. Using tweezers the photoresist covered wafer was placed in the center of the exposure box on a mark designated to make certain repeatable placement and exposure dosage of the substrate. For the first exposure of the photoresist covered substrate the

mask labeled “BASE” was placed on top of the wafer while insuring that the label “BASE was read correctly so that the UV absorbing mask was in direct contact with the photoresist. Then the vacuum table lid was closed over the mask and substrate and the vacuum pump was engaged to cause the polyethylene type cover to secure the mask in place over the wafer. The modified cardboard was then placed over the vacuum table and the exposure box was closed for exposure as shown in Fig 47. The correct time in seconds on the timer was established by multiplying the photoresist thickness T by the photoresist sensitivity S and dividing by the power density P output of the exposure box shown in Eq. 34 below. The exposing time of the first layer (40 micron thick) was calculated to be 446 seconds with the sensitivity of the photoresist being 46 mJ/cm^2per micron thickness. The power density output was measured at the middle of the exposure box and determined to be 4.2 mW/cm^2.

$$t = \frac{T*S}{P} \tag{34}$$

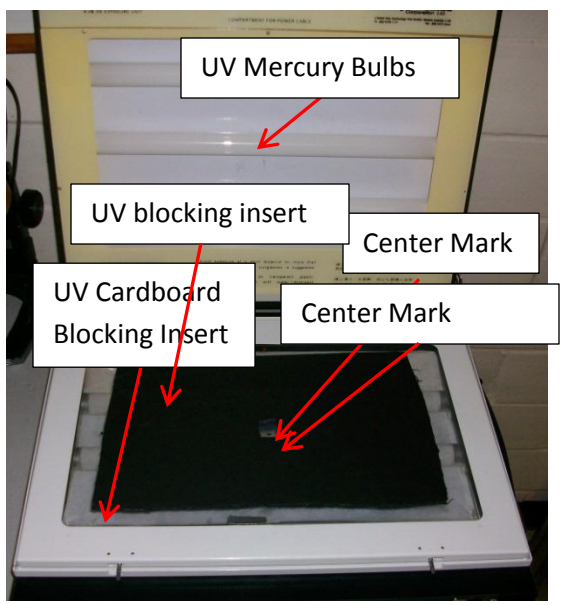

Figure 47. Exposure Box with UV blocking cardboard insert

Subsequent mask placement was more involved to ensure that the fiducial markings of the mask aligned with the preceding grown fiducial markings. A modified microscope with a UV filter covered microscope light was used to assist in the mask alignment as shown in Fig 48. The microscope was placed over the mask and photoresist covered wafer then using tweezers the mask was gently moved in the correct position as shown in Fig 49. The vacuum lid was then closed and tweezers were used to press down upon the vacuum cover onto the mask and wafer to confirm that the mask did not alter its position while the vacuum was in process. The tweezers were pressed against the alligator clip terminal location on the mask so to not deform the photoresist in critical regions on the wafer. The microscope was used to check the mask alignment after the vacuum process was completed. The process was very manually tedious and usually required multiple trials as the mask often altered its position during the vacuum process. Typically the subsequent mask alignment was not aligned correctly; after the process was optimized a mask aligner was used at a different lab.

Figure 48. Modified microscope used as mask aligner

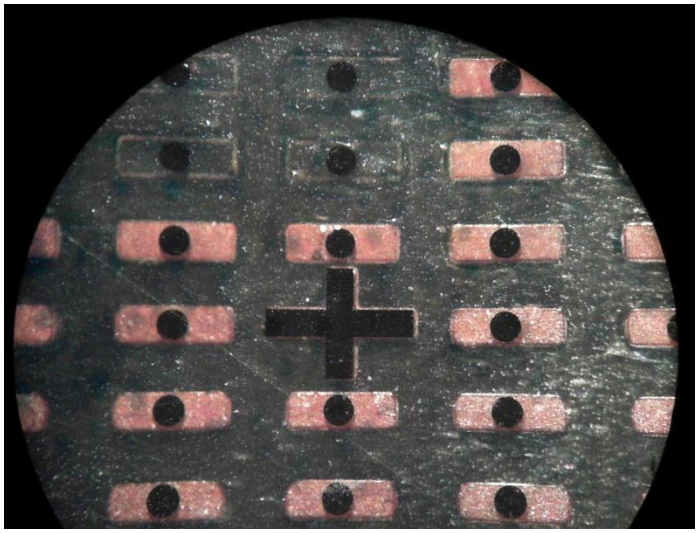

Figure 49. UV absorbing mask over laying existing topological features.

Post Exposure Relaxation

After many trials of the LIGA process it was found that after the wafer was exposed it needed to be left to set at least 24 hours to prevent critical photoresist cracking during development. During UV exposure the photoresist goes under a chemical

transformation with nitrogen and other gases being bi-products. The gases are trapped within the photoresist and if a post exposure bake was implemented immediately after exposure the expanding gases cause stresses within the resist leading to severe cracking during chemical development. If the exposed photoresist was left to sit, the photoresist will eventually outgas the gases, which prevent stresses that lead to cracking during development. A study has not been conducted to determine the optimal time for adequate outgassing to occur but 24 hours has been proven to be effective. Other procedures were performed to prevent cracking such as lowering the baking temperatures and performing temperature ramps but doing so caused other developing and also electroplating problems. The procedures will be discussed in more detail in the results section.

Post Exposure Bake Procedures

After adequate time for sufficient outgassing of the exposed photoresist the next processes is to strengthen the photoresist by raising the temperature of the resist to the softening point, this process is called post exposure bake (PEB). The process was necessary to crosslink the monomers created from exposure to polymers. The post exposure bake was performed on the HP-30 Echotherm digital hotplate and the proper post exposure baking temperature (80 °C) was checked using a type E thermocouple probe at a designated location. It was found that a sufficient temperature ramp was needed to prevent cracking from occurring during chemical development. The temperature ramp assists in relaxing any residual stresses that may have occurred during soft baking and exposure. The temperature ramp was performed by placing the substrate upon the outer edge of the hotplate and moved approximately 1” inward towards the designated position upon the hotplate every 15 seconds until the substrate met the desired location. Once the proper time for PEB has been reached the substrates were placed in the

Great Stuff fabricated cooling rack to slowly cool the substrates to room temperature (approx. 900s). The proper PEB times are a function of the photoresist thickness and displayed below in Table 12.

Table 12. Post Exposure Bake Procedures (Futurrex)

Thickness (µm)	PEB Temperature (°C)	PEB Time (s)
20	80	300
40	80	300
50	80	300
70	80	300
100	80	600
120	80	600

Photo Resist Development

After the substrates have been sufficiently cooled to room temperature the next process is to develop the resist chemically which selectively etches the unexposed regions of the photoresist to create the micro-molds. The chemical used to etch the unexposed resist is RD6 another Futurrex product. The active chemical used in RD6 is Tetramethylamonium or TMM which is a common developing solution used in industry. A 200mL beaker was cleaned with soap and tap water and then rinsed with DI water to contain the RD6 solution. Approximately 10 mL of RD6 was poured in the 200mL or an adequate amount to sufficiently submerge the substrate. The substrate was then placed in the solution and aluminum foil was placed over the opening of the beaker to prevent any solution from escaping during the development process. The RD6 in the breaker was then manually swashed around to provide adequate agitation to aid in etching the unexposed photoresist. After the prescribed developing time has been reached the substrate was then taken out of the RD6 solution with tweezers and thoroughly rinsed with DI water and then dried using the wafer spinner set at 5000 rpm at 45 seconds.

Post Development Resistance Testing

After etching the micro-cavities it is essential to assure that the electrical resistance within the micro-cavities is at the reference resistance level that was measured before the application of resist upon the nickel coated substrate. If the electrical resistance is elevated an order of magnitude above the reference measurement then there typically exists a small layer of resist within the micro-cavity causing the elevated resistance. If the resistance was too high then the substrate was then re-developed for 10 more seconds to remove the unwanted resist layer for improved electroplating adhesion.

The electrical resistance measurement involved checking the base micro-mold cavities located at the corners of the array and also the middle fudicial mark as shown in Fig 41. Unfortunately, the microprobe is not small enough to fit inside the cylinder micro-mold cavities; the middle fudicial mark is checked and is assumed to represent the resistivity of the entire wafer. Often the probe is placed directly on the alligator clip to assure that there exists no soil located upon the tip of the probe that may misrepresent the measurement. Before the resistance measurement method was implemented the micro-molds were inspected using a microscope while adjusting the light angle upon the substrate to identify residual resist within the cavities. If the residual resist was only a few microns thick, it was difficult to identify the unwanted resist and often caused plating failure. The electrical resistance measurement method was very reliable in identifying problems that would impede successful plating within the micro-molds. Electroplating Station

The electroplating station was arranged using a 500 mL beaker, a pure copper rod, a hotplate with magnetic stirrer, an alligator clip, and a DC power supply with additional

circuitry as shown in Fig 50. The 500 mL beaker held the electroplating solution and allowed sufficient room for adequate distance between the copper anode and nickel substrate cathode to improve plating uniformity. A pure copper rod anode was purchased to improve the deposition outcome, as copper wire purchased from the hardware store did not prove successful results. A magnetic stir rod operated from the Lab Depot Inc. hotplate was used for sufficient electrolyte solution agitation to improve the solution's electrical current throwing power. The alligator clip was used to complete the electrical circuit and to also securely grasp and submerge the nickel plated wafer within the electrolyte solution. The electroplating station was designed to be very basic and simple to use as to help keep the processes as repeatable as possible.

Electroplating

Once the micro-mold cavities have been successfully created the desired structures could now be grown through electrodeposition or electroplating. Standard direct current electroplating was initially used as the first order fabrication setup but later pulsed plating was implemented for the success of the copper deposition. A variety of other different procedures were implemented to optimize the electroplating process for the desired outcome. The other procedures will be left out from this section and mentioned in more detail in the results section while only the successful setup with be explained in detail in the following paragraphs.

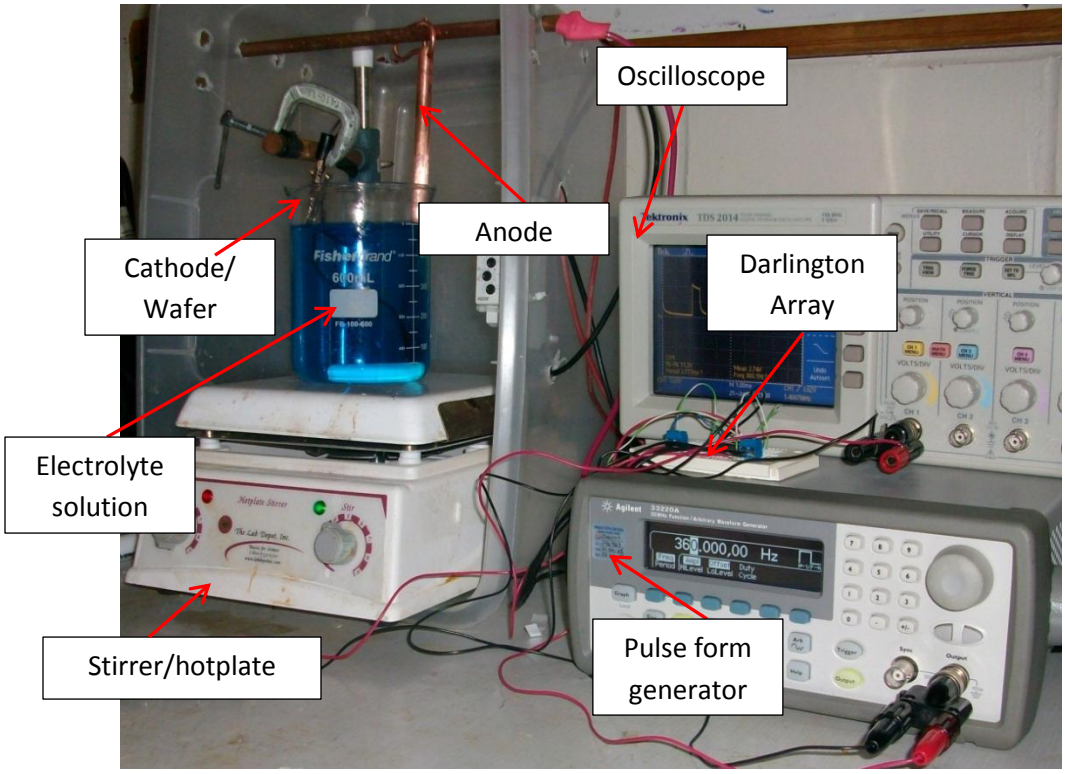

Figure 50. Plating Station with electronics

Electrolyte Solution

The electrolyte solution used was a mixture of DI water, sulfuric acid, and copper sulfate to effectively transfer the copper ions from the copper rod to the surface of the resist covered nickel plated wafer. The electrolyte solution was decided to be without leveling and brightening agents to reduce the amount of variables in the electroplating processes. The other reason why leveling and brightening agents were not introduced to the solution was because they can affect the mechanical integrity and adhesion of the plated copper. Once the electrolyte bath was created, it was used for approximately 10 trials before it was replaced with a new bath to reduce the amount of impurities into the solution. The recipe and procedures for developing the electrolyte solution was borrowed

from electroplating procedures from other laboratories and kept relatively constant throughout the trials, the technique is displayed below in Table 13.

Table 13. Electrolyte Bath Procedure

1.	Wear protective gloves and eye gear throughout the experiment.
2.	Clean a 500mL beaker with Acetone, then rinse with DI water and dry using Kim Wipes
3.	Fill the 500mL beaker with 175mL of DI water
4.	Use the scale to measure 60g of Copper Sulfate and then add to the 500mL beaker
5.	Measure out 40mL of Sulfuric Acid and then slowly pour into the 500mL beaker
6.	Pour DI water into the 500mL beaker until the fluid level reaches the 500mL mark

Current Density Overview and Equipment

For the prescribed electrolyte solution used the most influential factor for determining the quality of plating was the electrical current profile supplied to the electroplating station. The minimal conductive surface available for electroplating was between 0.15 and 0.02 cm^2 which to achieve a current density of 10 $\mathrm{mA/cm^2}$ the current needed to be between 1.5 and 0.2mA non-pulsed current. However, with the implication of pulsed plating and a duty cycle of 50% and lower, the current outputted from the power supply can be increased to more attainable levels while achieving the desired current density. An Agilent N6700B DC power supply capable of achieving current levels down to 0.1 mA was used to supply the electrical current for electrodeposition.

Additional circuitry consisted of an Agilent 33220A pulse wave generator and a 2803 Darlington array to rapidly switch the current supplied from the DC power supply to the desired square wave pulse frequency. A mechanical switch or relay was not capable of achieving the frequencies that was needed for proper pulse plating thus solid

state switches are ideal to use for our purposes. A Darlington array was chosen because it is capable of frequencies of up to 1 MHz and able to handle up to 500mA. The function generator (Agilent 33220A pulse wave generator or Arduino Uno) was used to control the Darlington array to turn the DC current on and off so the desired square pulse wave was achieved. The circuitry and equipment setup necessary for electrodepositon is shown below in Fig. 51. The present setup was capable of achieving the necessary electrical current magnitudes and frequencies for improved copper plating.

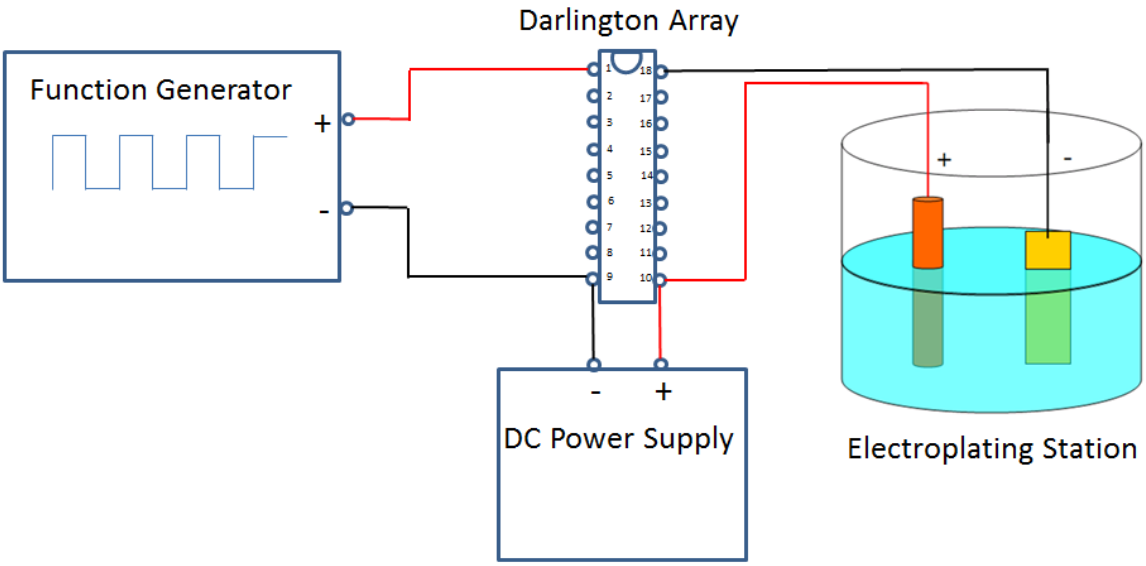

Figure 51. Electrical diagram for pulsed plating

Electroplating Procedures

After the electrolyte solution and necessary electrical equipment was properly created and setup, plating copper within the micro-mold cavities was able to begin. The electrolyte solution was placed upon the hotplate with an acetone and DI water cleaned magnetic stir rod placed in the solution. The stir setting was set to 2-3 which created a slight whirl indentation at the surface of the solution, this was necessary for adequate

solution agitation. The copper anode was thoroughly cleaned using a fine grain sandpaper to remove any oxide that may have been upon the surface and then excessively washed using DI water and acetone to wash away any copper particles left over from sanding. The copper anode rod was then dipped in degreasing solution to guarantee a hydrophilic surface followed by an acetone and DI rinse. Next, the copper anode was placed in the electrolyte solution close to the edge of the beaker to allow the maximum amount of distance from the cathode. Then, the alligator clip was then used to clip the wafer at the alligator clip terminal for proper grounding of the circuit. Finally, the wafer was then lowered into the electrolyte bath until all of the micro-mold and fudicial cavities were sufficiently immersed with the solution. It was important that the alligator clip terminal was never submerged within the electrolyte solution because the current would favor the clip and terminal increasing the current density at that region causing uneven deposition as shown in Fig. 52 below.

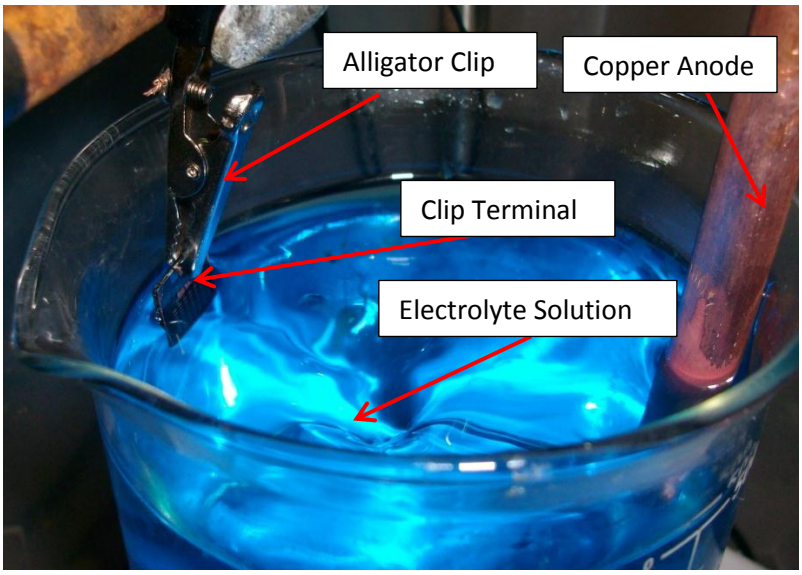

Figure 52. Wafer position in electrolyte bath

Determining Duty Cycle and Frequency

The electrical current profile settings were then calculated and implemented by adjusting both the DC power supply and the function generator. The current profile settings were dependent upon if either the base or the cylinder structures were grown due to the different surface areas introduced into the system. The sum of the surface areas of only the main structures were used to calculate the proper electrical current required based upon the target current density of 10 mA/ cm^2. Using Eqs. (38-41) the electrical current pulse profile can be determined and implemented into the equipment used. Unfortunately, using Eqs. (38-41) the duty cycle was calculated to be 12% which is below the minimum limit of what the function generator can perform (20%). Setting the duty cycle to 20% and the required time to switch off T_{off} to be constant, Eq. 45 was created from Eq. 38 and used to determine the required time to switch on T_{on}. This modification increased the switching time on 76% longer than the recommended time according to Eq. 40 however, the ratio of the average current density over the limiting current density is ~0.05 which is under the recommended limit of 1. The ratio ensures that the double layer is fully charged while maximizing mass transport to the cathode surface. The method for obtaining the limiting current density will be described in the following sections.

$$T_{on} = \frac{T_{off}0.2}{(1-0.2)} \tag{45}$$

The prescribed settings for pulsed electroplating are shown below in Table 14 below. The current supplied and current density shown in Table 14 is the electrical current supplied from the power supply and the current density if the duty cycle was 100%. The average current density is the lowered current density due to the implication

of the 20% duty cycle and is used as the desired current density for electrodeposition. The duty cycle and frequency were kept constant throughout the pulse plating series however; these settings can be altered to potentially improve plating results.

Table 14. Electrical current profile settings for pulsed electroplating

	Base	200 µm Cylinder	250 µm Cylinder	300 µm Cylinder
Area (cm^2)	0.158	0.019	0.03	0.04
Current Supplied (mA)	8.54	1.07	1.67	2.41
Current Density (mA/cm^2)	54.2	54.2	54.2	54.2
Average Current Density (mA/cm^2)	10	10	10	10
Duty Cycle (%)	20	20	20	20
Frequency (Hz)	361	361	361	361

Determining the Limiting Current Density

The limiting current density of the electrolyte solution was determined using an empirical approach borrowed from techniques used by Lee (Lee, Strathmann and Moon, Determination of the limiting current density in electrodialysis desalination as a emperical function of linear velocity 2005). A nickel plated electrical probe was used as the anode and a bare nickel plated silicon wafer was used as the cathode for the test series. Similar metals were used as both the cathode and anode because the voltage potential should not change drastically as a function of deposition growth. Next, the current was incrementally raised from 0.05 to 0.5 A while recording the voltage potential for 120 seconds at a sampling rate of 1 Hz. The voltage data points were then averaged for each electrical current step and then a plot of current density vs. voltage was created as shown in Fig. 53 below. The limiting current density was determined where the slope of current vs. voltage potential (inverse of resistance) was changed which indicates that all of the species are consumed and the resistivity changes. The limiting current density

of LCD was determined be ~0.2 A/ cm^2 which allows the ratio of the average current density and the LCD to be below the maximum limit for adequate plating results (Lee, Strathmann and Moon, Determination of the limiting current density in electrodialysis desalination as an empirical function of linear velocity 2006).

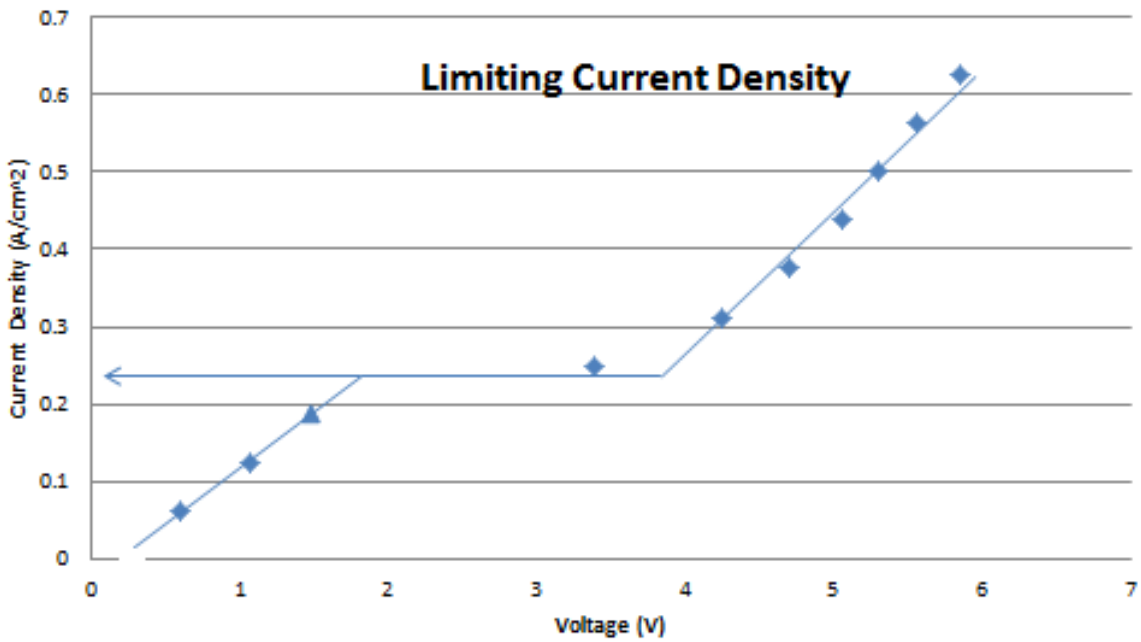

Figure 53. Limiting Current Density

Electroplating Time

The time of electroplating was dependent upon the height of which structure was being grown. The thickness of the base structure was designed to be 30 µm whereas the height of the cylinder was designed to be between 70-100 µm depending upon the size of the sample being measured in the crucible. The electroplating times were calculated using a mass transport equation which gave a good approximation of the thickness given the density ρ, atomic weight M_w, moles of electrons *n*, time *t*, Faraday's constant *F*, and current density I/A within the electrolyte solution as shown in Eq. 46 below.

(Schlesinger and Paunovic 2000) (Paunovic and Schlesinger 1998). The analysis of the estimated thickness was simplistic due to the time being the only variable that was not held constant in Eq. 46. Table 15. displays the appropriate values for Eq. 46 to achieve the desired height. Electroplating deposition results are displayed in the results section for the validity of Eq. 46.

$$T = \frac{M_w I t}{nFA\rho} \tag{46}$$

Table 15. Recommended values for desired growth height.

Height (µm)	Mw (g/Mol)	I/A (mA/cm^2)	Rho (g/m^3)	n (Mole)	F (C/Mol)	t (s)
30	63.54	10	8.96	2	96485.4	7380
45	63.54	10	8.96	2	96485.4	7900
50	63.54	10	8.96	2	96485.4	8778
60	63.54	10	8.96	2	96485.4	10533
70	63.54	10	8.96	2	96485.4	12289

Striking

The initial settings for the electroplating process were slightly altered for the first few minutes to ensure a good base plate for further plating. Initially, there typically exists a potential barrier on the surface of the cathode that will not allow adequate plating if the voltage potential is not great enough to overcome. Raising the current density to overcome this potential barrier ensure s that a good adherence of the electroplating material to the base metal will occur. The process of increasing the current density to begin a good thin base layer is called a “strike” or a “flash” (M. Schlesinger 2010). The initial current density was raised 150% of the recommended value, which would equate to 15 mA/cm^2. The “strike setting” was performed for 3 minutes to approximately build an initial layer of 1 µm for a good foundation for subsequent electroplating growth.

Smoothing

It was found that the surface roughness after the initial base deposit decreased the likelihood of successful resist removal during development. The lower development rate is due to the resist filling in the micro-crevasses and voids inhibiting the developing solution from successfully reaching the resist. This increases the chances of poor results during proceeding electroplating steps due to higher voltage potential or increases the likelihood of under etching if developed longer than recommended time. To reduce the surface roughness the current density was lowered 150% or to 5 mA/cm^2 during the last 10 microns of growth for a smoother finish. This improved the overall quality of the deposition and allowed for a higher success probability of latter electrodeposits.

Resist Removal

Once the electroplating process was completed and successful growth of copper within the micro-cavities has occurred the next process was to remove the remaining photoresist. The photoresist micro-mold cavities were designed to be sacrificial meaning after the structure was built the molds were then removed leaving only the base or base and cylinder in its pure form. The resist is vulnerable and dissolvable in Futurrex's RR41 which is mainly composed of dimethyl sulfoxide; also similar effects have been observed from exposure to acetone. To successfully remove the sacrificial photoresist the coated wafer was placed in a 200 mL beaker filled with 25 mL of RR41 then the opening of the beaker was sealed using aluminum foil and the solution was agitated using a swashing motion. After 60s to 90s of adequate agitation the wafer was removed using tweezers and visually inspected for any photoresist residue remaining on the surface of the wafer, if so the wafer was placed back in the solution again for 30 more seconds. Once thoroughly

cleaned the wafer was then rinsed off with acetone and DI water to ensure the entire RR41 chemical was removed from the surface.

Etching

Etching was performed as the last step in the bridge manufacturing process and was the least problematic of all of the steps. Similar to electroplating, etching requires the buildup of a photoresist layer however; the resist will serve as a mask to protect the copper from the etching solution. A model of the photoresist mask was created to determine the overall diameter D of the crucible based upon the opening diameter of the photoresist mask d, the depth of the crucible h, and the undercutting correction factor C_f as shown in Fig 54 and Eq. 47 below.

$$D = d + 2hC_f \tag{47}$$

The model is based upon the assumption that perfect isotropic etching of the material occurs ($C_f = 1$). During isotropic etching the etchant moves downward and outward from the opening of the mask while simultaneously undercutting the mask (Gad-el-Hak 2006). The isotropic assumption is largely dependent upon of the diameter of photoresist mask opening and solution agitation due to the ability of new etching solution reaching the material while the old solution and material are being transported away. The larger the photoresist opening diameter with constant crucible height the more isotropic the etching process will be while decreasing the aspect ratio of the crucible.

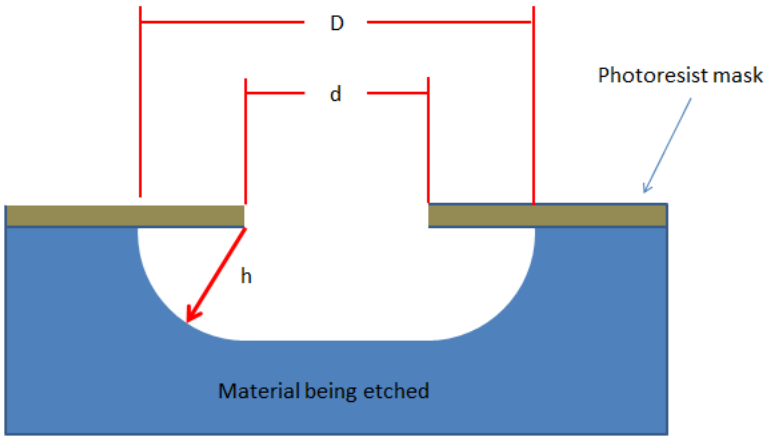

Figure 54. Photoresist mask design

Etching Procedure

The procedure for etching the bowl was borrowed from techniques used by printed circuit board hobbyists. The copper etching solution used was a standard PCB etchant solution, which contains ferric chloride as the main ingredient for etching. A small Tupperware container was filled with the PCB etchant solution until a level of 0.5" was reached for sufficient agitation and wetting of the wafer. An aquarium air pump was used to provide oxidation within the etchant solution as well as sufficient agitation. The Tupperware (R) containing the etchant solution was placed in a slightly larger container filled with hot tap water to increase etching rate and to help contain the bubbling solution. An air hose extending from the aquarium air pump was secured in an etching fixture and placed inside the Tupperware container so that the hose was completely submerged within the solution. Then the photoresist mask bridge-cylinder array was then placed in the solution located near the exit nozzle of the air hose for proper agitation as shown in Fig 55. The wafer was then removed after the optimal time has been reached and rinsed of with DI water followed by the resist removal as discussed earlier. The optimal time was determined using an in-house study discussed in the following paragraphs.

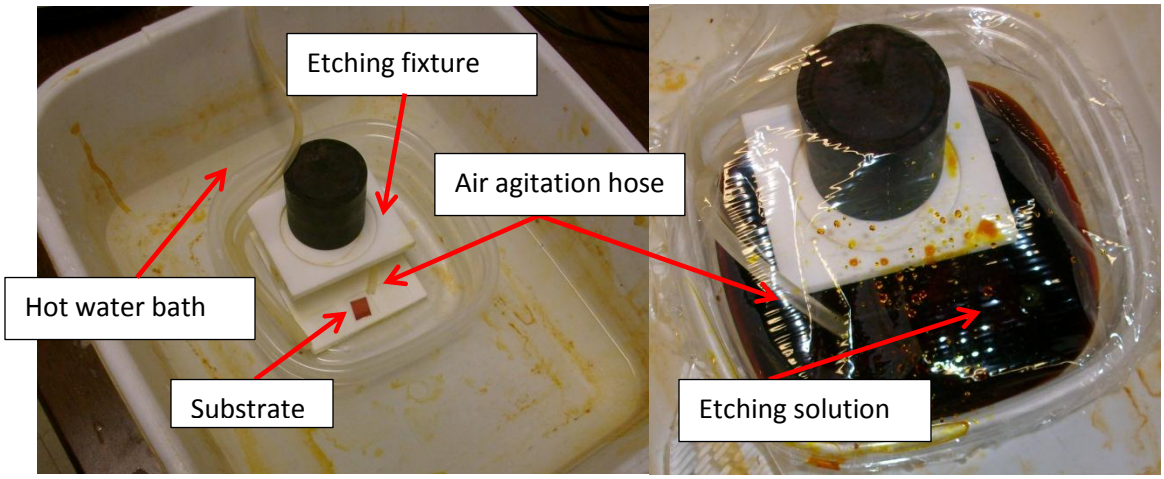

Figure 55. Etching station

Etching time study

Proper etching time is crucial in fabricating the desired bowl shaped crucible. A study conducted by Jian concluded that the etching rate of copper submerged into a fresh batch of Ferric Chloride at 25 °C was to be 18 µm/min (Jain, et al. 1998). However, a study was conducted to determine the accuracy of Jian's results with the use of micron sized masks. The in house study involved the use of a variety of etching masks and small pieces of pure copper foil to determine the most optimal choice in etch mask design and etching time. First, a small piece of copper was cut from the copper foil and flattened using a flat surfaced tool. Then, a layer of 20µm thick photoresist was applied using the spin 150 spinner. The resist was then soft baked, exposed, post exposure baked, developed and the cavity resistance was checked as described earlier. The true diameters of the cavities were then measured using a micrometer stage, microscope camera, and image J for later data analysis. A black sharpie then was used to coat the back side of the copper piece to prevent the etching solution from attacking the copper from the opposite side of the mask.

The photoresist masked copper foil was then placed in the etching bath as described earlier. After the determined time as been reached the copper piece was removed from the bath and rinsed with DI water. A microscope inspection of the copper piece was used to determine if etching occurred, if not the piece was developed 10 seconds longer then the etching procedure restarted. Once the copper samples were all etched according to the test matrix, the samples were then inspected using an optical profilometer to determine the diameter, depth, and shape of the crucibles. The optimal combination was then used as the prescribed procedure for manufacturing the desired bowl shaped crucible.

Bridge Release Etching

After the bridge has been successfully grown and etched for the final product the last step is to release the bridge from the nickel base metal. As mentioned before nickel was chosen as it is a desired base metal for electrodepositon and also it is non-problematic for selective etching. A non-phosphorus based nickel etching powder solution was used to perform the etching process; the procedures for correct mixing of the power are displayed in Table 16. below. Once the nickel etching powder was dissolved a custom made etching stand was placed in the beaker. The etching stand was produced from gypsum through a rapid prototype machine. A cheese cloth was used as a screen to collect any bridges that have been etched from the nickel base. The stand was designed to allow sufficient solution movement across the substrate while preventing any bridge structures from being damaged by the stir bar once etched from the nickel base. Etching time was stated to be ~50 µm/hour

Table 16. Procedures for Mixing Nickel Etching Solution

1.	Fill 500 mL beaker with 400 mL of water and add stir bar
2.	Place beaker on hot plate set temperature to 1 and stir bar on 6.
3.	Add 48 grams of MXB929 Nickel Stripper Powder from Caswell
4.	Wait until powder is completely dissolved and temperature constant.

Sample Characterization

Microscope camera

To characterize the samples after the processes were performed a few procedures and equipment was used to better assist in assessing the quality of the end process. As a first order evaluation, a 70X microscope along with a modified 8 MP web camera was used. The microscope was used to assess the sharpness of the micro-mold patterns after exposure and the quality of the etched cavities after development. The microscope and camera was also able to determine approximate width and length sizes with the assistance from a 25mm stage micrometer and an open source image program called Image J. An out-of-house optical profilometer was used to determine the mold depth and the slope of the mold walls as thick resist development tends to have effects of dark erosion, which cause sloped walls. Also, the profilometer assisted in determining the volume of the crucible after etching. A scanning electron microscope (SEM) aided in evaluating the thickness of the electroplating deposition for studies to determine the accuracy of Eq. 46 above.

For time and convenience considerations most characterization was performed using the 8 MP camera, microscope, stage micrometer, and the Image J program to abstract length and width information from the micro-cavities and from the electroplated structures. The object being measured was placed under the microscope objective lens

and positioned until the desired structure is in view from the microscope eyepiece lens. Then, the 25 mm stage micrometer was placed on top of the structure upside down so that both the measurement markers of the stage micrometer and structure are both in focus at the same time. Then the course focus was adjusted so that the object is in focus to ensure that both the measurement scale and object was in focus. The camera was then activated via the camera's software package and the 8MP option was chosen to take pictures at the best resolution. The auto focus was turned off and the brightness setting was adjusted for a clear picture on the camera's view screen. Still images were then captured and saved in a designated folder.

Image J

Image J software was used to abstract the measurement information from the photographs taken. Image J is an open source Java program inspired by NIH Image that is able to convert picture pixels into a distance measurement given a known distance for calibration. The photographs were then opened through the Image J program, from the program the images were then able to be zoomed in to visually assist the user in identifying small features. To calibrate the program the line feature was selected on the tool bar and a line was drawn from one micrometer stage marker to the next as shown below in Fig 56. Then the set scale option was selected to calibrate the program for distance measurement. From the present line drawn the program measured the amount of pixels between the start and finish of the line; the known distance of 1mm was entered in the known distance input box to effectively calibrate the distance for that image.

Once the program was calibrated for the present still image data was then collected and analyzed to determine the quality of different processes. Using the line

feature ten measurements of the structure's dimensions were taken as shown in Fig. 57 below and inserted into Excel for data analysis. The average and standard deviation σ was calculated from the values abstracted to determine the average distance and the distance uncertainty $U_{distance}$ by using Eq. 48 below where $t_{test\ 95\%}$ is the student t-test value for 95% confidence and N is the number of samples. This characterization method was used to determine over exposure, over development, under cutting, and effects of mold swelling within the electrolyte solution.

$$U_{distance} = t_{test\ 95\%} \frac{\sigma}{\sqrt{N}} \tag{48}$$

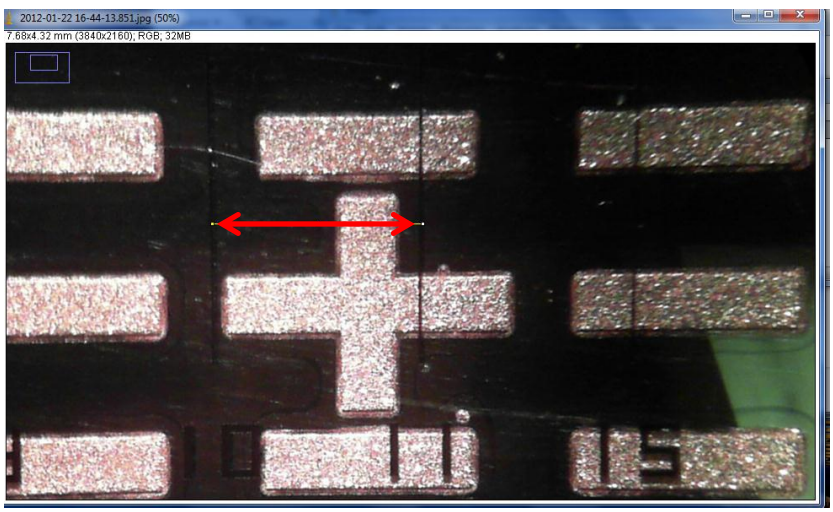

Figure 56. Abstracting known distance using Image J

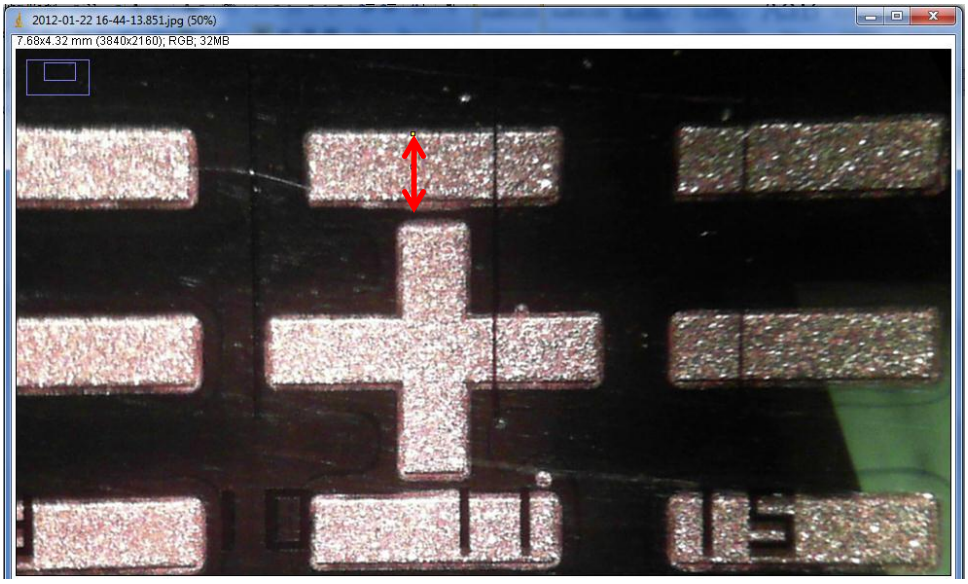

Figure 57. Abstracting Structure Dimensions using Image J.

Optical profilometer

The optical profilometer was used to determine more accurate information such as the mold or structure thickness as well as the profile and volume of the cavities. The Wyko NT9100 as shown below in Fig 58 is an optical profiling system able to perform repeatable sub-nanometer surface measurements. The optical profiler determines the depth by using a method using interference patterns by splitting a beam produced from LEDs to a reference mirror and another to the sample surface. If the sample surface and reference are in parallel only one fringe appears otherwise multiple dark and light bands will appear. The interference pattern is then imaged by a charged coupled device (CCD) camera and then processed by the software. (WYKO NT9100 Surface Profiler, setup and operation guide 2008)

The profilometer was used extensively to determine the profile shapes and more importantly the volumes of the crucible bowls as it is extremely important to determine the volume of substance that is being thermodynamically studied. The sample piece was

orthogonally placed upon the motorized stage of the optical profiler shown in Fig 58 and then positioned remotely under the optics. The magnification was set to 2.5X and set to vertical scanning interferometry (VSI). Using remote control knobs the object being measured was found and set in focus until fringes were visible in the viewing screen, then the tip/tilt knobs were adjusted until the fringes reduced to at least two large bands. The intensity of the light was also adjusted so that the patterns were not saturated as indicated by red areas in the viewing screen. Depending upon the size of what was being measured the scanning length was adjusted

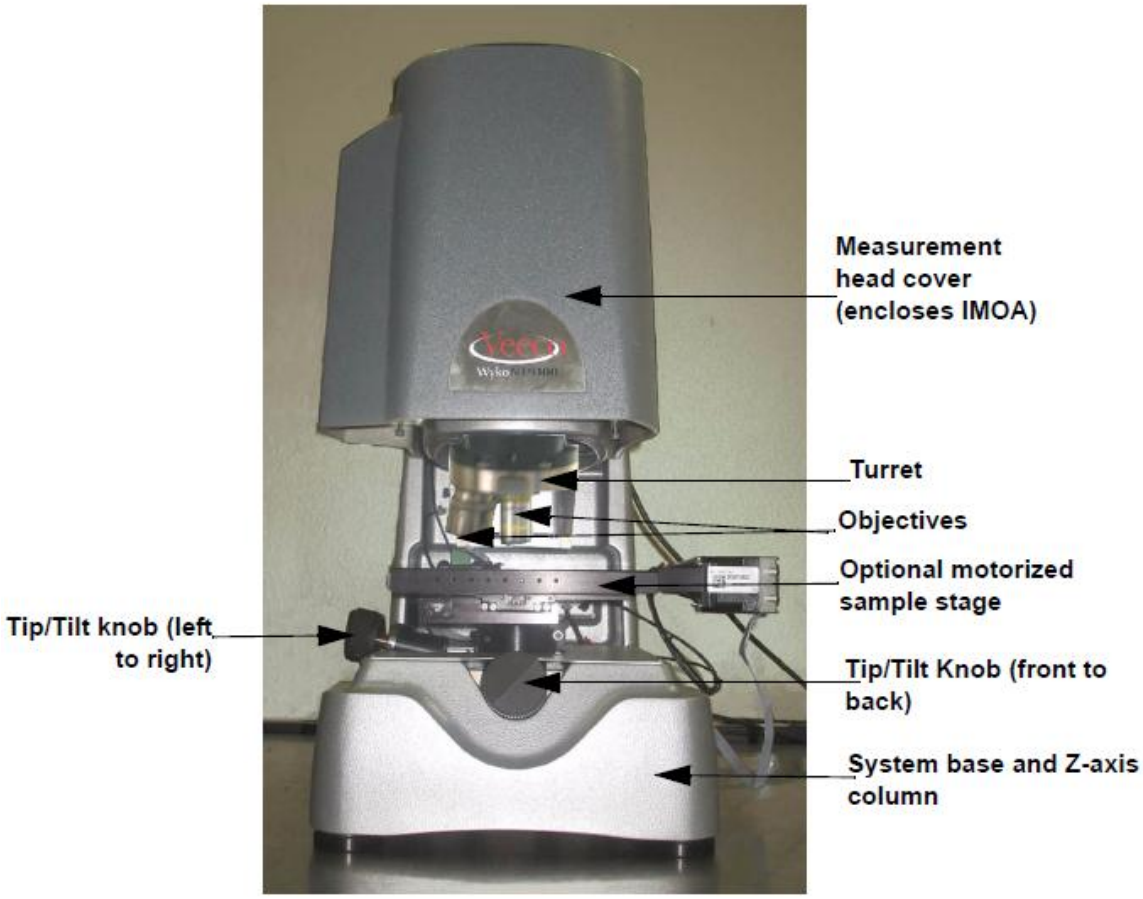

Figure 58. Wyko NT9100 optical profilometer (WYKO NT9100 Surface Profiler, setup and operation guide 2008)

Bowl Characterization

To determine the diameter, depth, aspect ratio, volume, and volume homogeneity of the crucibles required the use of the optical profilometer. A profile scan from both the longitude and latitude directions of the crucible were taken and then converted into numeric discrete x (length) and y (height) coordinates. That data was truncated to isolate the data points associated with the crucible shape only. Then the truncated data was split into two halves based upon the area's centroid to equally represent each side of the crucible shape. Then a Cartesian coordinate system was used where the length values were manipulated to be a function of height. Using a hybrid version of Simpson's rule and disc method as shown Eq. 49 below along with the semi-major $a(x)$ and semi-minor $b(x)$ axis of an ellipse and the step size h, the volume of the crucible $V_{crucible}$ was determined by revolving the halved crucible around the x axis. This was performed on both halves for both the longitude and latitude scans resulting in four different volume calculations that were later averaged along with determining their associated standard deviations. The homogeneity of the bowls was determined by evaluating the uncertainties of the four volume calculations using Eq. 49, the lower the uncertainty the more homogeneous the crucible. A Matlab script was written to perform all diameter, height, volume and uncertainties calculations; the code can be found in the appendix.

$$V_{crucible} = \pi \frac{h}{3}\left[a(x_0)b(x_0) + 2\sum_{j=1}^{\frac{n}{2}-1} a(x_{2j})b(x_{2j}) + 4\sum_{j=1}^{\frac{n}{2}} a(x_{2j-1})\, b(x_{2j-1}) + a(x_n)b(x_n)\right] \quad (49)$$

Volume homogeneity program

A brief description of how the program operates is warranted since it is the main tool used to analyze the data produced from the profilometer. Once the program is set to run it requires user input of the data points at which bowl starts and finishes for both the

X profile and Y profile. A 2-D plot is produced for both profiles and allows the user to select the beginning and end points of the crucible as shown in Fig 57. The program then calculates the diameters for both profiles and then determines which profile will be the major and minor axis of the ellipse for a more accurate volume calculation. The ratio of the diameters is also calculated and stored to be used in later calculations. Then the program determines where the profiles will be split to be revolved around. The program uses both the minimum depth and also the centroid of the crucible as the revolution axis. If the crucible is in a perfect bowl shape both revolution axis' positions will be the same. Then, the data is manipulated to position the axis positions on the origin (0,0) for easier data tracking. Next, depending upon which profile is being used for the current volume calculation, the program uses the diameter ratio to determine the corresponding major or minor axis for ellipse area calculation assuming the ratio is uniform throughout the depth of the crucible. The program then uses Eq. 49 to determine the volume for each half of both profiles for both the minimum and centroid based revolution axis. Finally, the script outputs the diameter, height, aspect ratio and volume calculations along with their associated standard deviations and uncertainties to an excel spread sheet for further analysis.

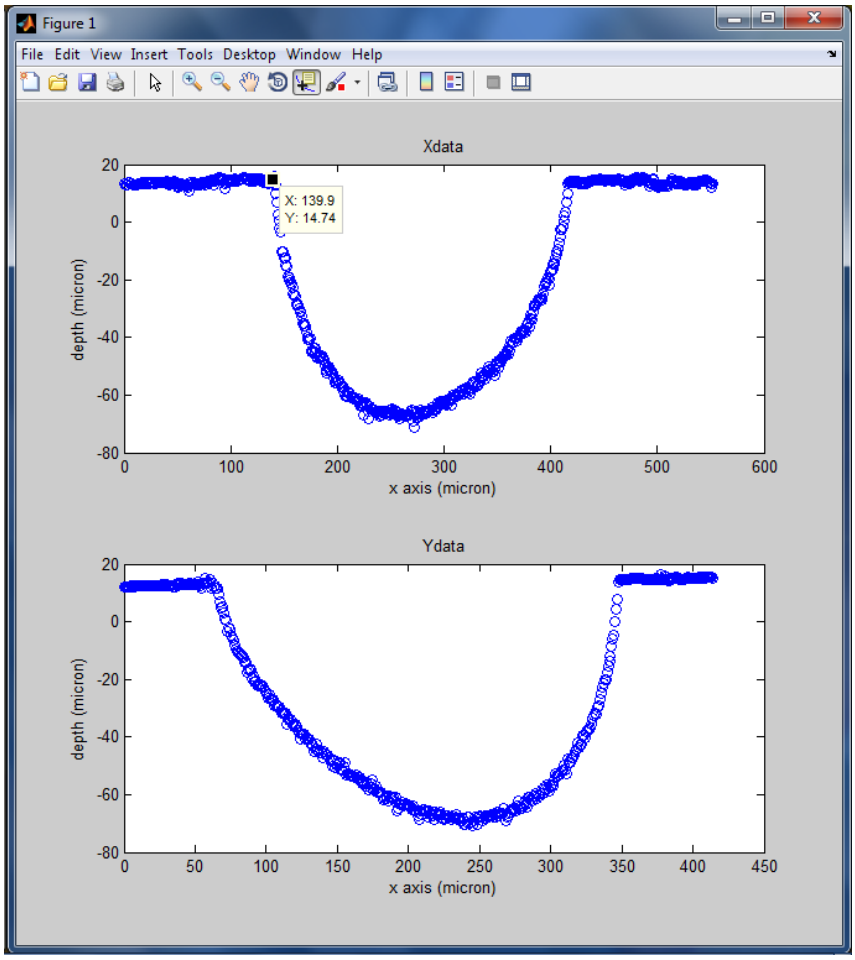

Figure 59. 2-D plot for both X and Y crucible profile data

Process Integration

Base structure

A plethora of steps and processes go into each manufacturing step of the bridge as the proceeding paragraphs have described, this section will solidify the integration of all the steps into an individual step approach. As discussed before the general process flow of constructing the DTA bridge is first growing the bridge base, then building up the cylinder, and finally etching a bowl shaped crucible into the cylinder. The first full process of developing the bridge base is illustrated in Fig. 60 where the process begins with the bare silicon substrate. The substrate is first sputtered with nickel and titanium

after a thorough RCA cleaning to remove any organic soil and oxidation layer that would cause poor adhesion. Then a 40 micron layer of resist was applied upon the substrate to allow sufficient height for electroplating growth as described in Table 17. The baking, exposing, and developing procedures were then implemented as described in Tables 10 & 11 above. The resistance probe and microscope was used to ensure that proper resist development has occurred for successful electroplating. Then, a 30 µm layer of copper was grown within the base micro-mold as described in Table 17 below along with a 20% duty cycle and 361 Hz pulse frequency. Finally, the resist was removed using RR41 or acetone to expose the grown copper to allow for fresh application of resist for future development of microcavities.

Table 17. Base Pulsed Electroplating Procedures

Height (µm)	Current Density (mA/cm^2)	Current Setting (A)	time (s)
1	15	0.012	181
19	10	0.0078	5170
10	5	0.0039	5442

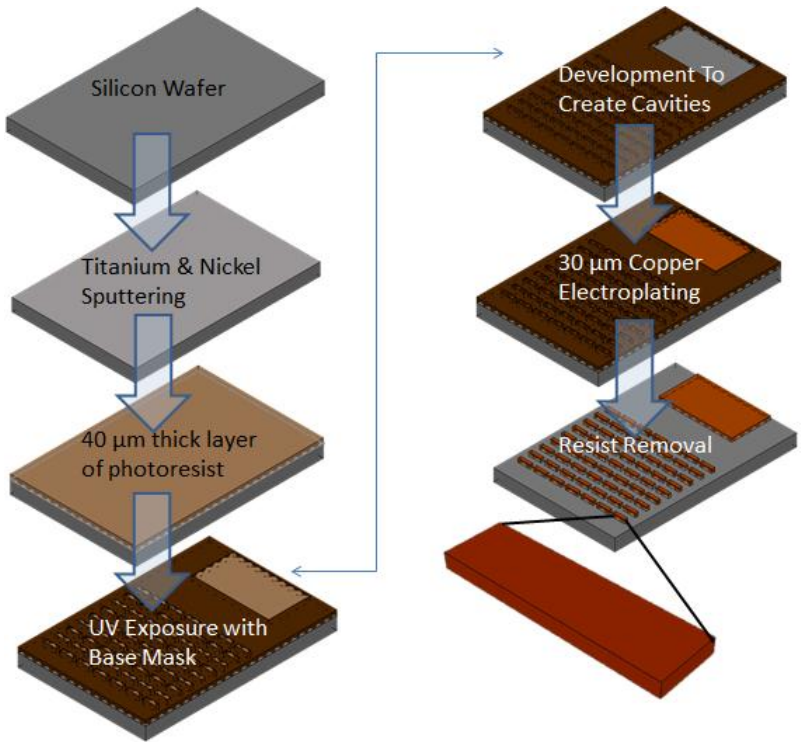

Figure 60. Bridge base construction

Cylinder

The next process of constructing the bridge is to grow a cylinder compatible for subsequent crucible etching in order to reduce thermal mass. The cylinder fabrication process is illustrated in Fig 61 below. The first step is to coat the wafer surface and base structures with 50 µm of photoresist as shown in Table 9; this will allow sufficient height for electroplating 45 µm of copper within the cavities. The baking, exposing, and developing procedures for proper buildup of 50 µm thick resist can be found in Tables 10 11 as discussed before. The preferred cylinder diameter size to be grown is typically 225 µm to allow for a 200 µm diameter crucible shape to be formed for easy thermocouple placement within the bowl. Subsequent copper growth upon the preceding bridge base structure has been proven difficult due to oxide formations and residual resist. Typically, a current strike of 200% of the original current value was used to sufficiently break down

the voltage potential within the cylinder cavities to establish an adequate base layer. The electroplating was performed with the prescribed settings displayed in Table 18 along with 20% duty cycle and 361 Hz D.C. pulsing. Once the electroplating process was complete the resist was removed to allow for fresh photoresist to be applied for the creation of an etching mask for the etching process.

Table 18. 225 micron crucible pulsed electroplating procedures

Height (µm)	Current Density (mA/cm^2)	Current Setting (A)	time (s)
1	20	0.0025	136
34	10	0.00125	9252
10	5	0.00062	5442

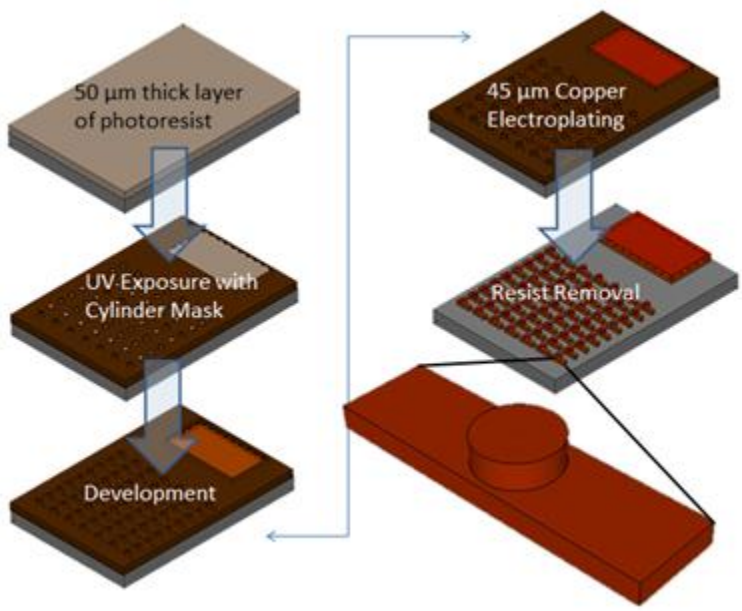

Figure 61. Cylinder fabrication process

Crucible

The final process steps of creating the micro-DTA is the creation of the bowl shaped crucibles using etching techniques as shown in Fig. 62. First, the mask was

developed by layering a 50 µm coat of photoresist over the wafer surface and existing bridge structures. The alignment of the etching masks were very crucial with low tolerance for error, thus an outsourced mask aligner was used in a different lab to perform the alignment and exposure of 5-10 µm of resist that was above the tops of the cylinder structures. After exposure, baking and development the wafer substrates was then placed in the etching station as described before for 20 minutes to create the desired bowls. The resist was then removed and the remaining structures were removed from the substrate by selectively stripping the thin nickel layer away.

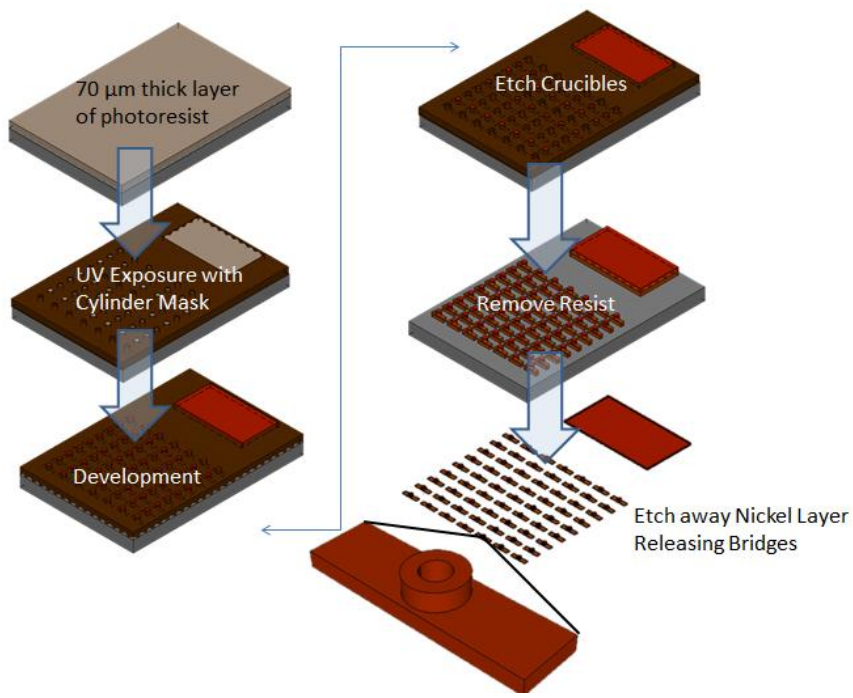

Figure 62. Crucible creating process

Manufacturing Conclusion

The fabrication process that was just discussed was a result from many different trials and methods to determine the correct combination of procedures to produce a workable bridge with crucible. The majority of the time and difficulty of the

manufacturing process was dedicated to determining the proper steps for developing the photoresist micro-mold cavities. The different procedures for developing the correct combination of processes are compiled and discussed in more detail in the results section. Although, the correct combination of processes has been determined to fabricate a workable bridge, they have not been optimized for tighter tolerances and quality of deposition. Such optimization procedures include baking temperatures and times along with development times for high tolerance geometry. The electroplating bath along with different current density profiles can also be optimized for more uniform and finer grain surface. Due to brevity of the research project these optimization procedures were left out and left as a high end first order approach for manufacturing of micro-bridges for biological DTA/DSC purposes.

Chapter 7. DTA Manufacturing Results

Introduction

The two topics of results being reported is the overall process results such as successful fabrication of steps and also the crucible construction and characterization. As stated before the majority of the time spent was determining the correct procedures to achieve successful, reliable, and repeatable micro-molds and electroplating. While the other portion of time was determining how to construct the crucible bowls for successful placement of the biological samples along with a thermocouple. The micro-mold and electrodeposition success was based upon numerous iterations of different combinations of procedures that were successful by other laboratories, companies, and even hobbyists. However, there seems to be a knowledge gap in peer reviewed literature concerning etching processes to create crucibles. The crucible bowls are a novel idea in the MEMS

manufacturing community and most procedures for construction and characterization of the crucibles were developed in house. The results reported will begin with process outcome and then concentrate on the characterization and development of the micro-crucibles.

Successful Fabrication Results

The results presented in this section will be in a troubleshooting format that was learned from the series of steps that led from failure and knowledge gained to eventually the successful combination of steps that were presented in the manufacturing process above. The justification for presenting the results in such an arrangement is to allow others who are new to large structure (>100µm) MEMS manufacturing to understand the process flow that was created and gain from the failures made. The initial fabrication process steps were initially conducted to learn the basics of the application of photoresist. Unfortunately, in the beginning process of the MEMS fabrication steps characterization data was not obtained from the camera, optical profiler or the SEM due to lack of resource knowledge. However, the results were recorded in spreadsheets and will be conveyed in the troubleshooting tables below.

Resist application

The first and the most crucial step in the micro-mold process is proper application of the photoresist upon the substrate. If the photoresist was not properly applied to the wafer then large deformations within the resist could result in subsequent problems in the latter steps. Displayed in Table 19 below are the recorded problems, the potential causes to the problems and recommended remedies. Insuring a properly clean wafer was the most problematic as it most usually caused vacancies or discontinuities within the resist during spin relaxation or soft baking. The resist does not adhere to hydrophobic surfaces

and if any organic contaminates were present on the wafer during resist application, the resist will evaporate or dissipate from that area causing voids within the resist layer. If voids occur the resist needed to be cleaned with acetone to remove the resist and repeat the cleaning and resist application process. If bubbles formed or the resist seemed to be uneven a simple relaxation of 1 hour proved to improve uniformity of the resist and to rid of air pockets that were trapped within the resist.

Table 19. Resist Application Trouble Shooting Table

Problems	Cause	Solution
Air Bubbles in resist	1. Faulty dispense tip 2. Air bubbles trapped in resist dispenser volume 3. Unproper dispense technique	**1.** Replace tip. **2.** Allow air bubbles in dispenser volume to surface and purge trapped air through tip. **3**. Insure resist flows smoothly from dispense tip to wafer surface **4.** Allow sufficent time for bubbles to outgas from dispensed resist on wafer by placement on level surface while covered to prevent evaporation
Uneven resist thickness and edge beading	1. Insufficient resist dispensed 2. resist dispensed off center 3. Resist thickness >30 microns	**1.** Dispense recommended volume amount per surface area. **2.** Insure concentration of dispensed resist is center relative to chuck **3.** Allow sufficent time for resist to reflow on wafer by placement on level surface while covered to prevent evaporation **4.** selectively remove wafer's edges to remove edge beading
Holes or discontinuities is resist	1. Organic contaminates 2. Oxide Layer 3. Surface debris 4. Water residue on wafer surface 5. Air bubbles	**1.** Clean with thorough rinsing using Acetone, Isoproply alcohol, and DI water to remove organic contaminates and surface debris **2.** Dip in pickeling solution for 60-90 seconds to remove oxide layer **3.** Pre-Bake of 100 C to deabsorb water within the wafer **4.** Refer to '*Air Bubbles*' solution

Development

Proper development was essential for the success of electroplating and was heavily dependent upon the preceding baking procedures. As shown in Table 20 below most remedies involve adjusting the soft or hard bake temperatures or times to prevent resist cracking and under etching which proved to be a daunting task. For an example,

one method was used to determine the correct PEB temperature to prevent cracking as shown in Fig 63 during development while holding all other variables constant. The conclusion of the proper PEB temperature was to lower the PEB to 65 °C which prevented cracking but enhanced under cutting of the resist as shown in Fig 64 and caused electroplating problems. The PEB temperature was too low to sufficiently remove the proper amount of resin and adequately crosslink the monomers. When the resist was submerged in the electrolyte solution a chemical reaction occurred between the acid and the resin. This reaction caused an oxidation layer on the surface of the cathode surface and increased the electrical resistance to ~1 Mohm which prevented further electroplating. After further research it was found that N_2 build up after exposure was a problem of thick resists which caused stress fractures if immediately exposed to a PEB (MicroChemicals 2010). A 24 hour post exposure relaxation time was implemented along with a temperature ramp during normal PEB to prevent cracking within the resist during development as shown in Fig 65.

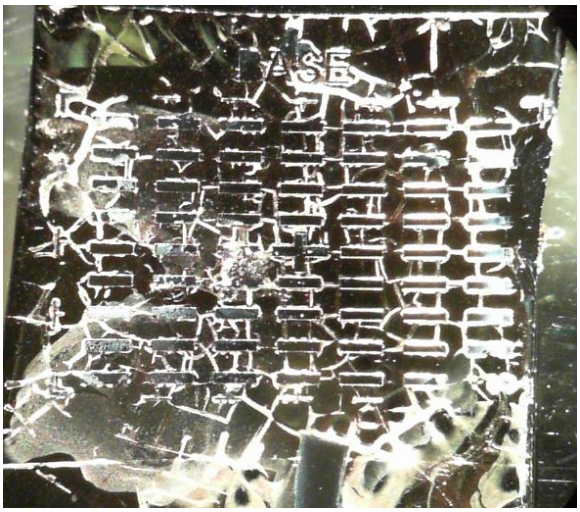

Figure 63. Resist cracking after development

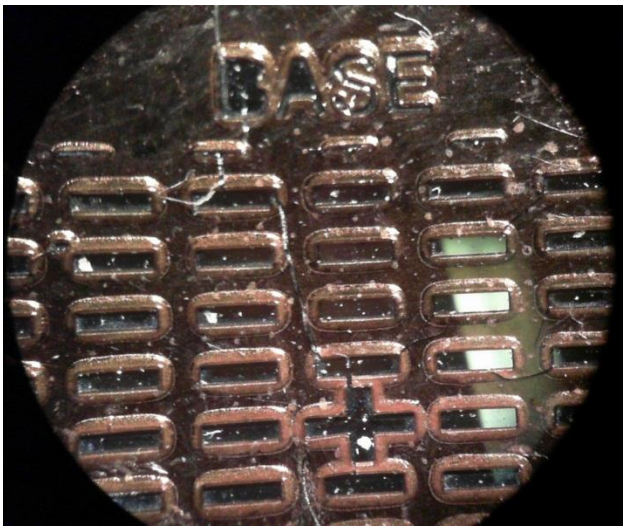

Figure 64. Undercutting of resist microcavities

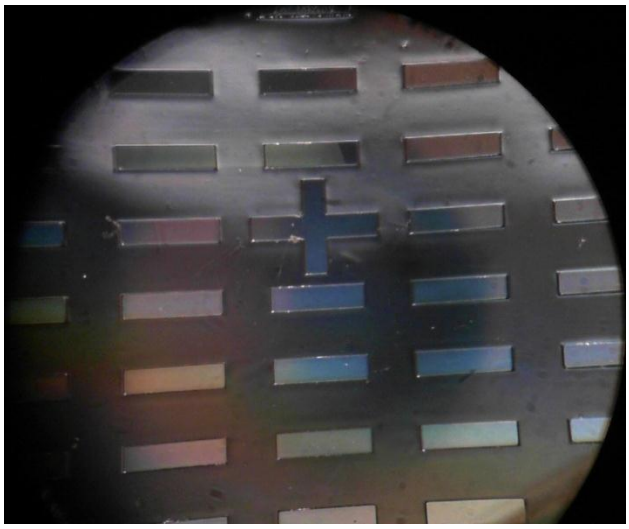

Figure 65. Proper development

Table 20. Development Troubleshooting Table

Problems	Cause	Solution
Resist Cracking	1. High thermal gradients during PEB 2. Excess N2 build up within resist post exposure 3. Temperature too high or too long during soft baking and/or PEB 4. Improper resist cool down	**1.**PEB Temperature Ramp **2.**Cover with petri dish to minimize temperature gradient. **3**. Sufficient relaxation time after exposure and before PEB **4.** Lessen temperature or time during soft baking and/or PEB **5**. Place resist in an insulated container to prevent rapid resist cool down
Under Etching/Unwanted Resist Removal (Dark Erosion)	1. Insufficient exposure dosage 2. Temperature too low or too short during softbaking and/or PEB 3. Temperature too high or too long during softbaking and/or PEB 4. Development too long 5. Photactive chemical inactive	**1.** Check exposure power output for proper dosage amount **2.** Measure resist thickness to insure proper input to exposure time equation **3.** Readjust temperatures or time during baking procedures to remove sufficient amount of resisn **4.** Readjust temperatures or time during baking procedures to reduce photactive chemical removal. **5.** Impliment check points during development to insure resist is removed before dark erosion occurs. **6.** Obtain fresh batch of photoresist.
Geometry Size Reduced	1. Exposure dosage too high. 2. Mask not in contact with resist	**1.** Check exposure power output for proper dosage amount **2.**Measure resist thickness to insure proper input to exposure time equation **3.** Insure correct photomask side is in contact with resist. **4.** Remove edge beading

Electroplating

Electroplating proved to be less problematic after the developing procedures were optimized to remove the proper amount of resin and to prevent cracking and under cutting. However, many times a small amount of resist resin was left and prevented proper plating adhesion to the cathode surface. The implementation of the electrical resistance probe improved adhesion results dramatically by determining the exact development times to adequately remove all resist within the micro-cavities. Often, it was found that many of the microcavities did not show signs of electrodeposition as shown in Fig. 66 throughout the process even though the resistivity of the cavities was within tolerable ranges as shown in Fig. 67. The resulting electroplating failure was partially due to the double layer that grew during standard D.C. plating causing an increase in

electrical potential along the cathode. Voltage potential required to sufficiently drive the desired electrical current from the anode to the cathode during electroplating was a good indicator of deposition results. If the voltage potential increased during electroplating as shown in Fig. 68 poor deposition results often occurred as explained earlier. Execution of pulsed D.C. plating proved to enhance uniformity and adequate material filling within all of the cavities as shown in Fig 69. Improved electrodeposition by pulsed plating was due to the sufficient discharge of the electrical double layer and the reduction of the ion concentration gradient within the solution. A troubleshooting table was constructed in Table 21 below to show remedies to problems encountered with electroplating.

Electroplating Cylinders

Electroplating the crucible cylinders proved to be more problematic than the base due to the relatively high electrical resistances of the base post plating. The high resistances minimized the current density within the micro-cavities, which slowed down the deposition times significantly. High current gradients were instead along the edges of the wafer where the nickel plating was slightly exposed and electrical resistances were low. As a result, significant plating occurred on the edges instead of inside the cylinder cavities. To counter edge deposition, the edges were coated with latex paint to essentially create a higher resistance circuit along the edges than the cavities to force deposition back into the cavities. This simple solution proved to be effective in growing cylinders as large as 80 microns in height.

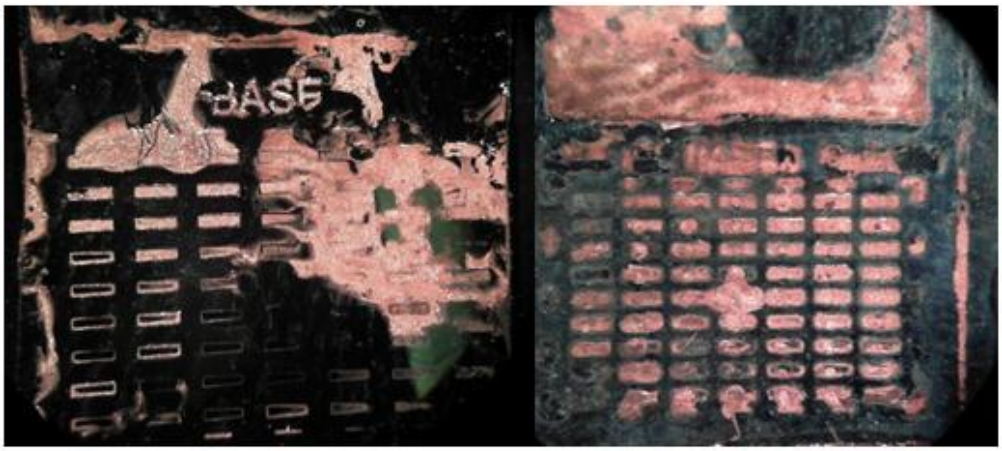

Figure 66. Poor deposition results during standard D.C. plating

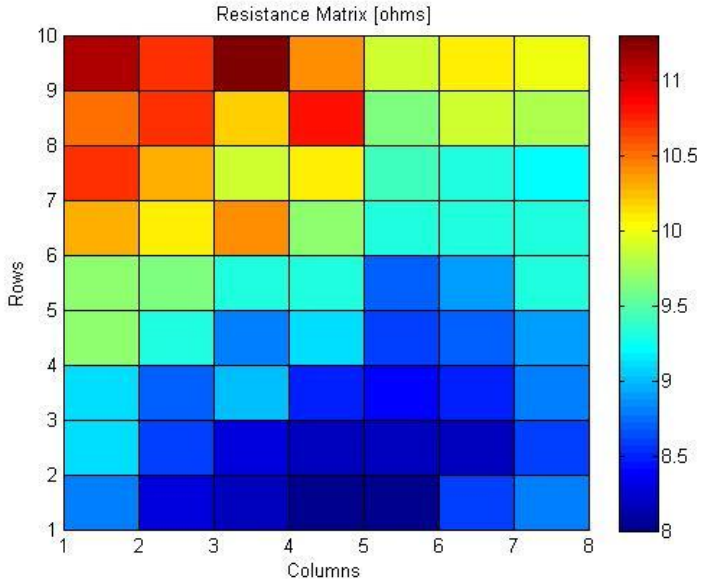

Figure 67. Electrical resistance matrix of fully developed cavities

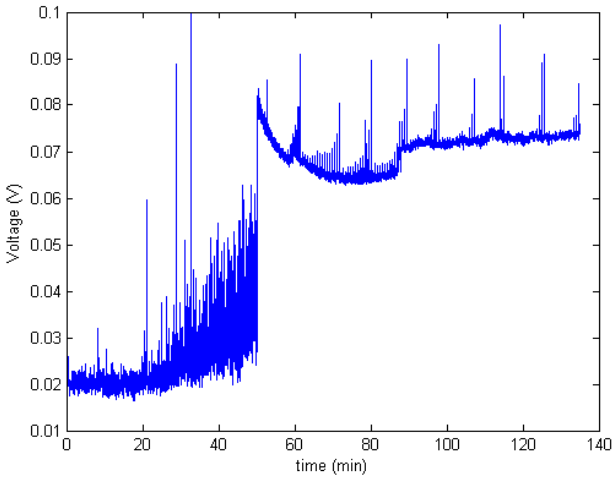

Figure 68. Electrodeposition voltage potential increased dramatically around 50 min indicating poor results

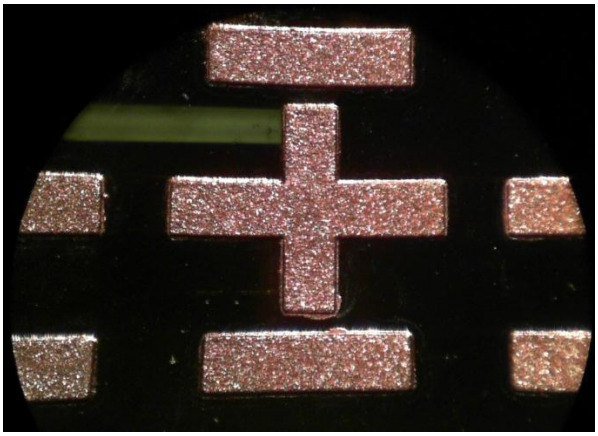

Figure 69. Improved deposition results as an outcome from pulsed D.C. electrodeposition.

Table 21. Electroplating Trouble Shooting Table

Problems	Cause	Solution
No Plating or poor adhesion	1. Thin layer of resist exists 2. Plating surface oxidized 3. Resist resin reacting with electroplating solution. 4. Voltage potential too high 5. Cavities not wetted	**1.**Insure proper development using resistance testing method **2.**Dip substrate in pickeling solution for 60-90 seconds. **3**. Insure proper temperatures and times for baking procedures to remove adequate amount of resin. **4.** Check pH in bath **5.** Impliment plating strike to lower voltage potential **6.** Fill cavities with DI water using pressurized stream from squirt bottle.
Uneven Material Deposit	1. Current density too high 2. DC pulsing incorrect 3. Not all areas plating 4. Improper distance between cathode and anode 5. pH in bath too high 6. insufficient solution agitation	**1.** Insure current density is between 0.01 and 0.03 A/cm^2 **2.** Check duty cycle and frequency settings are correct. **3.** Refer to '*No Plating*' solutions to insure all areas are being platted to insure even wafer current gradients. **4.** Insure distance between cathode and anode is more 3". **5.** Insure pH is <6 **6.** check stir bar speed.
Pitted or rough surface	1. Impurities in bath solution 2. Current density too high 3. Surface impurities	**1.** Filter bath solution to remove impurities **2.** Lower current density and insure current density is between 0.01 and 0.03 A/cm^2 **3.** Clean surface using mild hydrogen peroxide solution and DI rinse.

Electroplating Study

To confirm the validity of the analytical electroplating thickness correlation stated in Eq. 46 an electroplating study was implemented. Three separate square nickel coated wafer fragments were used to validate the linearity and accuracy of Eq. 46. Each fragment was measured to determine its associated area to determine the correct dosage of applied current to achieve the desired current density of 0.07 (A/in^2). Three electroplating trials were conducted with three different times 35, 60, and 90 minutes. The thicknesses were analyzed and measured using a scanning electron microscope to produce thickness measurements presented in Table 22 below. The measured results

agree with the predicted values produced from Eq. 21 and was determined to follow a linear trend with an R squared value of 0.9939.

Table 22. Electroplating Thickness Vs. Time Study

Current Density (A/in^2)	Time (min)	Predicted thickness (µm)	Measured Thickness (µm)	Relative Error
0.07	35	7.41	8.62	16.35%
0.07	60	14.35	14.97	4.31%
0.07	90	21.53	20.77	3.53%

Crucible Fabrication Results

This section will concentrate upon the development and characterization of the micro bowl shaped crucibles. The methods towards fabrication that are described are not borrowed from past literature instead; they were originated from within the laboratory. To understand the homogeneity and rate of etching an etching study was performed on copper foils using photoresist masks to determine the proper etching times and etching mask sizes. The studies determined how the etching responded to varying mask sizes and etching times.

Etching Fixture

Previous trials of performing the etching study did not utilize the etching fixture as described in the procedures section. Earlier etching experiments involved simply placing the test piece in a bath of copper etchant with the aerator hose being positioned near the experiment piece and secured in place with tape to run the trial. The crucible characterization results varied throughout different trials using the earlier method. It was then decided to develop a fixture that will secure the aerator hose in place at a predetermined distance away from the sample piece. A student t-test study was

performed to confirm that the results improved while using the fixture. The tests involved two separate 200 micron diameter masked samples and were both etched for 20 minutes, 21 different samples were analyzed and the results are displayed in Table 23 below. With a 95% confidence the fixture increased the volume and diameter while improving the AR, improved the crucible homogeneity by lowering the uncertainty, and also improved the eccentricity. The results confirmed that implementing the fixture for future trials was needed for improved studies.

Table 23. Fixture vs No Fixture Etching Experiment

	Fixture	No Fixture	P Value
Volume (centroid) (Nano-Liter)	2.88	1.88	9.19E-06
Standard Deviation (Nano-Liter)	0.05	0.10	3.04E-02
T-Test Uncertainty (Nano-Liter)	0.07	0.16	3.04E-02
Eccentricity	0.17	0.37	1.19E-04
Diameter µm	280.41	244.17	6.94E-05
Depth µm	64.19	65.60	8.08E-01
Correct Aspect Ratio	1.54	0.56	5.80E-07

Mask Diameter Study

It was hypothesized that keeping the etching time constant and varying the mask size would vary the crucible's aspect ratio by varying the restriction of the rate of etching solution agitation within the cavity. A study involved mask sizes that are within the range of the desired crucible size for this paper. The mask sizes chosen were 140, 170, and 200 µm diameter. Each masked sample piece was etched for 20 minutes using the etching fixture. A total of 30 samples were measured and analyzed to produce Table 24 below. The data indicates that with 95% confidence that the depth does not vary with mask size. However, for the 200 micron mask the etched radius does vary significantly from that of the 140 and 170 micron mask sizes by 12 microns. The study concludes that there exists a

diameter limit between 170 and 200 microns that improves the aspect ratio and also agrees with the previously stated hypothesis.

Table 24. Mask Diameter Etching Study

	140	170	200		140Vs170	170vs200	200vs140
Depth µm	55.93	63.92	64.19	**height p-value**	0.21	0.96	0.15
Radius µm	32.69	32.13	44.70	**radius p-value**	0.85	3.60E-03	6.71E-05

Etching Rate Study

A study was conducted to determine the etching rate of the copper etching solution by holding the mask size constant while varying the etching times. Through past experiments it was found that bowls were sufficiently etched at 20 minutes. It was hypothesized that the etching rate was linear due to the mask diameter, aerator hose distance, and solution bath temperature being constant while time being the only variable. The experimental test plan was based upon the hypothesis and designed to only use three different test samples with three different times to create a sufficient trend. Three different 200 micron masked samples were etched 15, 20, and 25 minutes with 28 different crucible samples being analyzed to determine the hypothesized linear etching rate. The etched radius did not significantly change with varying etching times, however the depth varied linearly with an R squared value of 0.9959 with time as shown in Table 25 below. The etching rate calculated was 1.8 microns per minute, which was an order of magnitude lower than what Jian predicted due to the restricted agitation within the micro-cavities. (Jain, et al. 1998**)**

Table 25. Etching Rate Study

	15min	20 min	25 min
Depth µm	55.73	64.19	73.04
radius µm	43.15	44.70	44.23

Final Bridge with Crucible

Once all fabrication techniques and procedures were determined through trial and experimentation a final bridge design was concluded and manufactured to assist in obtaining crucial thermodynamic data from biological samples. The final design specifications of the bridge were 50x300x1000 micron base with 50x300 micron cylinder and 60x280 micron bowl shaped crucible. The base was manufactured to be larger than stated in the procedures section to account for unknown handling problems. The crucible's aspect ratio was proposed to allow for the thermocouple bead to be in good thermal contact with the crucible bottom, otherwise not easily achievable with higher aspect ratios.

Optical profilometry images of the bridge with crucible were produced and illustrated below in Figs (70-71). The final manufactured measurement results from Image J and the optical profilometer were compared with the design specifications as shown in Table 26. The electroplated thicknesses of the base and cylinder exceeded the designed specifications by 34% and 58%. A potential cause for this error was 8 cavities in the upper region of the wafer did not plate well due to residual resist or oxidation within their cavities causing higher current densities to be directed towards the other voids. The higher current densities thus allowed for higher deposition rates causing an increase in plated thickness. The etched crucible was 24 microns shallower than what was designed. It is believed that the mask thickness for the cylinders greatly exceeded the

mask thickness used during the etching studies. This increase in thickness created a more restrictive passageway for proper etching solution agitation within the cavities thus reducing the etching rate. Also, the cylinder on the base was slightly off centered due to the problematic nature of hand alignment and settle variations during the mask vacuum process. However, the base and cylinder widths and lengths correlated closely with their associated design specifications. This was achieved only after determining the correct procedures for the development of micro-cavities. Also, the bowl-shaped crucible has a relatively high volume to diameter sensitivity (6745 $\mu m^3/\mu m$) allowing for improved 2-D volume abstractions. Overall, the final micro-DTA bridge manufacturing process was a success in achieving a quality bowl-shaped crucible and base for future biological calorimetric experiments and analysis.

Table 26. Geometry Characterization of Final Bridge

	Measured Mean	T-Test Uncertainty	Designed	Mean Relative Error
Base Width µm	336.14	4.50	300	12.05%
Base Length µm	1051.52	2.09	1000	5.15%
Base Height µm	67.32	1.45	50	34.63%
Cylinder Diameter µm	300.34	4.24	300	0.11%
Cylinder Height µm	79.39	0.76	50	58.78%
Crucible Diameter µm	249.67	4.02	280	10.83%
Crucible Depth µm	36.85	6.44	60	38.58%
Crucible Volume (Nano-Liter)	0.85	NA	1	15.00%
Crucible Eccentricity	0.30	NA	0	NA

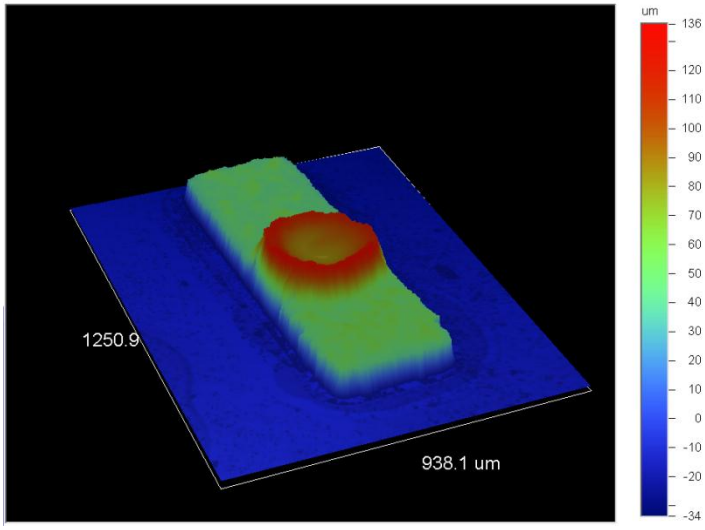

Figure 70. Side view of final micro-DTA bridge with crucible

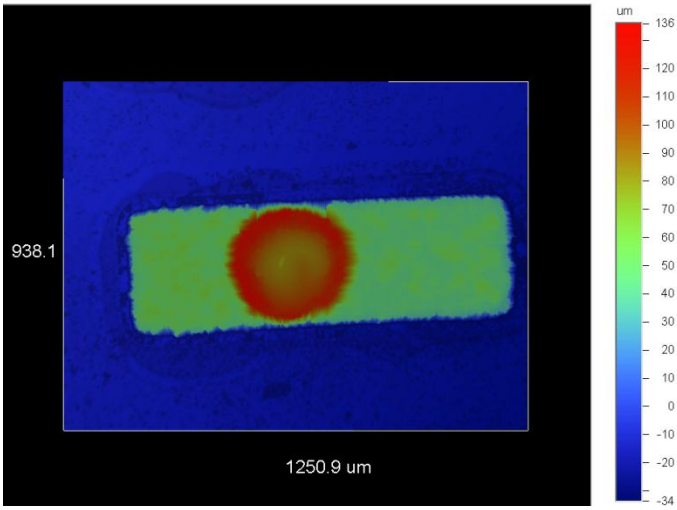

Figure 71. Top view of final micro-DTA bridge with crucible.

Micro-DTA Manufacturing Conclusion

A proof of concept micro-DTA bridge has been successfully manufactured for purposes of abstracting thermodynamic properties from biological samples such as oocyte cells. There are process areas of interest to improve the micro-DTA bridge manufacturing results such as electroplating and etching. The electroplating solution chemistry can be altered to allow for smaller grain sizes to be deposited, improving the

surface quality of the bridge and to also allow a more uniform deposition throughout the cavities for mass production of bridges. Various designs for etching stations can be implemented to increase aerated agitation and temperature uniformity to improve the overall homogeneity and aspect ratio of the bowl shaped crucibles.

Future designs of the micro-DTA bridge include employing different temperature measurement schemes to alleviate the need for a mass-difference base-line method. An intrinsic thermocouple device idea has been conceived by micro-welding a 0.0005" constantan wire into the copper crucible creating a type-T junction for a different approach to temperature measurement. The intrinsic thermocouple approach cannot be implemented with a DSC design due to external voltages used to alter the bridge temperature will interfere with the temperature measurement voltages. However, implementation of an isolated resistance temperature device into the bridge could be an alternate approach for a DSC scheme. Presently, the methods described in this paper have been proven to be successful in the manufacturing of a highly sensitive micro-bridge with built in micro-crucible for the containment of biological samples to perform successful scanning calorimeter measurements.

Works Cited

Allen, James J. . *Microelectomechanical system design.* New York: Taylor & Francis Group , 2005.

"Baking Steps in Photoresists Processing." *MicroChemical.* 01 27, 2010. www.microchemicals.eu/technical_information (accessed 11 23, 2011).

Bornside, D., C Macosko, and L. Scriven. "On the Modelling of Spin Coating ." *Journal of Imaging Technology* , 1987: 122.

Bottner, H. , et al. "Nanocalorimetric Devices with thermoelectric PECVD Thin Film Layers for the analysis of Biological Phase Transistions." *22nd International Conference on Thermoelectrics .* 2003 .

Carcano, G., M. Ceriani, and F. Soglio. "Spin Coating with High Viscosity Photoresit on Square Substrates." *Hybrit Circuits*, 1993.

Chandrasekar, M. S., and Malathy Pushpavanam. "Pulse and Pulse reverse plating-Conceptual, advantages and applications ." *Electrochimica Acta*, 2008: 3313-3322.

Cohen-Addad, J. P, A. Prunelet, J. P. Bazile, A. Buda, and M. Thomas. "rylonitrile–sodium methallylsulfonate copolymer. DSC approach." *Biomaterials* , 2003: 173-179.

"Columbia University Clean Room ." *CEPSR Clearn Room.* 2009. http://www.clean.cise.columbia.edu/ (accessed 11 21, 2011).

Devaraj, G. "Pulse Plating ." *Materials Chemistry and physics*, 1990: 439-461.

Diller, K. R., and S. Yuan. "An Optical Differential Scanning Calorimeter Cryomicroscope." *Journal of Microscopy*, 2005: 85-93.

Dukovic, John O. , H. Gerisher, and C. W. Tobias. "Current Distrubtion and Shape Change in Electrodeposition of Thin Films for Microelectronic Fabrication ." *Advances in Electrochemical Science and Engineering* , 1994.

Faulkner, L.,L. *MicroElectroMechanical System Design.* Columbus: Taylor & Francis Group, LLC, 2005.

Flack, Warren W., Ha-Ai Nguyen, and Elliott Capsuto. "Characterization of an Ultra-Thick Positive Photoresist for Electroplating Applications." *SPIE*, 2003: 1-15.

Flack, Warren W., Ha-Al Nguyen, Elliott Capsuto, and Kelly Abreau. "Characterization of 100 Micron Thick Positive Photoresist on 300 mm Wafers." *SPIE*, 2005: 1-12.

Franssila, Sami. *Introduction to Micro-Fabrication .* West Sussex: John Wiley & Sons , 2004.

Gad-el-Hak, Mohamed . *MEMS Design and Fabrication 2nd edition.* Boca Raton, FL: Taylor and Francis Group, LLC, 2006.

Gao, Dayong, and J. K. Crister. "Mechanisms of Cryoinjury in Living Cells." n.d.

Guttman, C. M. , and J. H. Flynn. "On the Drawing of the Base Line for differential scanning calorimetric calculation of heats of transition ." n.d.

Han, Bumsoo, Ramachandra V. Devireddy, and John C. Bischof. "Phase change behavior of biomedically relevant solutions." *ASME International Mechanical Engineering Congress & Exposition.* New Orleans: IMECE, 2002.

Han, Xu, and John K. Crister. "Measurement of the size of intracellular ice crystals in mouse oocytes using a melting point depression method and the influence of intracellular solute concentrations ." *Crybiology* , 2009: 302-307.

Jain, Cai, Ma Jusheng, Wang Gangqiang, and Tang Xiangyun. "Effects on Etching Rates of Copper In Ferric Chloride Solutions." *IEMT/IMC.* 1998. 144-148.

Jones, Scotten W. . "Photolithography." In *Silicon Integrated Circuit Process Technology*, 1-112. 2000.

Judy, W Jack. "Microelectromechanical (MEMS): fabrication applications." *Instute of Physics Publishing* , 2001: 19.

Kanani, Nasser. *Electroplating: basic principles, processes and practice.* Amsterdam : Elsevier, 2004.

Karimanal, Kamal V. , Michael J. Ellsworth, Jr. , and Gamal Refai-Ahmed. "A numerical technique for modeling thermoelectric cooler with temperature controller for steady state CFD applications." *IMECE.* Washington D.C. , 2003.

Kelly, J.J., and S.H. Goods. *LIGA-Based Microsystem Manufacturing: The Electrochemistry of Through-Mold Deposition and Material Properties.* Yorktown Neights: Electrochemistry at the Nanoscale , 2005.

Kern, Werner. "The Evolution of Silicon Wafer Cleaning Technology." *Journal Electrochem. Soc.* June 1990.

Klancnik, G. , J. Medved, and P. Mrvar. "Differential thermal analysis (DTA) and differential scanning calorimetry (DSC) as a method of material investigation." *RMZ-Materials and Geoenvironment,* , 2010: 127-142.

Lee, Hong Joo, Heiner Strathmann, and Seung Hyeon Moon. "Determination of the limiting current density in electrodialysis desalination as a emperical function of linear velocity ." *Elsevier*, 2005: 1-18.

Lee, Hong Joo, Heiner Strathmann, and Seung Hyeon Moon. "Determination of the limiting current density in electrodialysis desalination as an empirical function of linear velocity." *Desalination* , 2006: 43-50.

Li, W. H., J. H. Ye, and S.F. Y. Li. "Electrochemical deposition of Copper on patterned Cu/Ta(N)/Si)2 surfaces for super filling of sub-micron features." *Journal of Applied Electrochemistry* , 2001: 1395-1397.

Lobontiu, Nicolae, and Ephrahim Garcia. *Mechanics of Microelectromechanical Systems.* Moscow: Kluwer Academic Publishers, 2005.

Madou, Marc. *Fundamentals of Microfabrication the science of miniaturization .* Boca Raton: CRC Press LLC, 2002.

Maluf, Nadim, and Kirt Williams. *An Introduction to Microelectromechanical systems engineering .* Norwood, MA: Artech House, Inc. , 2004.

Mazieres, C. "Micro and Semi-Micro Differential Thermal Analysis." *Ecole Nationale Superieure de Chimie*, n.d.

McGrath, J. J. "A Microscopic Diffusion chamber for Determination of the Equilibrium and Non-Equilibrium osmotic Response of Individual Cells." *Journal of Microscopy*, 1985: 249-263.

Mechanisms behind the Lotus effect. Hong Kong , n.d.

MicroChemicals. "Baking Steps in Photoresists Processing." 1 27, 2010.

Microelectromechanical Systems. Washington, D.C. : National Academy Press, 1997.

"Microelectronmechanical Systems: Advanced Materials and Fabrication Methods." Washington D.C. : The National Academy of Sciences, 1997. 1-75.

Muldrew, Ken, and Locksley E. McGann. "Mechanisms of Intracellular Ice Formation." March 1990: 525-532.

Muldrew, Ken, and Locksley McGann. "The Osmostic Rupture Hypothesis of Intracellular Freezing Injury ." *Biophysical Journal* , 1994: 532-541.

Osero, Norman M. "Overview of pulse plating." *Plating and surface finishing* , 1986: 20-22.

Patankar, Suhas V. . *Numerical Heat Transfer and Fluid Flow .* Taylor & Francis , 1980.

Paunovic, M., and M. Schlesinger. *Fundamentals of Electrochemical Depositon .* New York: Wiley, 1998.

Pepin, Ben. "Fabrication of a micro-DSC Device using MEMS Techniques." Columbia, Mo , 2010.

Pope, M. I. , and M. D. Judd. *Differential Thermal Analysis, A guide to the technique and its applications .* n.d.

Puippe, J. Cl. "Influence of charge and discharge of electric double layer in pulse plating ." *Journal of Applied Electrochemistry*, 1980: 775-784.

Schlesinger, M., and M. Paunovic. *Modern Electroplating (4th edition).* New York: Wiley, 2000.

Schlesinger, Mordechay. *Modern Electroplatng .* Habaken, New Jersey: 2010, 2010.

Senesac, L. R. , D. Yi, A. Greve, J. H. Hales, and Z. J. Davis. "Micro-differential thermal analysis detection of adsorbed explosive molecules using microfabricated bridges ." n.d.

Simon, P. , and Z. Cibulkova. "Measurement of Heat Capacity by Differential Scanning Calorimetry." n.d.

Snodgrass, T, and C. Newquist. "Extrusion Coating of Polymers for Nex tGeneration, Large Area FPD Manufacturing." *SID*, 1994.

Solbrekken, Gary L., William G. Zhao, Steven F. Mullen, James D. Benson, X Han, and John K. Crister. "Development of a Micro-Scale Differential Scanning Calorimeter for Single Cell Measurements." *ASME-JSME Thermal Engineering Summer Heat Transfer Conference .* Vancouver: ASME, 2007. 8.

Standard Practice for Preparation of Copper and Copper-Base Alloys for electroplating and conversion coatings . ASTM, 2008.

"What is MEMS." *MEMSnet.* n.d. http://www.memsnet.org (accessed November 9, 2011).

Woods, Erik J. , James D. Benson, Yuksel Agca, and John K Crister. "Fundamental crybiology of reproductive cells and tissues ." *Cryobiology* , 2004: 146-156.

"WYKO NT9100 Surface Profiler, setup and operation guide ." Tucson , Arizona : Veeco Instruments Inc, 2008.

Yang, H, Reiyu Chein, T. H. Tsai, J. C. Chang, and J. C. Wu. "High-aspect-ratio microstructural posts electroforming modeling and fabrication in LIGA process." *Microsyst Technol*, 2006: 187-192.

Yang, J. , and C. Roy. "Using DTA to quantitavely determine enthalpy change over a wide temperature range by the "mass-difference baseline method" ." *Thermochimica Acta*, 1999.

Yang, R, and W Wang. "Fabrication of out-of-plane SU-8 refractive microlens using directly lithography method." SPIE 5346, 2004. 151-159.

Youssef, S., J Podlecki, R. A. Asmar, B. Sorli, C. Oliver, and A. Foucaran. "MEMS Scanning Calorimeter with Serpentine-Shaped Platinum Resistors for Characterizations of Microsamples." *Microelectrictromechanical systems*, 2009.

Yu, M. , E. A. Olson, M. Zhang, F. Schiettekatte, Z. Zhang, and L. H. Allen. "Ultrasensitive, fast, thin-film DSC." *Review of Scientific Instruments*, n.d.

Zhang, J., N. W. Botterill, C. J. Roberts, and D. M. Grant. "Micro-thermal analysis of NiTi shape memory allow thin films." *Thermochimica Acta*, 2003.

Zhang, Xi, et al. "Pulse Electroplating of Copper Film." *Journal of Nanoscience and Nanotechnology*, 2008: 2568-2574.

Zhao, William G. , Gary L. Solbrekken, Steven F. Mullen, James D. Benson, Xu Han, and John K. Crister. "Development of A Micro-Scale Differential Scanning Calorimeter for Single Cell Measurements." Vancouver, British Columbia : ASME , 2007.

Appendix:

Numeric Model

```
%% 1-D multi-layer conduction transient control volume code
% with emphasis on thermoelectric heating and cooling
% Written by Logan Compton
% 2-16-2012

% Code pulls existing electrical current data from experimental results
and
% models the temperature of the top node of the thermal electric module
% which consists of layers of ceramic alumnia, alumnium, bismuth
telluride,
% alumnium and ceramic alumnia. Applys peltier heating and cooling at
% alumnium and bisumth telluride interfaces along with joule heating
within
% the bismuth telluride piece. Constant boundary condition on the
bottom end
% node to represent cold block and heat transfer coefficient on the top
% node to represent natural convection.


clear all
clc
tic
%% Build model by adding thermodynamic properties into array

%% layer properties
cvl=1*10e-9; %control volume size (m)
cv2=8*10e-7;
cv3=2*10e-7;
cv4=3*10e-8;
cv5=6*10e-9;

% Layering Scheme: ceramic, copper, bismuth telluride, copper, ceramic,
copper, glass,
% bismuth telluride, copper, water, Type E themoelectric

k=[35,223,1.48,223,35,1.4,401,1.2,401,569e-3,(21.9+16.7)];
%(W/m)Thermal conductivity of layers (1,2,3..)
rho=[3750,8800,7700,8800,3750,2225,8960,7700,8960,1000,8730];  %
(kg/m^3)density of layers (1,2,3..)
cp=[775,420,122,420,775,835,390,122,390,4217,(4.07e-1+3.984e-1)]; %
(J/kg*K)heat capacity of layers (1,2,3..)
len=[0.0006858,0.0004318,0.00127,0.0004318,0.0006858,0.0001524,0.000152
4,500e-6,30e-6,15e-6,25e-6]; %(m)length of layers (1,2,3..)  %(m)length
of layers (1,2,3..)

 nodes=[500,600,1200,600,500,500,500,800,600,600,600];%mesh independent
volume


%% Experimental Model Properties
  Jo=xlsread('initcond','E2:E1300'); % retreives current profile
```

```
  t=xlsread('initcond','A2:A1300'); % retreives time profile
  Tprof=xlsread('initcond','G2:G1300'); % retreives Temperature profile
of experimental results
  T_init=xlsread('Tinit','A1:A7004'); % retreives intial temperature
distrubtion within the model

  %% Specify Time step
  Dt=0.05; % constant time step [s]

 %%%%%%%%%%%%%%%%%%%%%calculation ensure s even time
step%%%%%%%%%%%%%%%%%%%%%%
  t1=diff(t);% data time step [s]
  ts=round(t1/Dt);  % number of timing loops per data time step
  n_time=sum(ts);   % total number of timing loops per data time step.

%%%%%%%%%%%%%%%%%%%%%%%%%%%%%%%%%%%%%%%%%%%%%%%%%%%%%%%%%%%%%%%%%%%%%%%%%%%%%%%
%%%%%%

 %% Specify Initial Temperature
  T_init = 273-15; % initial temperature */
  J=(Jo./(2.17e-6))';%* electric current density in [A/m2]
 rho_e = [(2*8.82e-6),1.68e-8];%/* electric resistivity in [ohm-m] */
 %rho_e = [(1.026e-3),1.68e-8];
 alpha =0.378*1.92e-4; %/* Seebeck coefficient [V/K] */

%% Internal Heat generation & Boundary Conditions
spa=[0,0,0,0,0,0,0,0,0,0,0];
sca=[0,0,0,0,0,0,0,0,0,0,0];
layerbc=[0,1,-1,0,0,0,0,0,0,0];% applies peltier cooling/heating at
layer interfaces -1=cooling 1=heating
control = [0,1]; %/* control should be 0 if a temperature BC is used
and 1 otherwise */
T_bc =[251,0]; %Temperature Boundary Conditions
q = [0,0]; % conduction B.C.
h = [0,0.5]; % heat transfer coefficient for convection B.C.
T_inf = [0,288]; % ambient air temperature for convection B.C.

%% Natural convection information
L=(1.95e-6)/(0.0056); %charcteristic length (A/P)
Beta=1/T_inf(2); %
Nav=14.54e-6;
Naalpha=20.62e-6;
Nak=24e-3;


%%%%%%%%%%%%%%%%%%%%%%%%%%%%%%%%%%%%%%%%%%%%%%%%%%%%%%%%%%%%%%%%%%%%%%%%%%%%%%%
%%%%%%%%%%%%%%%%%%%%%%%%%%%%%%%%%%%%%%%%%%%%
%%%%%%%%%%%%%%%%%%%%%%%%%%%%Control Volume Creation
%%%%%%%%%%%%%%%%%%%%%%%%%%%%%%%%%%%%

% Set up a numbering scheme to make node indexing easier */
n(1)=nodes(1);
for i=2:length(nodes)
    n(i)=n(i-1)+nodes(i);
end
```

```
% Set up a length scheme to make position indexing easier */
l(1)=len(1);
for i=2:length(nodes)
    l(i)=l(i-1)+len(i);
end
% control volume
cv(1)=2.0*(len(1)/(2.0*nodes(1) + 1));%/* control volume for first
layer */
cv(length(nodes))=2.0*(len(length(nodes))/(2.0*nodes(length(nodes)) +
1)); %/* control volume for last layer */
for i=2:length(nodes)-1
    cv(i)=len(i)/nodes(i);  %/* control volume for ith layer */
end

%% assigning node position and intial temperature for each node.
x(1,1) = 0;
%T(1,1) = T_init(1);
T(1,1) = T_init;
x(1,n(length(nodes)) + 1) = l(length(nodes)-1) + len(length(nodes));
%T(1,n(length(nodes)) + 1) = T_init(length(T_init));
 T(1,n(length(nodes)) + 1) = T_init;
for i=2:nodes(1)
        x(1,i) = x(1,i-1) + cv(1);
        %T(1,i) = T_init(i);
        T(1,i) = T_init;
end

    for j=2:length(nodes)
            for i = 1:nodes(j)
        x(1,n(j-1) + i) = l(j-1) + cv(j)/2.0 + cv(j)*(i-1);
        %T(1,n(j-1) + i) = T_init(n(j-1) + i);
        T(1,n(j-1) + i) = T_init;
            end
    end

    %% Pre Allocating memory

    AP=zeros(1,(n(length(nodes))+1));
    AE=zeros(1,(n(length(nodes))+1));
    AW=zeros(1,(n(length(nodes))+1));
    Ao=zeros(1,(n(length(nodes))+1));
    sp=zeros(1,(n(length(nodes))+1));
    sc=zeros(1,(n(length(nodes))+1));
    b=zeros(1,(n(length(nodes))+1));
    P=zeros(1,(n(length(nodes))+1));
    Q=zeros(1,(n(length(nodes))+1));
    f=zeros(1,length(nodes));
    k_eq=zeros(1,length(nodes));
    Tlastnode=zeros(n_time,1);

    Tlastnode(1,:)=T_init;
    %Tlastnode(1,:)=T_init(length(T_init));

    %% Start of timing loop
    z=1; % z denotes which timing loop (ts)
    s=1; % s denotes which step inside current timing loop (ts)
```

```
  for time = 1:n_time

if s==ts(z)
    z=z+1; % if s is equal to the total number of steps inside timing
loop
    s=0;  % then progress towards next timing loop and reset s
end
clc
disp('percent complete')
disp(z/length(t)*100)
s=s+1;

%% Natural Heat Transfer Coefficient
Ra=abs(real((9.81*Beta*(T(1,n(length(nodes))+1)-
T_inf(2))*L^3)/(Nav*Naalpha))); %Rayleigh number
Nul=0.27*Ra^(1/4); %Nusselt number
Nah=(Nul*Nak)/L; % heat transfer coefficient for natural convection
h=[0,Nah];


JH=J(z)*J(z).*rho_e;
sca=[0,JH(2),JH(1),JH(2),0,0,0,0,0,0,0];

%% Layering
sc(1) = sca(1);
sp(1) = spa(1);
AE(1) = control(1)*k(1)/cv(1);
AW(1) = 0.0;
Ao(1) = control(1)*rho(1)*cp(1)*cv(1)*0.5/Dt;
AP(1) = AE(1) + AW(1) +  Ao(1) + h(1) - sp(1)*cv(1)*0.5*control(1) +
1.0*(1.0 - control(1));
b(1) = T_bc(1) + q(1) + h(1)*T_inf(1) + Ao(1)*T(1,1) +
sc(1)*cv(1)*0.5*control(1);


        for o=2:nodes(1)
               sc(o) = sca(1);
               sp(o) = spa(1);
               AE(o) = k(1)/cv(1);
               AW(o) = k(1)/cv(1);
               Ao(o) = rho(1)*cp(1)*cv(1)/Dt;
               AP(o) = AE(o) + AW(o) + Ao(o) - sp(o)*cv(1);
               b(o) = Ao(o)*T(1,o) + sc(o)*cv(1);
        end

   for p=1:length(nodes)-1
       for i = 2:nodes(p+1)
%

           sc(n(p) + i) = sca(p);
               sp(n(p) + i) = spa(p);
               AE(n(p) + i) = k(p+1)/cv(p+1);
               AW(n(p) + i) = k(p+1)/cv(p+1);
               Ao(n(p) + i) = rho(p+1)*cp(p+1)*cv(p+1)/Dt;
```

```
                AP(n(p) + i) = AE(n(p) + i)+ AW(n(p) + i) + Ao(n(p) + i)
- sp(n(p) + i)*cv(p+1);
                b(n(p) + i) = Ao(n(p) + i)*T(1,n(p) + i) + sc(n(p) +
i)*cv(p+1);
        end

          f(p) = (l(p) - x(n(p)))/(x(n(p)+1) - x(n(p)));
          k_eq(p) = 1.0/((1 - f(p))/k(p) + f(p)/k(p+1));

          AE(n(p)) = k_eq(p)/(0.5*(cv(p) + cv(p+1)));
          AP(n(p)) = AE(n(p)) + AW(n(p)) + Ao(n(p)) - sp(n(p))*cv(p);


        sc(n(p) + 1) = sca(p);
        sp(n(p) + 1) = spa(p);
        AE(n(p) + 1) = k(p+1)/cv(p+1);
        AW(n(p) + 1) = k_eq(p)/(0.5*(cv(p) + cv(p+1)));
        Ao(n(p) + 1) = rho(p+1)*cp(p+1)*cv(p+1)/Dt;
        AP(n(p) + 1) = AE(n(p) + 1) + AW(n(p) + 1) + Ao(n(p) + 1) -
sp(n(p) + 1)*cv(p + 1);
        b(n(p) + 1) = Ao(n(p) + 1)*T(1,n(p) + 1) + sc(n(p) + 1)*cv(p +
1);

    end

 %/* take care of first and last boundary node coefficients,
            %based on type of B.C. */
sc(1) = sca(1);
sp(1) = spa(1);
AE(1) = control(1)*k(1)/cv(1);
AW(1) = 0.0;
Ao(1) = control(1)*rho(1)*cp(1)*cv(1)*0.5/Dt;
AP(1) = AE(1) + AW(1) +  Ao(1) + h(1) - sp(1)*cv(1)*0.5*control(1) +
1.0*(1.0 - control(1));
b(1) = T_bc(1) + q(1) + h(1)*T_inf(1) + Ao(1)*T(1,1) +
sc(1)*cv(1)*0.5*control(1);


j=(n(length(nodes))+1); m=length(nodes);
sc(j) = sca(m);
sp(j) = spa(m);
 AW(j) = control(2)*k(m)/cv(m);
 AE(j) = 0.0;
 Ao(j) = control(2)*rho(m)*cp(m)*cv(m)*0.5/Dt;
 AP(j) = AE(j) + AW(j) +  Ao(j) + h(2) - sp(j)*cv(m)*0.5*control(2) +
1.0*(1.0 - control(2));
 b(j) = T_bc(2) + q(2) + h(2)*T_inf(2) + Ao(j)*T(1,j) +
sc(j)*cv(length(nodes))*0.5*control(2);


%%   applies peliter cooling to nodes around the interface layer
 for a=1:length(layerbc)
  if layerbc(a) ~=0
      qv1(time)=(alpha*J(z)*T(1,n(a)))/(cv(a));
```

```
sc(n(a)+(1)) = qv1(time)*layerbc(a); % Heating/Cooling  at the direct
interface
b(n(a) + 1) = Ao(n(a) + 1)*T(1,n(a) + 1) + sc(n(a) + 1)*cv(a+1);

sc(n(a)-(1)) = qv1(time)*layerbc(a); % Heating/Cooling  at the direct
interface
b(n(a) - 1) = Ao(n(a) - 1)*T(1,n(a) - 1) + sc(n(a) - 1)*cv(a - 1);

sc(n(a)) = qv1(time)*layerbc(a); % Heating/Cooling  at the direct
interface
b(n(a)) = Ao(n(a))*T(1,n(a)) + sc(n(a))*cv(a);

  end
 end



   %/* Solve for the temperature field using TDMA.  Move in positive x
dir. */

         P(1) = AE(1)/AP(1);
         Q(1) = b(1)/AP(1);

         for i = 2:n(length(nodes))+1
            P(i) = AE(i)/(AP(i) - AW(i)*P(i-1));
            Q(i) = (b(i) + AW(i)*Q(i-1))/(AP(i) - AW(i)*P(i-1));
         end

         T(1, n(length(nodes)) + 1) = Q(n(length(nodes)) + 1);

         for i = n(length(nodes)):-1:1
            T(1,i) = P(i)*T(1,i+1) + Q(i);
         end

Tlastnode(time+1,:)=T(1,n(length(nodes))+1);

  end
  % creates time array for plotting
  ttime(1)=0;
  for q=2:n_time+1
      ttime(q)=ttime(q-1)+Dt;
  end


  figure(1)
  hold on
  plot(ttime,Tlastnode)
  plot(t,Tprof,'r')
  xlabel('time (s)')
  ylabel('Temperature of last node')
  hold off

toc
MM=[ttime',Tlastnode];
```

```
xlswrite('Data',MM)
```

Control System

```
CR=1.3; % cooling rate (K/s)
tend=65; % time ending
tstep=0.05; % time step
t=0:tstep:tend; % creates time array
Ttarget(1)=289.268;
for k=2:length(t)
    Ttarget(k)=(Ttarget(k-1)-(CR*tstep)); % creates target temperature
rate for tracking
end
T_init=xlsread('Tinit','A1:A7003');  % inputs initial temperature
distrubtion
Objupper=5.5; % upper current level
Objlower=0; % lower current level
%flag=zeros(1,length(Ttarget)); % flag=1 cooling mode , flag=0 heating
mode
flag=0;
Ao=2;

for j=1:length(Ttarget)

[Aa(j),fval(j)]=fmincon(@(A)Objective(A,Ttarget(j),T_init,flag),Ao,[],[
],[],[],Objlower,Objupper);
[Tlastnode(j),T]=controlsystem(Aa(j),T_init,flag);
T_init=T;

if j>20
        if Aa(j)==0
        flag=1;
        end
    end

end
xlswrite('control',Aa','A2:A1700')
xlswrite('control',t','B2:B1700')
xlswrite('control',Tlastnode','C2:C1700')

function Tobj=Objective(A,Ttarget,T_init,flag)
Tlastnode=controlsystem(A,T_init,flag);
Tobj=abs(Tlastnode-Ttarget);
end



%% Build model by adding thermodynamic properties into array

%% layer properties
cv1=1*10e-9; %control volume size (m)
cv2=8*10e-7;
cv3=2*10e-7;
```

```
cv4=3*10e-8;
cv5=6*10e-9;

% Layering Scheme: ceramic, copper, bismuth telluride, copper, ceramic,
copper, glass,
% bismuth telluride, copper, water, Type E themoelectric

k=[35,401,1.48,401,35,1.4,401,1.2,401,569e-3,(21.9+16.7)];
%(W/m)Thermal conductivity of layers (1,2,3..)
rho=[3750,8960,7700,8960,3750,2225,8960,7700,8960,1000,8730];  %
(kg/m^3)density of layers (1,2,3..)
cp=[775,390,122,390,775,835,390,122,390,4217,(4.07e-1+3.984e-1)]; %
(J/kg*K)heat capacity of layers (1,2,3..)
len=[0.0006858,0.0004318,0.00127,0.0004318,0.0006858,0.0001524,0.000152
4,500e-6,30e-6,10e-6,25e-6]; %(m)length of layers (1,2,3..)
%nodes=[round(len(1)/cvl),round(len(2)/cvl),round(len(3)/cv2),round(len
(4)/cvl),round(len(5)/cvl),round(len(6)/cv3),round(len(7)/cv4)]; %nodes
of layers (1,2,3..)

 nodes=[500,600,1200,600,500,500,500,800,600,600,600]; %mesh
independent volume



%% Experimental Model Properties


  %% Specify Time step
  Dt=0.05; % constant time step [s]

 %%%%%%%%%%%%%%%%%%%%%calculation ensure s even time
step%%%%%%%%%%%%%%%%%%%%%%
%%%%%%%%%%%%%%%%%%%%%%%%%%%%%%%%%%%%%%%%%%%%%%%%%%%%%%%%%%%%%%%%%%%%%%%%%%%
%%%%%%

 %% Specify Initial Temperature
 J=(Jo./(2.17e-6))';%* electric current density in [A/m2]
 rho_e = [(8.58e-6+8.82e-6),1.68e-8];%/* electric resistivity in [ohm-
m] */
 alpha = 0.34*1.92e-4; %/* Seebeck coefficient [V/K] */

%% Internal Heat generation & Boundary Conditions
spa=[0,0,0,0,0,0,0,0,0,0,0];
sca=[0,0,0,0,0,0,0,0,0,0,0];
layerbc=[0,1,-1,0,0,0,0,0,0,0];% applies peltier cooling/heating at
layer interfaces -1=cooling 1=heating
control = [0,1]; %/* control should be 0 if a temperature BC is used
and 1 otherwise */
T_bc =[251,0]; %Temperature Boundary Conditions
q = [0,0]; % conduction B.C.
h = [0,0.5]; % heat transfer coefficient for convection B.C.
T_inf = [0,288]; % ambient air temperature for convection B.C.

%% Natural convection information
```

```
L=(1.95e-6)/(0.0056); %charcteristic length (A/P)
Beta=1/T_inf(2); %
Nav=14.54e-6;
Naalpha=20.62e-6;
Nak=24e-3;


%%%%%%%%%%%%%%%%%%%%%%%%%%%%%%%%%%%%%%%%%%%%%%%%%%%%%%%%%%%%%%%%%%%%%%%%%
%%%%%%%%%%%%%%%%%%%%%%%%%%%%%%%%%%%%%%%
%%%%%%%%%%%%%%%%%%%%%%%%%%%Control Volume Creation
%%%%%%%%%%%%%%%%%%%%%%%%%%%%%%%%%%%

% Set up a numbering scheme to make node indexing easier */
n(1)=nodes(1);
for i=2:length(nodes)
    n(i)=n(i-1)+nodes(i);
end
% Set up a length scheme to make position indexing easier */
l(1)=len(1);
for i=2:length(nodes)
    l(i)=l(i-1)+len(i);
end
% control volume
cv(1)=2.0*(len(1)/(2.0*nodes(1) + 1));%/* control volume for first
layer */
cv(length(nodes))=2.0*(len(length(nodes))/(2.0*nodes(length(nodes)) +
1)); %/* control volume for last layer */
for i=2:length(nodes)-1
    cv(i)=len(i)/nodes(i);  %/* control volume for ith layer */
end

%% assigning node position and intial temperature for each node.
x(1,1) = 0;
T(1,1) = T_init(1);
x(1,n(length(nodes)) + 1) = l(length(nodes)-1) + len(length(nodes));
T(1,n(length(nodes)) + 1) = T_init(length(T_init));

for i=2:nodes(1)
        x(1,i) = x(1,i-1) + cv(1);
        T(1,i) = T_init(i);
end

    for j=2:length(nodes)
            for i = 1:nodes(j)
        x(1,n(j-1) + i) = l(j-1) + cv(j)/2.0 + cv(j)*(i-1);
        T(1,n(j-1) + i) = T_init(n(j-1) + i);
            end
    end

    %% Pre Allocating memory

    AP=zeros(1,(n(length(nodes))+1));
    AE=zeros(1,(n(length(nodes))+1));
    AW=zeros(1,(n(length(nodes))+1));
    Ao=zeros(1,(n(length(nodes))+1));
```

```
    sp=zeros(1,(n(length(nodes))+1));
    sc=zeros(1,(n(length(nodes))+1));
    b=zeros(1,(n(length(nodes))+1));
    P=zeros(1,(n(length(nodes))+1));
    Q=zeros(1,(n(length(nodes))+1));
    f=zeros(1,length(nodes));
    k_eq=zeros(1,length(nodes));


    %Tlastnode=T_init(length(T_init));

    %% Start of timing loop


%% Natural Heat Transfer Coefficient
Ra=abs(real((9.81*Beta*(T(1,n(length(nodes))+1)-
T_inf(2))*L^3)/(Nav*Naalpha))); %Rayleigh number
Nul=0.27*Ra^(1/4); %Nusselt number
Nah=(Nul*Nak)/L; % heat transfer coefficient for natural convection
h=[0,Nah];

JH=J*J.*rho_e;
sca=[0,JH(2),JH(1),JH(2),0,0,0,0,0,0,0];

%% Layering
sc(1) = sca(1);
sp(1) = spa(1);
AE(1) = control(1)*k(1)/cv(1);
AW(1) = 0.0;
Ao(1) = control(1)*rho(1)*cp(1)*cv(1)*0.5/Dt;
AP(1) = AE(1) + AW(1) +  Ao(1) + h(1) - sp(1)*cv(1)*0.5*control(1) +
1.0*(1.0 - control(1));
b(1) = T_bc(1) + q(1) + h(1)*T_inf(1) + Ao(1)*T(1,1) +
sc(1)*cv(1)*0.5*control(1);


        for o=2:nodes(1)
               sc(o) = sca(1);
               sp(o) = spa(1);
               AE(o) = k(1)/cv(1);
               AW(o) = k(1)/cv(1);
               Ao(o) = rho(1)*cp(1)*cv(1)/Dt;
               AP(o) = AE(o) + AW(o) + Ao(o) - sp(o)*cv(1);
               b(o) = Ao(o)*T(1,o) + sc(o)*cv(1);
        end

   for p=1:length(nodes)-1
       for i = 2:nodes(p+1)
%
           sc(n(p) + i) = sca(p);
               sp(n(p) + i) = spa(p);
               AE(n(p) + i) = k(p+1)/cv(p+1);
               AW(n(p) + i) = k(p+1)/cv(p+1);
               Ao(n(p) + i) = rho(p+1)*cp(p+1)*cv(p+1)/Dt;
```

```
                AP(n(p) + i) = AE(n(p) + i)+ AW(n(p) + i) + Ao(n(p) + i)
- sp(n(p) + i)*cv(p+1);
                b(n(p) + i) = Ao(n(p) + i)*T(1,n(p) + i) + sc(n(p) +
i)*cv(p+1);
        end

          f(p) = (l(p) - x(n(p)))/(x(n(p)+1) - x(n(p)));
          k_eq(p) = 1.0/((1 - f(p))/k(p) + f(p)/k(p+1));

          AE(n(p)) = k_eq(p)/(0.5*(cv(p) + cv(p+1)));
          AP(n(p)) = AE(n(p)) + AW(n(p)) + Ao(n(p)) - sp(n(p))*cv(p);


        sc(n(p) + 1) = sca(p);
        sp(n(p) + 1) = spa(p);
        AE(n(p) + 1) = k(p+1)/cv(p+1);
        AW(n(p) + 1) = k_eq(p)/(0.5*(cv(p) + cv(p+1)));
        Ao(n(p) + 1) = rho(p+1)*cp(p+1)*cv(p+1)/Dt;
        AP(n(p) + 1) = AE(n(p) + 1) + AW(n(p) + 1) + Ao(n(p) + 1) -
sp(n(p) + 1)*cv(p + 1);
        b(n(p) + 1) = Ao(n(p) + 1)*T(1,n(p) + 1) + sc(n(p) + 1)*cv(p +
1);

    end

 %/* take care of first and last boundary node coefficients,
            %based on type of B.C. */
sc(1) = sca(1);
sp(1) = spa(1);
AE(1) = control(1)*k(1)/cv(1);
AW(1) = 0.0;
Ao(1) = control(1)*rho(1)*cp(1)*cv(1)*0.5/Dt;
AP(1) = AE(1) + AW(1) +  Ao(1) + h(1) - sp(1)*cv(1)*0.5*control(1) +
1.0*(1.0 - control(1));
b(1) = T_bc(1) + q(1) + h(1)*T_inf(1) + Ao(1)*T(1,1) +
sc(1)*cv(1)*0.5*control(1);


j=(n(length(nodes))+1); m=length(nodes);
sc(j) = sca(m);
sp(j) = spa(m);
 AW(j) = control(2)*k(m)/cv(m);
 AE(j) = 0.0;
 Ao(j) = control(2)*rho(m)*cp(m)*cv(m)*0.5/Dt;
 AP(j) = AE(j) + AW(j) +  Ao(j) + h(2) - sp(j)*cv(m)*0.5*control(2) +
1.0*(1.0 - control(2));
 b(j) = T_bc(2) + q(2) + h(2)*T_inf(2) + Ao(j)*T(1,j) +
sc(j)*cv(length(nodes))*0.5*control(2);


%%   applies peliter cooling to nodes around the interface layer
 for a=1:length(layerbc)
  if layerbc(a) ~=0
%
      qv1=(alpha*J*T(1,n(a)))/(cv(a));
```

```
sc(n(a)+(1)) = qv1*layerbc(a); % Heating/Cooling  at the direct
interface
b(n(a) + 1) = Ao(n(a) + 1)*T(1,n(a) + 1) + sc(n(a) + 1)*cv(a+1);

sc(n(a)-(1)) = qv1*layerbc(a); % Heating/Cooling  at the direct
interface
b(n(a) - 1) = Ao(n(a) - 1)*T(1,n(a) - 1) + sc(n(a) - 1)*cv(a - 1);

sc(n(a)) = qv1*layerbc(a); % Heating/Cooling  at the direct interface
b(n(a)) = Ao(n(a))*T(1,n(a)) + sc(n(a))*cv(a);

  end
 end



   %/* Solve for the temperature field using TDMA.  Move in positive x
dir. */

         P(1) = AE(1)/AP(1);
         Q(1) = b(1)/AP(1);

         for i = 2:n(length(nodes))+1
            P(i) = AE(i)/(AP(i) - AW(i)*P(i-1));
            Q(i) = (b(i) + AW(i)*Q(i-1))/(AP(i) - AW(i)*P(i-1));
         end

         T(1, n(length(nodes)) + 1) = Q(n(length(nodes)) + 1);

         for i = n(length(nodes)):-1:1
            T(1,i) = P(i)*T(1,i+1) + Q(i);
         end

Tlastnode=T(1,n(length(nodes))+1);


end
```

DTA Area Calculator:

```
%Written by: Logan Compton
%11/22/10
%7/9/11
%=================================================================
===

%% Imports 2 CSV temperature profile files and finds area under
temperature spike
%base=base line temperature profile csv file
%data=water droplet temperature profile csv file
```

```
fprintf('Select desired profile X file...') % allows user to select
profile file
basefolder1=uigetdir('C:\Users\Linkin\Desktop');
base1=uigetfile({'*.csv';'*.xls'},'',basefolder1);
clc
fprintf('Select desired profile Y file...') % allows user to select
profile file
base2=uigetfile({'*.csv';'*.xls'},'',basefolder1);
clc

t1 = xlsread(fullfile(basefolder1, base1),'B4:B3600');% xX
T1=xlsread(fullfile(basefolder1, base1),'C4:C3600');% yX
t2 = xlsread(fullfile(basefolder1, base2),'B4:B3600');% xY
T2=xlsread(fullfile(basefolder1, base2),'C4:C3600');% yY
T1=T1+273;
T2=T2+273;



figure(1)
hold on
plot(t1,T1,'b')
plot(t2,T2,'r')
xlabel('time')
ylabel('Temperature [C]')
ng= input('Data Range and order of polynominal fit? [start time, end
time, order] '); % user inputs selected range
stt=ng(1); endt=ng(2);
Max=round(mean(find(t1<=stt+0.03 & t1>=stt-0.03 ))); % determines
starting point for polyfit
minend=round(mean(find(t1<=endt+0.03 & t1>=endt-0.03 )));% determines
ending point for polyfit
Tdiff=T2-T1;% subtracts profile
N=length(Tdiff);
%% Finds the Temperature Spike
delt=Tdiff(Max)-0; % Finds the difference between the starting point
and the x-axis to determine the correct area under the curve.
Tdiff2=Tdiff(Max:minend)-delt; %Creates new Tdiff profile isolating
temperature spike for integration
tdiff=t1(Max);
t3=t1(Max:minend)-tdiff;

%% Calculates the Area under the curve.
N=length(Tdiff2);
pp = pchip(t3,Tdiff2);
Area = quad(@(t3)ppval(pp,t3),t3(1),t3(N))%finds area under Tdiff
profile
YY=pchip(t3,Tdiff2,t3);

%% Plotting
figure(1)
subplot(2,2,1)
plot(t1,T1,'r')
title('Base Line Temperature Profile')
xlabel('Time (s)')
ylabel('Temperature [C]')
axis tight
```

```
subplot(2,2,2)
hold on
plot(t1,T1)
plot(t1,T2,'r')
hold off
title('Water Droplet Temperature Profile')
xlabel('Time (s)')
ylabel('Temperature [C]')
axis tight
subplot(2,2,3)
plot(t1,Tdiff)
title('Temperature Difference')
xlabel('Time (s)')
ylabel('Temperature [C]')
axis tight
grid on
subplot(2,2,4)
plot(t3,Tdiff2,'x',t3,YY)
title('Area Under Curve')
xlabel('Time (s)')
ylabel('Temperature [C]')
axis tight
grid on
A=num2str(Area);
text(0.25,2,A)

figure(2)
hold on
plot(t1,T1,'r')
plot(t1,T2,'y')
title('Data Comparison')
xlabel('time (s)')
ylabel('Temperature (T)')
grid on
hold off

for n = 1:2
saveas(figure(n),[basefolder1 filesep 'Area Plot' num2str(n)], 'jpg')
end
```

DTA Heat Capacity Calculator:

```
function []=DSCtool
%=====================================================================
===
%Written by: Logan Compton
%12/19/10
%Revised 1/20/11
%Revised 1/28/11
%Revised 2/4/11
%Revised 3/22/12
%=====================================================================
===
rho=0.0009999432; % (g/mm^3)
```

```
vls=0.001709766;%(mm^3)

c=4.199; %(J/g*K)
vss=0.000940371;% (mm^3)


%% Imports 2 CSV temperature profile files and determines the sample
holder
%% temperature properities

%base=base line temperature profile csv file
%data=sample temperature profile csv file
%rho=sample density (kg/m^3)
%v=sample volume (m^3)
%c=sample specific heat capacity (J/kg K)
%stt= time starting point
%endt= end time
%ord=order of differation

% lets user find desired base and sample files
fprintf('Select desired profile X file...') % allows user to select
profile file
basefolder1=uigetdir('C:\Users\Linkin\Desktop');
base1=uigetfile({'*.csv';'*.xls'},'',basefolder1);
clc
fprintf('Select desired profile Y file...') % allows user to select
profile file
base2=uigetfile({'*.csv';'*.xls'},'',basefolder1);
clc

t1 = xlsread(fullfile(basefolder1, base1),'B4:B3600');% xX
T1=xlsread(fullfile(basefolder1, base1),'C4:C3600');% yX
t2 = xlsread(fullfile(basefolder1, base2),'B4:B3600');% xY
T2=xlsread(fullfile(basefolder1, base2),'C4:C3600');% yY


figure(1)
hold on
plot(t1,T1,'b')
plot(t2,T2,'r')
xlabel('time')
ylabel('Temperature [C]')
h = legend('Base','Sample',2);
set(h,'Interpreter','none')

%%=============================Calibration============================
====

flag=1;
cycle=1;

while flag==1;
clear t1n t2n T1n T2n h1 h2 T1val T2val DDT1 DDT2 t1ns t1s t2ns PropBDD
UDDT1 UDDT2 UDPropBDD DPropBDDDV DPropBDDDDTdt2 DPropBDDDDTdt1
```

```
    if cycle ==1;
  clc
  ng= input('Data Range and order of polynominal fit? [start time, end
time, order] '); % user inputs selected range
  stt=ng(1); endt=ng(2);
flag=1;
else
        flag=0 ;
end
       if flag==0
    break
end


st=round(mean(find(t1<=stt+0.05 & t1>=stt-0.05 )));
Endref=round(mean(find(t1<=endt+0.05 & t1>=endt-0.05 )));

% Polynomial fitting of Temperature profile of bridge only
t1n=t1(st:Endref); %truncates old time profile
h1=mean(diff(t1n)); % finds the mean time spacing
[T1n,S1,mu1]=polyfit(t1n,T1(st:Endref),1); %creates polynomial
t1ns=t1n(1):h1:t1n(length(t1n)); %new evenly spaced time
[T1val,uT1]=polyval(T1n,t1ns,S1,mu1); %evaluates polynomial at even
time intervals

% Polynomial fitting of Temperature profile of bridge and sample
t2n=t2(st:Endref);%truncates old time profile
h2=mean(diff(t2n));% finds the mean time spacing
[T2n,S2,mu2]=polyfit(t2n,T2(st:Endref),1);%creates polynomial
t2ns=t2n(1):h2:t2n(length(t2n));%new evenly spaced time
[T2val,uT2]=polyval(T2n,t2ns,S2,mu2); %evaluates polynomial at even
time intervals


%% First order derivative for discritized data from 5 order Taylor
series

for i=3:length(T1val)-2
    DDT1(i)=(8*(T1val(i+1)-T1val(i-1))+(T1val(i-2)-
T1val(i+2)))/(12*h1);
    DDT2(i)=(8*(T2val(i+1)-T2val(i-1))+(T2val(i-2)-
T2val(i+2)))/(12*h2);
end

t1s=t1ns(1:length(DDT1)); % creates new time profile for plotting
t2s=t1s;

%=======================Calculation of Bridge Property
====================

%PropBDD=abs(((rho*c*v)*(DDT2))./((DDT1-DDT2)));
MDDT2=abs(mean(DDT2));
MDDT1=abs(mean(DDT1));
PropBDD=mean((((MDDT2*vls)-(MDDT1*vss))*rho*c)./(MDDT1-MDDT2));
```

```
%==============================plotting================================
====

trunDD=find(t1s>stt); % finds where to truncate bridge property plot
from user input
T1vallen=length(PropBDD); % determines how many data points are used
str = num2str(T1vallen); % to polot the value on the plot
figure (2)
subplot(2,2,1)
hold on
plot(t1,T1)
plot(t2,T2,'r')
title('original data')
xlabel('time(s)')
ylabel('Temperature(C)')
axis tight
hold off
subplot(2,2,3)
hold on
plot(t1s, DDT1,'b')
plot(t2s, DDT2,'r')
title('1st Derivative of Data')
xlabel('time(s)')
ylabel('Cooling Rate(C/s)')
h = legend('Base','Sample',2);
set(h,'Interpreter','none')
hold off
subplot(2,2,2)
hold on
title('Truncated Smoothed')
plot(t1ns,T1val)
plot(t2ns,T2val,'red')
plot(t1,T1,'green')
plot(t2,T2,'black')
axis([t2ns(1),t1ns(length(t1ns)),T2val(length(T2val)),T1val(1)])
xlabel('time(s)')
ylabel('Temperature(C)')

hold off
subplot(2,2,4)
hold on
title('Temperature Uncertainty')
xlabel('time(s)')
ylabel('Temperature (C)')
plot(t1ns,uT1)
plot(t2ns,uT2,'r')
axis tight
hold off

write=input('do you want to write this to file (Yes=1, No=2) ');
if write==1
%M=[t1s(trunDD:length(PropBDD))',PropBDD(trunDD:length(PropBDD))',UDPro
pBDD(trunDD:length(PropBDD))'];
PropBDD
MDDT1
```

```
MDDT2
M=[PropBDD;MDDT1;MDDT2];
newfolder=[basefolder1 filesep 'bridge properties'];
xlswrite(newfolder,M,'A2:A6');
% for n = 1:2
% saveas(figure(n),[dir filesep 'bridge properties plot' num2str(n)],
'jpg')
% end
end
cycle=input('Do you want to change the data range? (Yes=1, No=2) ');
end
```

Height as a function of Diameter Calculator

```
clear all

fprintf('Select desired profile X file...') % allows user to select
profile file
basefolder1=uigetdir('C:\Users\Linkin\Desktop');
base1=uigetfile({'*.csv';'*.xls'},'',basefolder1);


x = xlsread(fullfile(basefolder1, base1),'A4:A800');% xX
y=xlsread(fullfile(basefolder1, base1),'B4:B800');% yX

if abs(x(2))<.01
    x=x*10^3; % converts mm to micron
end
if abs(y(2))<.01
    y=y*10^3; % converts mm to micron
end

%% allows user to select the beggining and end points of the profile

figure(1)
plot(x,y,'o')
title('Xdata')
xlabel('x axis (micron)')
ylabel('depth (micron)')



start1=input('xcordinate where curve starts of Xdata '); % start of
crucible X
finish1=input('xcordinate where curve finishes of Xdata'); % end of
crucible X
Diameter=finish1-start1


startvX=round(mean(find(x<=start1+1 & x>=start1-1 ))); % finds the
start value point
finishvX=round(mean(find(x<=finish1+1 & x>=finish1-1))); %finds the
finish value point
```

```
centervX(1)=round(mean(find(x<=mean(x(startvX:finishvX))+1 &
x>=mean(x(startvX:finishvX))-1))); % center based on centroid




%% appropriately splits the profile in two halves to perform to volume
%% calculations

clear V1 V2 V3 V4 A1X A1Y A2X A2Y B1X B1Y B2X B2Y sim1X sim1Y sim2X
sim2Y
clear Xhalf1newX Yhalf1newX Xhalf2newX Yhalf2newX Xhalf1newY Yhalf1newY
Xhalf2newY Yhalf2newY
clear Xhalf1X Yhalf1X Xhalf2X Yhalf2X Xhalf1Y Yhalf1Y Xhalf2Y Yhalf2Y

% splits X profile into two halves
Xhalf1X=x(startvX:centervX);
Yhalf1X=y(startvX:centervX);
Xhalf2X=x(centervX:finishvX);
Yhalf2X=y(centervX:finishvX);
Depth1=y(startvX)-y(centervX);

Xhalf1newX=Xhalf1X-Xhalf1X(length(Xhalf1X));
Yhalf1newX=Yhalf1X-Yhalf1X(length(Yhalf1X));
Xhalf2newX=Xhalf2X-Xhalf2X(1);
Yhalf2newX=Yhalf2X-Yhalf2X(1);

polytool(Yhalf2newX,Xhalf2newX,4)

deg1=input('degree of fit for 1st curve ');
[fit1,s1,m1]=polyfit(Yhalf2newX,Xhalf2newX,5);

[fit2,s2,m2]=polyfit(Yhalf1newX,Xhalf1newX,5);

Y1=linspace(Yhalf1newX(1),Yhalf1newX(length(Yhalf1newX)),300);

X1=polyval(fit2,Y1,s2,m2);

for i=1:length(Y1)

X2=polyval(fit1,Y1(i),s1,m1);

D(i)=X2-X1(i);

end

Yinv=linspace(Yhalf1newX(length(Yhalf1newX)),Yhalf1newX(1),300);

flag=input('is this x or y profile; x=1 y=2');
if flag==1
xlswrite('HFDX',[D',Yinv'])
end
if flag==2
```

```
xlswrite('HFDY',[D',Yinv'])
end
```

Volume as a function of Height Calculator

```
Hy=xlsread('HFDY','B1:B301');

Diax2=xlsread('HFDX2','A1:A301');
Hx2=xlsread('HFDX2','B1:B301');
Diay2=xlsread('HFDY2','A1:A301');
Hy2=xlsread('HFDY2','B1:B301');

Vh=xlsread('Volume','A4:A840')*10^-3;
V=xlsread('Volume','B4:B840');
flag=1;

while flag==1
 proflag=input('enter if X (1) or Y (2) ');
FDD=input('enter Diameter [mean,uncertainty] ');
FD=[FDD(1),FDD(1)+FDD(2),FDD(1)-FDD(2)];
 for i=1:3
if proflag==1
if FD(1)<224.71 && FD(2)<224.71
    DPX=round(mean(find(Diax<=FD(i)+.2 & Diax>=FD(i)-.2 ))); % finds
the Diameter Point
if FD(i)<Diax(DPX)
    AHx=((FD(i)-Diax(DPX+1))*(Hx(DPX)-(Hx(DPX+1)))/(Diax(DPX)-
Diax(DPX+1)))+Hx(DPX+1);
end
if FD(i)>Diax(DPX)
    AHx=((FD(i)-Diax(DPX-1))*(Hx(DPX)-(Hx(DPX-1)))/(Diax(DPX)-Diax(DPX-
1)))+Hx(DPX-1);
end
VPX=round(mean(find(Vh<=AHx+.1 & Vh>=AHx-.1 ))); % finds the Volume
Point
if AHx<Vh(VPX)
    Volumex=((AHx-Vh(VPX+1))*(V(VPX)-(V(VPX+1)))/(AHx-
Vh(DPX+1)))+V(DPX+1);
end
if AHx>Vh(VPX)
    Volumex=((AHx-Vh(VPX-1))*(V(VPX)-(V(VPX-1)))/(AHx-Vh(DPX-
1)))+V(DPX-1);
end

end
DPX2=round(mean(find(Diax2<=FD(i)+.2 & Diax2>=FD(i)-.2 ))); % finds the
Diameter Point
if FD(i)<Diax2(DPX2)
    AHx2=((FD(i)-Diax2(DPX2+1))*(Hx2(DPX2)-(Hx2(DPX2+1)))/(Diax2(DPX2)-
Diax2(DPX2+1)))+Hx2(DPX2+1);
end
if FD(i)>Diax2(DPX2)
    AHx2=((FD(i)-Diax2(DPX2-1))*(Hx2(DPX2)-(Hx2(DPX2-1)))/(Diax2(DPX2)-
Diax2(DPX2-1)))+Hx2(DPX2-1);
end
```

```
VPX2=round(mean(find(Vh<=AHx2+.1 & Vh>=AHx2-.1 ))); % finds the Volume
Point
if AHx2<Vh(VPX2)
    Volumex2=((AHx2-Vh(VPX2+1))*(V(VPX2)-(V(VPX2+1)))/(AHx2-
Vh(DPX2+1)))+V(DPX2+1);
end
if AHx2>Vh(VPX2)
    Volumex2=((AHx2-Vh(VPX2-1))*(V(VPX2)-(V(VPX2-1)))/(AHx2-Vh(DPX2-
1)))+V(DPX2-1);
end
Volumeav(i)=Volumex2;
VolStd=FDD(2);
if FD(1)<224.71 && FD(2)<224.71
Volumeav(i)=mean([Volumex,Volumex2]);
VolStd=std([Volumex,Volumex2]);
end
end
if proflag==2
DPY=round(mean(find(Diay<=FD(i)+.4 & Diay>=FD(i)-.4 )));
if FD(i)<Diay(DPY)
    AHy=((FD(i)-Diay(DPY+1))*(Hy(DPY)-(Hy(DPY+1)))/(Diay(DPY)-
Diay(DPY+1)))+Hy(DPY+1);
end
if FD(i)>Diay(DPY)
    AHy=((FD(i)-Diay(DPY-1))*(Hy(DPY)-(Hy(DPY-1)))/(Diay(DPY)-Diay(DPY-
1)))+Hy(DPY-1);
end

DPY2=round(mean(find(Diay2<=FD(i)+.4 & Diay2>=FD(i)-.4 )));
if FD(i)<Diay2(DPY2)
    AHy2=((FD(i)-Diay2(DPY2+1))*(Hy2(DPY2)-(Hy2(DPY2+1)))/(Diay2(DPY2)-
Diay2(DPY2+1)))+Hy2(DPY2+1);
end
if FD(i)>Diay2(DPY2)
    AHy2=((FD(i)-Diay2(DPY2-1))*(Hy2(DPY2)-(Hy2(DPY2-1)))/(Diay2(DPY2)-
Diay2(DPY2-1)))+Hy2(DPY2-1);
end

VPY=round(mean(find(Vh<=AHy+.1 & Vh>=AHy-.1 )));
if AHy<Vh(VPY)
    Volumey=((AHy-Vh(VPY+1))*(V(VPY)-(V(VPY+1)))/(AHy-
Vh(DPY+1)))+V(DPY+1);
end
if AHy>Vh(VPY)
    Volumey=((AHy-Vh(VPY-1))*(V(VPY)-(V(VPY-1)))/(AHy-Vh(DPY-
1)))+V(DPY-1);
end

VPY2=round(mean(find(Vh<=AHy2+.1 & Vh>=AHy2-.1 )));
if AHy2<Vh(VPY2)
    Volumey2=((AHy2-Vh(VPY2+1))*(V(VPY2)-(V(VPY2+1)))/(AHy2-
Vh(DPY2+1)))+V(DPY2+1);
end
```

```
if AHy2>Vh(VPY2)
    Volumey2=((AHy2-Vh(VPY2-1))*(V(VPY2)-(V(VPY2-1)))/(AHy2-Vh(DPY2-
1)))+V(DPY2-1);
end
Volumeav(i)=mean([Volumey,Volumey2]);
VolStd=std([Volumey,Volumey2]);
end


end
VolDiaUnc=abs(Volumeav(3)-Volumeav(2))/2;
Volume=[Volumeav(1),VolDiaUnc]
flag=input('find another volume? 1=yes 0=no ');
end
```

Crucible Volume Homogeneity Program

```
clear all

MaskD=205; % Mean Mask Diameter

fprintf('Select desired profile X file...') % allows user to select
profile file
basefolder1=uigetdir('C:\Users\Linkin\Desktop');
base1=uigetfile({'*.csv';'*.xls'},'',basefolder1);
clc
fprintf('Select desired profile Y file...') % allows user to select
profile file
base2=uigetfile({'*.csv';'*.xls'},'',basefolder1);
clc

xx = xlsread(fullfile(basefolder1, base1),'A4:A800');% xX
yx=xlsread(fullfile(basefolder1, base1),'B4:B800');% yX
xy = xlsread(fullfile(basefolder1, base2),'A4:A800');% xY
yy=xlsread(fullfile(basefolder1, base2),'B4:B800');% yY


if abs(xx(3))<.01
    xx=xx*10^3; % converts mm to micron
end
if abs(yx(3))<.01
    yx=yx*10^3; % converts mm to micron
end
if abs(xy(3))<.01
    xy=xy*10^3; % converts mm to micron
end
if abs(yy(3))<.01
    yy=yy*10^3; % converts mm to micron
end

if abs(xx(1))>100
    xx=xx*10^-3; % converts mm to micron
end
```

```
if abs(yx(1))>100
    yx=yx*10^-3; % converts mm to micron
end
if abs(xy(1))>100
    xy=xy*10^-3; % converts mm to micron
end
if abs(yy(1))>100
    yy=yy*10^-3; % converts mm to micron
end
%% allows user to select the beggining and end points of the profile


figure(1)
subplot(2,1,1)
plot(xx,yx,'o')
title('Xdata')
xlabel('x axis (micron)')
ylabel('depth (micron)')
subplot(2,1,2)
plot(xy,yy,'o')
title('Ydata')
xlabel('x axis (micron)')
ylabel('depth (micron)')


start1=input('xcordinate where curve starts of Xdata '); % start of
crucible X
finish1=input('xcordinate where curve finishes of Xdata'); % end of
crucible X

start2=input('xcordinate where curve starts of Ydata '); % start of
crucible Y
finish2=input('xcordinate where curve finishes of Ydata'); % end of
crucible Y



rad1=(finish1-start1)/2; % radius of curve X
rad2=(finish2-start2)/2; % radius of curve Y

% determines which radius profile is larger (major axis) or smaller
(minor
% axis)
if rad1>=rad2
    a=rad1;
    b=rad2;
    flag=1; %denotes that X file is 'a'
elseif rad2>rad1
    a=rad2;
    b=rad1;
    flag=2; %denotes that Y file is 'a'
end

f=sqrt(a^2-b^2)/a;  % Ellipse factor
rat=a/b; % ratio of radius
```

```
startvX=round(mean(find(xx<=start1+1 & xx>=start1-1 ))); % finds the
start value point
finishvX=round(mean(find(xx<=finish1+1 & xx>=finish1-1))); %finds the
finish value point
centervX(1)=round(mean(find(xx<=mean(xx(startvX:finishvX))+1 &
xx>=mean(xx(startvX:finishvX))-1))); % center based on centroid
centervX(2)=round(mean(find(yx<=min(yx(startvX:finishvX))+1 &
yx>=min(yx(startvX:finishvX))-1))); % center based on minimum value

startvY=round(mean(find(xy<=start2+1 & xy>=start2-1 ))); % finds the
start value point
finishvY=round(mean(find(xy<=finish2+1 & xy>=finish2-1))); %finds the
finish value point
centervY(1)=round(mean(find(xy<=mean(xy(startvY:finishvY))+1 &
xy>=mean(xy(startvY:finishvY))-1)));% center based on centroid
centervY(2)=round(mean(find(yy<=min(yy(startvY:finishvY))+1 &
yy>=min(yy(startvY:finishvY))-1)));% center based on minimum value

%% appropriately splits the profile in two halves to perform to volume
%% calculations
for p=1:2
clear V1 V2 V3 V4 A1X A1Y A2X A2Y B1X B1Y B2X B2Y sim1X sim1Y sim2X
sim2Y
clear Xhalf1newX Yhalf1newX Xhalf2newX Yhalf2newX Xhalf1newY Yhalf1newY
Xhalf2newY Yhalf2newY
clear Xhalf1X Yhalf1X Xhalf2X Yhalf2X Xhalf1Y Yhalf1Y Xhalf2Y Yhalf2Y

% splits X profile into two halves
Xhalf1X=xx(startvX:centervX(p));
Yhalf1X=yx(startvX:centervX(p));
Xhalf2X=xx(centervX(p):finishvX);
Yhalf2X=yx(centervX(p):finishvX);
Depth1=yx(startvX)-yx(centervX(2));
% splits Y profile into two havles
Xhalf1Y=xy(startvY:centervY(p));
Yhalf1Y=yy(startvY:centervY(p));
Xhalf2Y=xy(centervY(p):finishvY);
Yhalf2Y=yy(centervY(p):finishvY);
Depth2=yy(startvY)-yy(centervY(2));


%New coordinates (sets the beggin points on the orgin (0,0))

Xhalf1newX=Xhalf1X-Xhalf1X(length(Xhalf1X));
Yhalf1newX=Yhalf1X-Yhalf1X(length(Yhalf1X));
Xhalf2newX=Xhalf2X-Xhalf2X(1);
Yhalf2newX=Yhalf2X-Yhalf2X(1);

Xhalf1newY=Xhalf1Y-Xhalf1Y(length(Xhalf1Y));
Yhalf1newY=Yhalf1Y-Yhalf1Y(length(Yhalf1Y));
Xhalf2newY=Xhalf2Y-Xhalf2Y(1);
Yhalf2newY=Yhalf2Y-Yhalf2Y(1);

% plots new truncated crucible on origin
```

```
figure(2)
subplot(2,2,1)
hold on
plot(Xhalf1newX,Yhalf1newX,'r')
plot(Xhalf2newX,Yhalf2newX,'r')
line([Xhalf1newX(length(Xhalf1newX)),Xhalf1newX(length(Xhalf1newX))],[Y
half1newX(1),Yhalf1newX(length(Yhalf1newX))])
title('X data plot with centroid line')
hold off

subplot(2,2,3)
hold on
plot(Yhalf1newX,Xhalf1newX,'r')
plot(Yhalf2newX,Xhalf2newX,'b')
axis([-10, Yhalf1newX(1), Xhalf1newX(1),
Xhalf2newX(length(Xhalf2newX))])
title('X data flipped axis for disk method')
xlabel('depth (micron)')
ylabel('x-axis (micron)')
hold off

subplot(2,2,2)
hold on
plot(Xhalf1newY,Yhalf1newY,'r')
plot(Xhalf2newY,Yhalf2newY,'r')
line([Xhalf1newY(length(Xhalf1newY)),Xhalf1newY(length(Xhalf1newY))],[Y
half1newY(1),Yhalf1newY(length(Yhalf1newY))])
title('Y data plot with centroid line')
hold off

subplot(2,2,4)
hold on
plot(Yhalf1newY,Xhalf1newY,'r')
plot(Yhalf2newY,Xhalf2newY,'b')
axis([-10, Yhalf1newY(1), Xhalf1newY(1),
Xhalf2newY(length(Xhalf2newY))])
title('Y data flipped axis for disk method')
xlabel('depth (micron)')
ylabel('x-axis (micron)')
hold off

%% start of volume calculation

if mod(length(Xhalf1newX),2)==1
    Xhalf1newX=Xhalf1newX(1:length(Xhalf1newX)-1);
end
if mod(length(Xhalf2newX),2)==1
    Xhalf2newX=Xhalf2newX(1:length(Xhalf2newX)-1);
end

if  flag==1

A1X=abs(Xhalf1newX); %
B1X=abs(A1X/rat);
end
```

```
if flag==2

B1X=abs(Xhalf1newX);
A1X=abs(B1X*rat);
end

%% Start of X 1 loop
for i=2:length(Xhalf1newX)-1


if mod(i,2)==0
sim1X(i)=2*A1X(i)*B1X(i);
end
if mod(i,2)==1
sim1X(i)=4*A1X(i)*B1X(i);
end
end

sim1X(1)=A1X(1)*B1X(1);
sim1X(length(Xhalf1newX))=A1X(length(Xhalf1newX))*B1X((length(Xhalf1new
X)));

deltax1X=(Xhalf1newX(3)-Xhalf1newX(1))/2;

if  flag==1

A2X=abs(Xhalf2newX);
B2X=abs(A2X/rat);
end
if flag==2

B2X=abs(Xhalf2newX);
A2X=abs(B2X*rat);
end
%% Start of the X 2 loop
for i=2:length(Xhalf2newX)-1

if mod(i,2)==0
sim2X(i)=2*A2X(i)*B2X(i);
end
if mod(i,2)==1
sim2X(i)=4*A2X(i)*B2X(i);
end
end

sim2X(1)=A2X(1)*B2X(1);
sim2X(length(Xhalf2newX))=A2X(length(Xhalf2newX))*B2X(length(Xhalf2newX
));
deltax2X=(Xhalf2newX(3)-Xhalf2newX(1))/2;

if mod(length(Xhalf1newY),2)==1
    Xhalf1newY=Xhalf1newY(1:length(Xhalf1newY)-1);
end
if mod(length(Xhalf2newY),2)==1
```

```
    Xhalf2newY=Xhalf2newY(1:length(Xhalf2newY)-1);
end

if  flag==1

B1Y=abs(Xhalf1newY);
A1Y=abs(rat*B1Y);
end
if flag==2

A1Y=abs(Xhalf1newY);
B1Y=abs(A1Y/rat);
end

%% Start of Y 1 loop
for i=2:length(Xhalf1newY)-1


if mod(i,2)==0
sim1Y(i)=2*A1Y(i)*B1Y(i);
end
if mod(i,2)==1
sim1Y(i)=4*A1Y(i)*B1Y(i);
end
end

sim1Y(1)=A1Y(1)*B1Y(1);
sim1Y(length(Xhalf1newY))=A1Y(length(Xhalf1newY))*B1Y((length(Xhalf1new
Y)));
deltax1Y=(Xhalf1newY(3)-Xhalf1newY(1))/2;

if  flag==1
%     A2Y=abs(sqrt(Xhalf2newY.^2/(1-f^2)));;
%     B2Y=abs(Xhalf2newY);
B2Y=abs(Xhalf2newY);
A2Y=abs(rat*B2Y);
end
if flag==2
%     B2Y=abs(((Xhalf2newY.^2*(1-f^2))).^1/2);
%     A2Y=abs(Xhalf2newY);
A2Y=abs(Xhalf2newY);
B2Y=abs(A2Y/rat);
end
%% Start of Y 2 Loop
for i=2:length(Xhalf2newY)-1

if mod(i,2)==0
sim2Y(i)=2*A2Y(i)*B2Y(i);
end
if mod(i,2)==1
sim2Y(i)=4*A2Y(i)*B2Y(i);
end
end
```

```
sim2Y(1)=A2Y(1)*B2Y(1);
sim2Y(length(Xhalf2newY))=A2Y(length(Xhalf2newY))*B2Y(length(Xhalf2newY
));
deltax2Y=(Xhalf2newY(3)-Xhalf2newY(1))/2;



V1=sum(sim1X)*(deltax1X/3)*pi; % for X
V2=sum(sim2X)*(deltax2X/3)*pi;

V3=sum(sim1Y)*(deltax1Y/3)*pi; % for Y
V4=sum(sim2Y)*(deltax2Y/3)*pi;


 if p==1
   newstat1=[V1; V2; V3; V4]
   Mean1=mean(newstat1);
       Std1=std(newstat1);
       Unc1=(Std1*3.182)/2;
 end
 if p==2
   newstat2=[V1; V2; V3; V4]
   Mean2=mean(newstat2);
       Std2=std(newstat2);
       Unc2=(Std2*3.182)/2;
 end
end
       D1=rad1*2 ;
       D2=rad2*2 ;
       AR1=D1/Depth1;
       AR2=D2/Depth2;
       IsoAR1=(D1-MaskD)/Depth1;
       IsoAR2=(D2-MaskD)/Depth2;
       MD=mean([D1,D2]);
       RadEtch=(MD-MaskD)/2;

  Stat1=[Mean1;Std1;Unc1;f];
  Stat2=[Mean2;Std2;Unc2;f];
  Geom=[D1;D2;Depth1;Depth2;AR1;AR2;IsoAR1;IsoAR2];

Geomstat=[mean([D1,D2]);mean([Depth1,Depth2]);mean([AR1,AR2]);mean([Iso
AR1,IsoAR2]);RadEtch];
  f
newfolder=[basefolder1 filesep 'volume stats'];

xlswrite(newfolder,newstat1,'A2:A5');
xlswrite(newfolder,newstat2,'B2:B5');
xlswrite(newfolder,Geom,'C2:C9');
xlswrite(newfolder,Geomstat,'D2:D6');
xlswrite(newfolder,Stat1,'D8:D11');
xlswrite(newfolder,Stat2,'D13:D16');
```

Chemical List

Chemical Name	Company Purchased
NR21-20000P Negative Thick Resist	Futurrex
RR41 Resist Remover	Futurrex
RD6 Resist Developer	Futurrex
PCB Etchant Solution	Radioshack
Dimethly Sulfoxide (CPA)	Fisher Scientific
Phosphate Buffered Saline (CPA)	Fisher Scientific
Ethylene Glycol (CPA)	Fisher Scientific
MXB929 Nickel Stripper	Caswell Inc
Sparex No.2 Pickling compound	Grobet USA
Sulfuric Acid 99%	University Chemical Store
Cupric Sulfate	University Chemical Store
Methylene Chloride	University Chemical Store
Acetone	University Chemical Store